STATISTICAL MECHANICS OF JAMMED MATTER

by

Ping Wang

A dissertation submitted to the Graduate Faculty in Physics in partial fulfillment of the requirements for the degree of Doctor of Philosophy, The City University of New York

2009

This manuscript has been read and accepted for the
Graduate Faculty in Physics in satisfaction of the
dissertation requirement for the degree of Doctor of Philosophy.

Prof. Hernan Makse

Date — Chair of Examining Committee

Prof. Steven Greenbaum

Date — Executive Officer

Prof. Hernan Makse, Physics Department, CCNY

Prof. Timothy H. Boyer, Physics Department, CCNY

Prof. Sergey Buldyrev, Physics Department, Yeshiva University

Prof. Sergey Vitkalov, Physics Department, CCNY

Prof. Charles Maldarelli, Chemical Engineering Department, CCNY

Supervisory Committee

THE CITY UNIVERSITY OF NEW YORK

Abstract

STATISTICAL MECHANICS OF JAMMED MATTER

by

Ping Wang

Adviser: Professor Hernán A. Makse

In a thermal system, the Brownian motion of the constituent particles implies that the system dynamically explores the available energy landscape, such that the notion of a statistical ensemble applies. For densely packed systems of interest in this study, in which enduring contacts between particles are important, the potential energy barrier prohibits an equivalent random motion. At first sight it seems that the thermal statistical mechanics do not apply to these systems as there is no mechanism for averaging over the configurational states. Hence, these systems are inherently out of equilibrium. On the other hand, if the granular material is gently tapped such that the grains can slowly explore the available configurations, the situation becomes analogous to the equilibrium case scenario. It has been shown that the volume of the system is dependent on the applied tapping regime, and that this dependence is reversible, implying ergodicity [1]. This result gives support to the proposed statistical ensemble valid for dense, static and slowly moving granular materials which was first introduced by Edwards and Oakeshott in 1989 [2, 3]. Through this approach, notions of macroscopic quantities such as entropy and compactivity were also introduced to granular matter.

Acknowledgements

I am deeply grateful to my supervisor, Professor Hernán A. Makse, Physics Department and Levich Institute, City College of New York, for his important support and constructive comments throughout this work.

I am grateful to my close friend and colleague Dr. Chaoming Song, Physics Department, Physics Department and Levich Institute, City College of New York, who contributed to most parts of this work.

I wish to express my thanks to our group members Chris Briscoe, Kun Wang and Yuliang Jin, for useful discussions.

Contents

List of Figures

Chapter 1

Introduction to the Concept of Jamming

The act of jamming or the condition of being jammed stems from the following layman meaning:

'a crowd or congestion of people or things in a limited space, e.g. a traffic jam'.

The scientific translation defines "jamming" as a state which emerges when a many-body system is blocked in a configuration far from equilibrium, from which it takes too long a time to relax for the time scale to be a measurable quantity. Jamming is emerging as a fundamental feature of many diverse systems [4], such as

- Granular materials: sand, sugar, marbles, dry powders
- Emulsions: mayonnaise, custard, milk

- Colloidal suspensions: paints, muds
- Structural glasses: polymer melts, silica glass
- Spin glasses.

These distinct disordered systems are but a few examples of out of equilibrium systems, which are united by their behaviour at the point of structural arrest. Whereas one can think of liquids or suspensions as consisting of particles which move very slowly compared to gases, a state may occur where all particles are in close contact with one another and therefore experience jamming. The process of jamming is specific to the system in question due to their different microscopic properties. The following examples illustrate this. While it suffices to pour a granular material into a closed container and shake it to jam up the particles, the emulsion droplets require a large 'squeezing' force usually implemented by centrifugation. On the other hand, the interaction between colloidal particles can be tuned such that the interparticle attraction induces a jammed configuration even at low densities of the material. Furthermore, glassy materials can be cooled down to very low temperatures at which the molecules can no longer diffuse, thus trapping the system into jammed configurations. Hence, through very different jamming mechanisms, we arrive at the jammed state for a variety of systems.

All these systems belong to a class of materials known as 'soft' matter, referring to their complex mechanical properties which are neither fluid nor solid-like. This behaviour is directly linked to the material's capability to support a mechanical disturbance once it has reached a jammed state. While the concepts of crowding and the subsequent mechanical response unite these materials, the details of their

constitutive particles introduce important differences. For instance, in a polymer melt, it is the physical chemistry of the individual strands which will govern the ensemble, whereas it is the interactions between the colloidal particles, rather than their constituent molecules, which will determine the system behaviour in suspensions. Moreover, particles of sizes up to 1μm are governed by the laws of statistical mechanics since their dynamics is due to thermal (Brownian) motion. Above that threshold size (e.g. grains), the gravitational energy exceeds k_BT, where T is the room temperature and k_B the Boltzmann constant, thus prohibiting motion. The colloidal regime is therefore defined for sizes between 1nm and 1μm, such that thermal averaging is present. It applies to glasses, colloids, surfactants and microemulsions, or in other words, to 'complex fluids'. Most of the fundamental physics research has been performed on thermal systems until present, and many of the unifying concepts have arisen through the comparison of systems within this category.

In the next three chapters we first describe the structural arrest in thermal systems, where the classical statistical mechanics tools are applicable, and then proceed to athermal systems, such as sheared granular materials, in which new situations suitable for a statistical analysis are introduced.

1.1 Jamming in Glassy Systems

In a fluid at thermal equilibrium the particle dynamics is too fast to capture the detail of the underlying potential energy landscape, thus it appears flat. Decreasing the temperature slows down the Brownian dynamics, implying a limiting temper-

ature below which the system can no longer be equilibrated in this way. Hence, the thermal system falls out of equilibrium on the time scale of the experiment and thus undergoes a *glass transition* [5]. The motion of each particle is no longer thermally activated and only the vibration inside the cage formed by its surrounding neighbours persists. However, even below the glass transition temperature the particles continue to relax, but the nature of the relaxation is very different to that in equilibrium. This phenomenon of a structural evolution beyond the glassy state is known as "aging". The dynamics becomes dominated by the multidimensional potential energy surface which the system can explore as a function of the degrees of freedom of the particles. In order to describe this landscape Stillinger and coworkers [6], based on ideas introduced by Goldstein [7], developed the concept of inherent structures which are defined as the potential energy minima. The trajectory of a system aging at temperature T can be mapped onto the successive potential basins that the system explores. Computational methods are the only available technique for investigating this behaviour, in which the inherent structures are found via steepest-descent quenching of the system configurations to the basins of the wells. The entropy of the system can be shown to be separable into contributions from the available configurations and the vibrational modes around each minimum. There have been many studies which have embarked on an investigation of aging through the exploration of the configurational space [8, 9, 10].

The importance of the inherent structure formalism is in enabling the comparison of jamming in particulate systems with glasses [11]. The entropy arising from the inherent configurations of the glass at very low temperatures and the exploration of these configurations due to the vibrational modes of the particles

could be viewed as analogous to the configurational changes in particulate packings under slow tapping or shear. However, in granular materials there is an added effect of friction, which dissipates the analogous vibrations at once. Unlike granular materials, a thermal system is never permanently trapped in the bottom of a valley, but escapes in other accessible unstable directions through intrinsic thermal vibrations. At any finite temperature the system will not resemble the granular system in that it continuously evolves toward a maximum density state. Thus, the only true analogous situation between glasses and granular materials is valid at zero temperature. However, there are characteristic features of the glassy relaxation at a finite T which act as useful tools for the description of granular systems by exploiting the analogy between the relaxation of powders and aging in glassy systems [12].

For instance, theories developed during the late eighties and nineties in the field of spin glasses [13, 14] have led to a better understanding of glassy systems through the generalisation of usual equilibrium relations, such as the fluctuation-dissipation relation, to situations far from equilibrium [15]. This approach developed by Cugliandolo, Kurchan and collaborators yielded macroscopic observable properties, such as an "effective temperature" for the slow modes of relaxation, which could then be compared between various glassy systems. Furthermore, the existence of an effective temperature with a thermodynamic meaning in glasses at very low temperature suggests an 'ergodicity' for the long-time behaviour of the system [16]. This ergodicity is closely related to the statistical ideas for granular systems [17, 18, 19] which we will introduce in the following sections. In support of this argument, the effective temperature in glasses is found to be an adequate

concept for describing granular matter [20], as it will be shown in Chapter 4.

From a theoretical point of view, these systems are still only understood in terms of predictions of a general nature and many open questions remain. There is still much debate on issues such as the precise mechanisms of surfing the energy landscape, the effects of memory in the system, the slowing down of the system with time, and the discrepancies between the behaviour of different glassy systems, but they are beyond the scope of this work.

1.2 Jamming in Particulate Systems

In a sense one would imagine there is no simpler physical system than a granular assembly. After all it is just a set of packed rigid objects with no interaction energy. It is the inability to describe the system on the continuum level in any other way except according to its geometry which has led to a lack of a well established granular theory until present. Mostly due to their industrial importance, there has been a vast literature describing phenomenological observations without an encompassing theory. In the words of de Gennes, the state of granular matter can be compared to solid state physics in the 30's or critical phenomena in phase transitions before the renormalization group. In other words, there is a need for describing the universal features of the observed behaviour within a theoretical framework devised for these and other jammed systems.

In parallel with the extensive research on glasses, described earlier, a decade ago Edwards and collaborators postulated the existence of a statistical ensemble for granular matter, despite the lack of thermal motion and the absence of an

equilibrium state [21, 2, 3, 22, 23]. The main postulate was based on jamming the granular particles at a fixed total volume such that all microscopic jammed states are equally probable and become accessible to one another (ergodic hypothesis) by the application of a type of external perturbation such as tapping or shear, just as thermal systems explore their energy landscape through Brownian motion. Hence, let us consider granular jamming in more detail.

Pouring sugar into a cup is the simplest example of a fluid to solid transition which takes place solely because of a density increase. In terms of physics, in particulate materials such as emulsions and granular media, a jammed system results if particles are packed together so that all particles are touching their neighbours, which obviously requires a sufficiently high density. In these athermal systems there is no kinetic energy of consequence; the typical energy required to change the positions of the jammed particles is very large compared to the thermal energy at room temperature ($\sim 10^{14}$ times, see Chapter 4). As a result, the material remains arrested in a static state and is able to withstand a sufficiently small applied stress.

There is a subtle, but crucial difference, between a configuration in mechanical equilibrium and a jammed configuration, particularly in the context of this research. The mechanism of arriving at a *static configuration* by an increase in density, which is an intuitively obvious process, is not always sufficient to satisfy the *jamming* condition in our definition. This applies especially to systems which bear knowledge of the process of their creation. For instance, pouring grains into a container results in a pile at a given angle of repose. This equilibrium configuration is not jammed because in response to an external perturbation, the constituent par-

ticles will irreversibly rearrange, approaching a truly jammed configuration. The statistical mechanics which we are aiming to test implies an ergodic hypothesis, which is not valid in such history-dependent samples [1].

It turns out that by allowing the system to explore its available configurational space through external mechanical perturbations, the system will rearrange such that all possible configurations (w.r.t. the perturbation) become accessible to one another. Continuing with the analogy in the real world, the gentle tapping on a table of the cup filled with sugar will initially change the unstable angle of repose of the sugar pile and flatten its top surface, and therefore its density, until it settles into a desired configuration which depends on the strength of the tap. We can only perform a statistical analysis on the resulting configurations which have no memory of their creation, i.e. the true jammed configurations. Thus we arrive at a jammed ensemble, suitable for the application of statistical mechanics, described in Chapter 2. Since the particles can jump across the energy landscape during the tap, but then stop at once due to frictional dissipation, there is an analogy to the inherent structure formalism in glassy systems [11]. This new statistical mechanics is able to provide unifying concepts between previously unrelated media.

1.2.1 Applications of the jamming condition

The statistical mechanics which we are aiming to develop implies an ergodic hypothesis, which is not valid in history-dependent samples. In fact, there are many experimental situations in which the statistical mechanics cannot be applied due

[1] Theories attempting to describe such systems have been developed by Bouchaud et al, proposing a model for the 'fragile' systems, i.e. systems which rearrange under infinitesimal stresses [24]. However, this situation will not be considered here.

to the lack of ergodicity. For instance convection cycles have been observed in granular systems under vigorous tapping [25]- an effect which is closely associated with the segregation process of different granular species. These types of closed loops in phase space cannot be described within the thermodynamic framework. Rapid granular flows observed in pouring sand in a pile, or vigorously shaken granular systems at low density are out of the scope of the present approach since the systems are exploring configurations far from the jammed states [26]. Kinetic theories of inelastic gases are more appropriate to treat these situations [27]. The physics of the angle of repose [28] may not be understood under the thermodynamic framework due to the absence of the jamming condition of the pile, despite the fact that it is static. In many practical situations, heterogeneities appear which also preclude the application of a thermodynamic approach. For instance, when granular materials are sheared in a sufficiently large shear stage, shear bands appear where the strain is discontinuous [29]. Such local effects cannot be captured by the present thermodynamic approach.

On the other hand, if the application of statistical physics to jammed phenomena were to prove productive, then one could anticipate a more profound insight into the characterisation and understanding of the system as a whole. For instance, the thermodynamic hypothesis would lead to the prediction of macroscopic quantities such as viscosity and complex shear moduli, which would in turn provide a complete rheological caracterisation of the system. As a matter of theoretical interest, a statistical ensemble for jammed matter could be one of the very few generalisations of the statistical mechanics of Gibbs and Boltzmann to systems out of equilibrium.

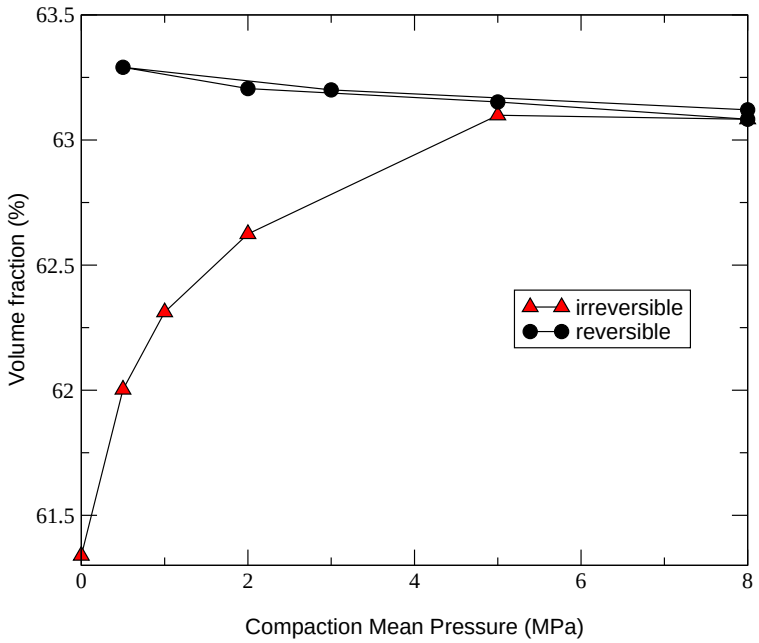

Figure 1.1: Compaction curve for a packing of glass beads under an oscillating pressure. Increasing the amplitude of oscillation initially increases the density by filling the loose voids, after which a reversible regime is achieved (from [30]).

1.2.2 Achieving the jammed state

Experimentally, the conditions for a statistical ensemble of jammed states can be achieved by pre-treating the granular assembly by tapping or via slow shear-driving. Experiments at the University of Chicago involving the tapping of granular columns were the first to show the existence of a reversible regime in which the system configurations are independently sampled [1]. Starting with a loose packing of the grains, the tapping routine initially removes the unstable loose voids and thus eliminates the irreversible grain motion. Once all the grains are touching their neighbours, the density of the resulting configuration becomes dependent on the tapping amplitude and the number of taps; the larger the amplitude, the lower the density. The mechanism of the *compaction* process leading to a steady-state

density is extremely slow, in fact, it is logarithmic in the number of taps. This dependence of the density of grains on the external perturbation of the system once the memory effects of the pile construction details have been removed, is known as the reversible branch of the 'compaction curve', see Fig. 1.1. Despite the presence of friction between grains (implying memory effects) this curve is reversible, establishing a new type of equilibrium states. It is along this curve that the thermodynamics for granular matter can be applied.

There have been several further experiments confirming these results for different system geometries, particle elasticities and compaction techniques. For example, the system can be mechanically tapped or oscillated, vibrated using a loudspeaker, slowly sheared in a couette geometry, or even allowed to relax under large pressures over long periods of time, all to the same effect [31, 32, 30, 33]. Here we show a new compaction regime under an oscillating pressure where the same density dependence of a packing of glass and acrylic beads is noted for varying amplitudes of the pressure oscillation. These experiments have been performed at Schlumberger-Doll Research [30]. The resulting curve of the achieved volume fraction as a function of the amplitude of the pressure oscillation is shown in the inset of Fig. 1.1.

Moreover, experiments in the Cavendish laboratory [33] have shown how the conductivity of powdered graphite can also be a measure of the particle density as it is being vibrated, in which the direct link to the volume function is less obvious, but the qualitative results indicate the same trends. The methodology for achieving jammed configurations has also been established experimentally for the purpose of rheological and thermodynamical studies and it will be described

in Chapter 4.

At this point, it is important to note that we have only considered infinitely rigid, rough grains in which an increase in the pressure of the system, for instance by placing a piston on top of the grains, causes no change in the shape of the grains and therefore no change in the packing density. On the other hand, real grains have a finite elastic modulus, thus the application of a sufficiently large external pressure will always result in grain deformation and therefore a density increase unrelated to the tapping. In soft particles, such as emulsions, the effect of pressure is more significant. The tapping experiment described above measured the resulting densities at atmospheric pressure, which is considered to be the zero reference pressure. The same experiment can be repeated at finite pressures giving rise to equivalent compaction curves, depicted in Fig. 1.2. Whereas hard grains, such as glass beads, require extremely large pressures ($\sim$ 1MPa) to deform and the amount of deformation is limited by their yield stress, softer particles, such as rubber, are able to reach higher densities with relative ease. Droplets and bubbles, being the softest particles one can have, are capable of reaching the density of 1, corresponding to a biliquid foam and a foam, respectively, by an application of much smaller pressures ($\sim$ 1kPa). They have the advantage of the whole pressure range being accessible to them. Another distinction between granular materials and emulsions is the presence of friction in the former and the smoothness of the latter. Since friction plays an important role in inducing memory into the system, its absence leads to a much easier achievement of the jammed state, described above. For instance, in the case of emulsions, allowing the particles to cream under gravity will suffice to arrive at the reversible part of the compaction curve,

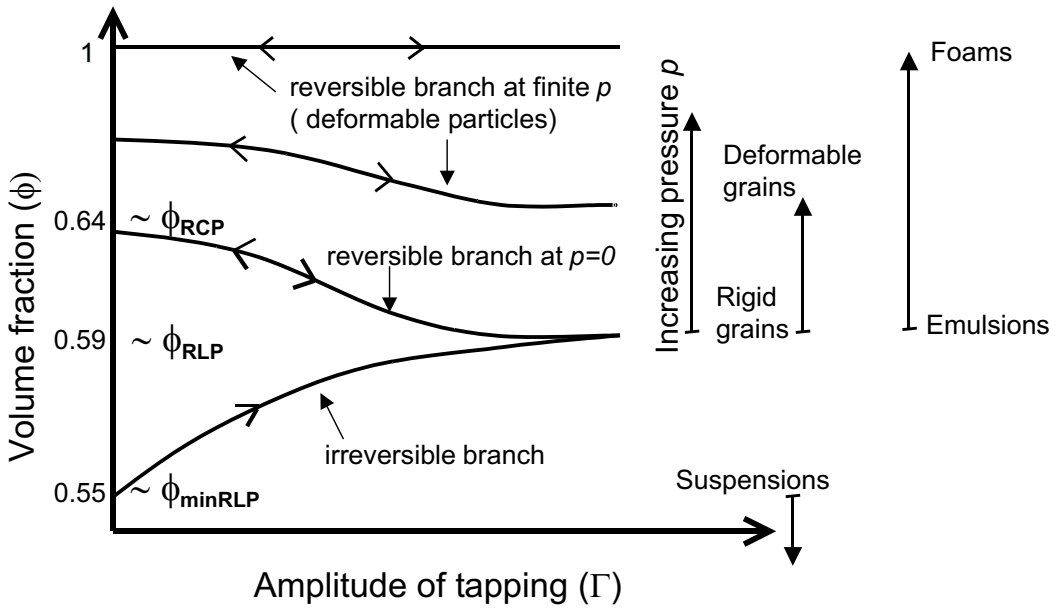

Figure 1.2: Compaction curves of volume fraction ϕ versus amplitude of oscillation A for different external confining pressures, p. Increasing the amplitude of oscillation initially increases the volume fraction by filling the loose voids (irreversible branch), after which a reversible regime is achieved. For infinitely rigid grains (the "zero pressure" curve) the minimum volume fraction along the irrevesible branch is the random loose packing. The reversible branch goes from the maximum random loose packing fraction to the random close packing fraction. Below the minimum RLP only suspensions can exist. See Section 2.2.2 for details.

bypassing the irreversible branch.

1.3 Unifying Concepts in Granular Matter and Glasses

In the preceding paragraphs, it has been shown under which conditions both thermal and athermal systems explore the configurational energy landscape, which possibly results in commonalities in their behaviour. At present, new unifying

theoretical descriptions for jammed matter are being sought, as well as new experimental evidence to unify the predicted state for *all* varieties of jammed systems.

The prediction of how different systems jam with respect to the applied stress, density and temperature has led to a speculative diagram proposed by Liu and Nagel in their article "Jamming is not just cool anymore" in Nature [34, 35, 36]. It links the behaviour of glasses (thermal systems) and bubbles, grains, droplets (athermal systems) by the dynamics of their approach to jamming.

Since the observable properties such as applied strain, temperature and density can be obtained by consideration of only the jammed configurations in a given system, the thermodynamics of jamming, discussed in the next Chapter, is intimately related to the ideas put forward in the jamming phase diagram.

Chapter 2

New Statistical Mechanics for Granular Matter

This Chapter aims to justify the use of statistical mechanics tools in situations where the system is far from thermal equilibrium, but jammed. In what follows, we present the classical statistical mechanics theorems to an extent which facilitates an understanding of the important concepts for the development of an analogous granular theory, as well as the assumptions necessary for the belief in such a parallel approach. Thereafter, we present a theoretical framework to fully describe the exact specificities of the granular packing, and the shaking scenario which leads to the derivation of the Boltzmann equation for a jammed granular system.

This kind of an analysis paves the path to macroscopic quantities, such as the compactivity, characterising each static configuration from the microstructural information of the packing. It is according to this theory that the jammed configurations obtained from experiments and simulations are later characterised.

2.1 Classical Statistical Mechanics

In the conventional statistical mechanics of thermal systems, the different possible configurations, or microstates, of the system are given by points in the phase space of all positions and momenta $\{p, q\}$ of the constituent particles. The equilibrium probability density ρ_{eqm} must be a stationary state of Liouville's equation which implies that ρ_{eqm} must be expressed only in terms of the total energy of the system, E [37]. The simplest form for a system with Hamiltonian $\mathcal{H}(p, q)$ is the microcanonical distribution:

$$\rho_{\text{eqm}}(E) = \frac{1}{\Sigma_{\text{eqm}}(E)}, \tag{2.1}$$

for the microstates within the ensemble, $\mathcal{H}(p, q) = E$, and zero otherwise. Here,

$$\Sigma_{\text{eqm}}(E) = \int \delta(E - \mathcal{H}(p, q)) \;\; dp \; dq, \tag{2.2}$$

is the area of energy surface $\mathcal{H}(p, q) = E$.

Equation (2.1) states that all microstates are equally probable. Assuming that this is the true distribution of the system implies accepting the ergodic hypothesis, i.e. the trajectory of the closed system will pass arbitrarily close to any point in phase space.

It was the remarkable step of Boltzmann to associate this statistical concept of the number of microstates with the thermodynamic notion of entropy through his famous formula

$$S_{\text{eqm}}(E) = k_B \log \Omega_{\text{eqm}}(E). \tag{2.3}$$

Thus, in classical statistical mechanics, the total energy of the system is sufficient to describe the probability density of states. Whereas the study of thermal systems has had the advantage of available statistical mechanics tools for the exploration of the phase space, an entirely new statistical method, unrelated to the temperature, had to be constructed for grains.

2.2 Statistical Mechanics for Jammed Matter

We now consider a jammed granular system composed of *rigid* grains Such a system is analogously described by a network of contacts between the constituent particles in a fixed volume, V, since there is no relevant energy E in the system. In the case of granular materials, the analogue of phase space, the space of microstates of the system, is the space of possible jammed configurations as a function of the degrees of freedom of the system $\{\zeta\}$.

It is argued that it is the volume of this system, rather than the energy, which is the key macroscopic quantity governing the behaviour of granular matter [21, 2, 3]. If we have N grains of specified shape which are assumed to be infinitely rigid, the system's statistics would be defined by a function $\mathcal{W}(\zeta)$, a function which gives the volume of the system in terms of the specification of the grains.

In this analogy one replaces the Hamiltonian $\mathcal{H}(p, q)$ of the system by the volume function, $\mathcal{W}(\zeta)$. The average of $\mathcal{W}(\zeta)$ over all the jammed configurations determines the volume V of the system in the same way as the average of the Hamiltonian determines the average energy E of the system.

2.2.1 Definition of the volume function, $\mathcal{W}$

One of the key questions in this analogy is to establish the 'correct' $\mathcal{W}$ function, the statistics of which is capable of fully describing the system as a whole. The idea is to partition the volume of the system into different subsystems α with volume $\mathcal{W}^\alpha$, such that the total volume of a particular configuration is

$$\mathcal{W}(\zeta) = \sum_\alpha \mathcal{W}^\alpha \tag{2.4}$$

It could be that considering the volume of the first coordination shell of particles around each grain is sufficient; thus, we may identify the partition α with each grain. However, particles further away may also play a role in the collective system response due to enduring contacts, in which case $\mathcal{W}$ should encompass further coordination shells. In reality, of course, the collective nature of the system induces contributions from grains which are indeed further away from the grain in question, but the consideration of only its nearest neighbours is a good starting point for solving the system, and is the way in which we proceed to describe the $\mathcal{W}$ function. The significance of the appropriate definition of $\mathcal{W}$ is best understood by the consideration of a response to an external perturbation to the system in terms of analogies with the Boltzmann equation which we will describe in Section 2.4.

Perhaps the most straightforward definition of the function $\mathcal{W}^\alpha$ is given in terms of the Voronoi diagram which partitions the space into a set of regions, associating all grain centroids in each region to the closest grain centroid, depicted by line OP in the diagram in Fig. 2.1a. The loop formed by the perpendicular bisectors (ab) of each of the lines joining the central grain to its neighbours is the Voronoi cell,

depicted in red. Even though this construction successfully tiles the system, its drawback is that there is no analytical formula for the enclosed volume of each cell. Recently Ball and Blumenfeld [38, 39] have shown by an exact triangulation method that the volume defining each grain can be given in terms of the contact points C using vectors constructed from them (see Fig. 2.1b). The method consists in defining shortest loops of grains in contact with one another (p,q loops), thus defining the void space around the central grain. The difficulty arises in three dimensions since this construction requires the identification of void centres, v. This is not an obvious task, but is currently under consideration. The resulting volume (red) is the antisymmetric part of the fabric tensor, the significance of which is its appearance in the calculation of stress transmission through granular packings [38].

A cruder version for the volume per grain, yet with a strong physical meaning, has been given by Edwards. For a pair of grains in contact (assumed to be point contacts for rough, rigid grains) the grains are labelled α, β, and the vector from the centre of α to that of β is denoted as $\vec{R}^{\alpha\beta}$ and specifies the complete geometrical information of the packing. The first step is to construct a configurational tensor $\vec{\mathcal{C}}^{\alpha}$ associated with each grain α based on the structural information,

$$\mathcal{C}_{ij}^{\alpha} = \sum_{\beta} R_i^{\alpha\beta} R_j^{\alpha\beta}. \tag{2.5}$$

Then an approximation for the area in 2D or volume in 3D encompassing the first coordination shell of the grain in question is given as

$$\mathcal{W}^{\alpha} = 2\sqrt{\mathrm{Det}\mathcal{C}_{ij}^{\alpha}}. \tag{2.6}$$

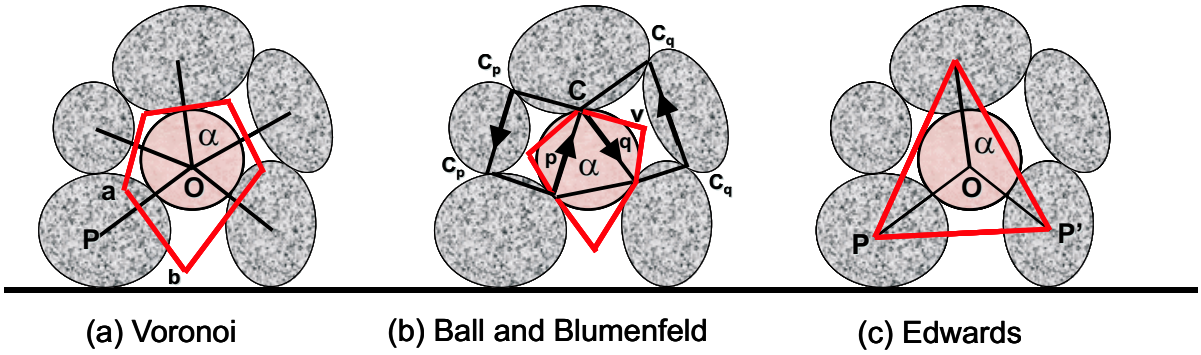

Figure 2.1: Different volume functions as discussed in the text: (a) Voronoi, (b) Ball and Blumenfeld and (c) Edwards construction.

This volume function is depicted in the Fig. 2.1c, with grain coordination number 3 in two dimensions, where Eq. (2.6) should give the area of the triangle (red) constructed by the centres of grains P which are in contact with the grain α. The above equation is exact if the area is considered as the determinant of the vector cross product matrix of the two sides of the triangle. Surprisingly, this approximation works well for other coordination numbers and even in 3D, due to the partitioning of the obtained volumetric objects into triangles/pyramids, intrinsic to the method, and subsequently summing over them to obtain the resulting volume. However, this definition is clearly only an approximation of the space available to each grain since there is an overlap of $\mathcal{W}^\alpha$ for grains belonging to the same coordination shell. Thus, it overestimates the total volume of the system: $\sum \mathcal{W}^\alpha > V$. However, it is the simplest approximation for the system based on a single coordination shell of a grain.

2.2.2 Entropy and compactivity

Now that we have explicitly defined $\mathcal{W}$ it is possible to define the entropy of the granular packing. The number of microstates for a given volume V is measured by the area of the surface $\mathcal{W}(\zeta) = V$ in the phase space of jammed configurations and it is given by:

$$\Sigma_{\text{jammed}}(V) = \int \delta\Big(V - \mathcal{W}(\zeta)\Big) \;\; \Theta(\zeta) \;\; d\zeta, \tag{2.7}$$

where now $d\zeta$ refers to an integral over all possible jammed configurations and $\delta(V - \mathcal{W}(\zeta))$ formally imposes the constraint to the states in the sub-space $\mathcal{W}(\zeta) = V$. $\Theta(\zeta)$ is a constraint that restricts the summation to only reversible jammed configurations as opposed to the merely static equilibrium configurations as previously discussed. The radical step is the assumption of equally probable microstates which leads to an analogous thermodynamic entropy associated with this statistical quantity:

$$S(V) = \lambda \log \Sigma_{\text{jammed}}(V) = \lambda \log \int \delta(V - \mathcal{W}(\zeta)) \;\; \Theta(\zeta) \;\; d\zeta, \tag{2.8}$$

which governs the macroscopic behaviour of the system [3, 2]. Here λ plays the role of the Boltzmann constant. The corresponding analogue of temperature, named the "compactivity", is defined as

$$X_V^{-1} = \frac{\partial S}{\partial V}. \tag{2.9}$$

where the subscript V refers to the fact that it is the derivative of the entropy with respect to the volume.

This is a bold statement, which perhaps requires further explanation in terms of the actual role of compactivity in describing granular systems. We can think of the compactivity as a measure of how much more compact the system could be, i.e. a large compactivity implies a loose configuration (e.g. random loose packing, RLP) while a reduced compactivity implies a more compact structure (e.g. random close packing, RCP, the densest possible random packing of monodisperse hard spheres). In terms of the reversible branch of the compaction curve, large amplitudes generate packings of high compactivities, while in the limit of the amplitude going to zero a low compactivity is achieved. In terms of the entropy, many more configurations are available at high compactivity, thus the dependence of the entropy on the volume fraction can be qualitatively described as in Fig. 2.2. In the figure, for monodisperse packings the RCP is identified at $\phi \approx 0.64$ [40], the maximum RLP fraction is identified at $\phi \approx 0.59$ [41], while the crystalline packing, FCC, is at $\phi = 0.74$ but cannot be reached by tapping.

At any given tapping amplitude, there exists an equilibrium volume fraction toward which the system slowly evolves. For instance, a system may find itself at a lower entropy than the equilibrium curve by the application of an internal constraint at a given volume fraction. This situation can be achieved by creating small crystalline regions within a packing configuration of a lower density, and looser regions compensating for the volume reduction such that the total volume of the system remains constant. This configuration, given that it is not jammed, will tend toward the equilibrium packing via the application of a small perturbation

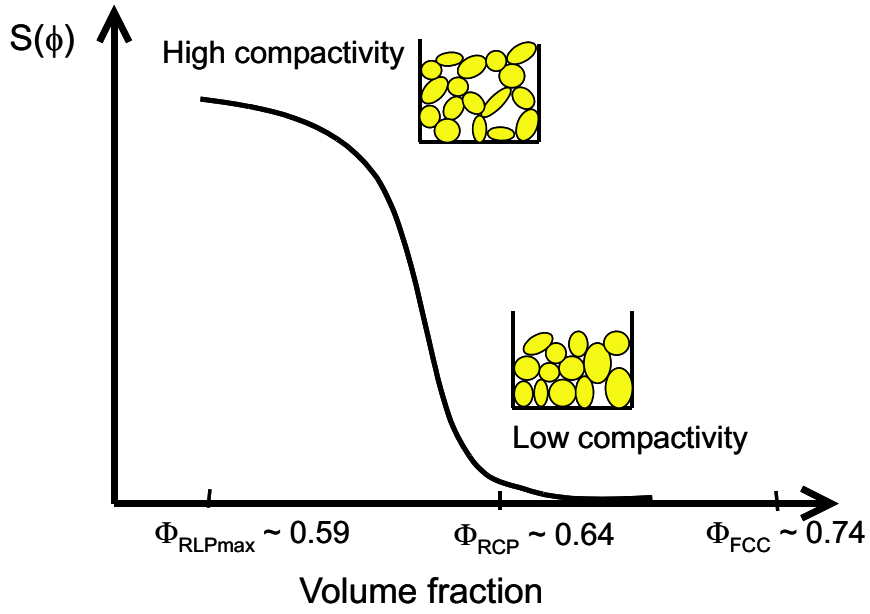

Figure 2.2: Interpretation of the compactivity and entropy in terms of different packings. See also Fig. 1.1.

by increasing its entropy. Such an example will be made more explicit in the derivation of the Boltzmann equation for granular materials. At volume fractions beyond the RCP (and at atmospheric pressure) the system is not able to explore the configurations as they can only be achieved by the partial crystallisation of the sample, where there are very few configurations available.

It becomes clear from Eq. (4.19) that the compactivity is only applicable in equilibrated jammed states. As an analogue of temperature, it should also obey the zero-th law of thermodynamics. Hence, two different powders in physical contact with one another should equilibrate at the same compactivity, given a mechanism of momentum transfer between the two systems. Indeed, we may think of an appropriate laboratory experiment which would test this hypothesis under certain conditions necessary for creating the analogous situation to heat flow.

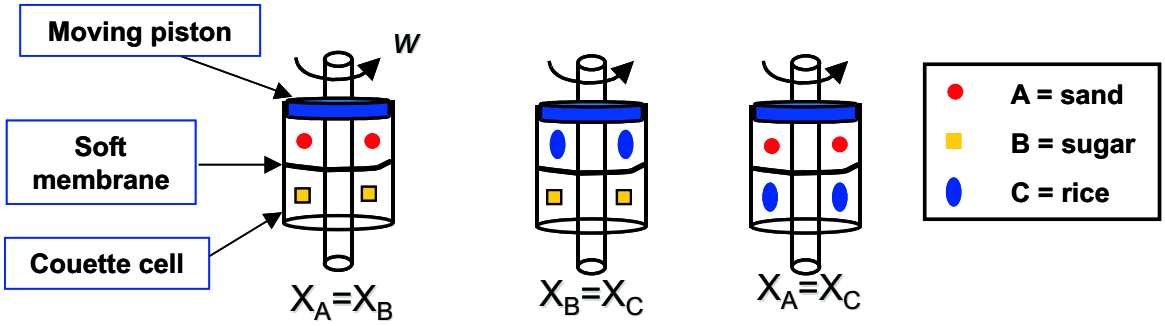

Figure 2.3: ABC experiment to test the zero-th law of granular thermodynamics.

Two powders, A and B, of different grain types are poured into a vertical couette cell as shown in Fig. 2.3. The grains must experience an equivalent tapping or shearing regime, which is achieved by the rotation of the inner cylinder of the couette cell. The species are separated by a flexible diaphragm, such that momentum transfer between the two systems is ensured. The two powders must be well separated such that there is no mixing involved, but in contact nevertheless. The grains are kept at a constant pressure by a piston which is allowed to move freely to accommodate for the changes in volume experienced by the two types of grains. Gravity may play a role in the experiment, which is avoided by density matching the particles with a suspending fluid.

The experiment consists in placing powders A and B together in the above cell and slowly shearing them at a given velocity. The powders should come to equilibrium volumes V_A and V_B, with equivalent respective compactivities, $X_A = X_B = X$. While it is easy to measure the volumes of the two systems, the measurement of their compactivities employs more sophisticated methods, discussed in Chapter 4. In the absence of a compactivity scale, we use powder B as a 'thermometer' by placing it in contact with a third powder C. The volume B is

kept at V_B and the volume of C is allowed to fluctuate until it reaches the equilibrium state. Finally, powders A and C are put together to test if they will reach the same volumes as they did in previous runs in contact with B, thus proving the zeroth law.

2.2.3 Remarks

To summarise, the granular thermodynamics is based on two postulates:

1) While in the Gibbs construction one assumes that the physical quantities are obtained as an average over all possible configurations at a given energy, the granular ensemble consists of only the jammed configurations at the appropriate volume.

2) As in the microcanonical equilibrium ensemble, the strong ergodic hypothesis is that all jammed configurations of a given volume can be taken to have equal statistical probabilities.

The ergodic hypothesis for granular matter was treated with skepticism, mainly because a real powder bears knowledge of its formation and the experiments are therefore history dependent. Thus, any problem in soil mechanics or even a controlled pouring of a sand pile does not satisfy the condition of all jammed states being accessible to one another as ergodicity has not been achieved, and the thermodynamic picture is therefore not valid. This point has been discussed in Section 1.2. The Chicago experiments of tapping columns [31] showed the existence of reversible situations. For instance, let the volume of the column be $V(n, \Gamma)$ where n is the number of taps and Γ is the strength of the tap. If one first obtain a volume $V(n_1, \Gamma_1)$, and then repeat the experiment at a different tap intensity and obtain

$V(n_2, \Gamma_2)$, when we return to tapping at (n_1, Γ_1) one obtains a volume V' which is $V'(n_1, \Gamma_1) = V(n_1, \Gamma_1)$. Moreover, in simulations of slowly sheared granular systems the ergodic hypothesis was shown to work [20].

It is often noted in the literature that although the simple concept of summing over all jammed states which occupy a volume V works, there is no first principle derivation of the probability distribution of the Edwards ensemble as it is provided by Liouville's theorem for equilibrium statistical mechanics of liquids and gases. In granular thermodynamics there is no justification for the use of the $\mathcal{W}$ function to describe the system as Liouville's theorem justifies the use of the energy in the microcanonical ensemble. In Section 2.4 we will provide an intuitive proof for the use of $\mathcal{W}$ in granular thermodynamics by the analogous proof of the Boltzmann equation.

The comment was also made that there is no proof that the entropy Eq. (3.3) is a rigorous basis for granular statistical mechanics. In the next section we will develop a Boltzmann equation for jammed systems and show that this analysis can be used to produce a second law of thermodynamics, $\delta S \geq 0$ for granular matter, and the equality only comes with Eq. (3.3) being achieved.

Although everyone believes that the second law of thermodynamics is universally true in thermal systems, the only accessible proof comes in the Boltzmann equation, as the ergodic theory is a difficult branch of mathematics which will not be covered in the present discussion. By investigating the assumptions and key points which led to the derivation of the Boltzmann equation in thermal systems, it is possible to draw analogies for an equivalent derivation in jammed systems.

It should be noted that there is an extensive literature on granular gases [26, 27],

which are observed when particles are fluidised by vigorous shaking, thus inducing continuous particle collisions. There is a powerful literature on this topic, but it is not applicable to the problem of jamming.

2.3 The Classical Boltzmann Equation

Entropy in thermal systems satisfies the second law,

$$\frac{\partial S}{\partial t} \geq 0, \tag{2.10}$$

which states that there is a maximum entropy state which, according to the evolution in Eq. (2.10), any system evolves toward, and reaches at equilibrium. A 'semi'-rigorous proof of the Second Law was provided by Boltzmann (the well-known 'H-theorem'), by making use of the 'classical Boltzmann equation', as it is now known.

In order to derive this equation, Boltzmann made a number of plausible assumptions concerning the interactions of particles, without proving them rigorously. The most important of these assumptions were:

- The collision processes are dominated by two-body collisions (Fig. 2.4a). This is a plausible assumption for a dilute gas, since the system is of very low density, and the probability of there being three or more particles colliding is infinitesimal.

- Collision processes are uncorrelated, i.e. all memory of the collision is lost on completion and is not remembered in subsequent collisions: the famous

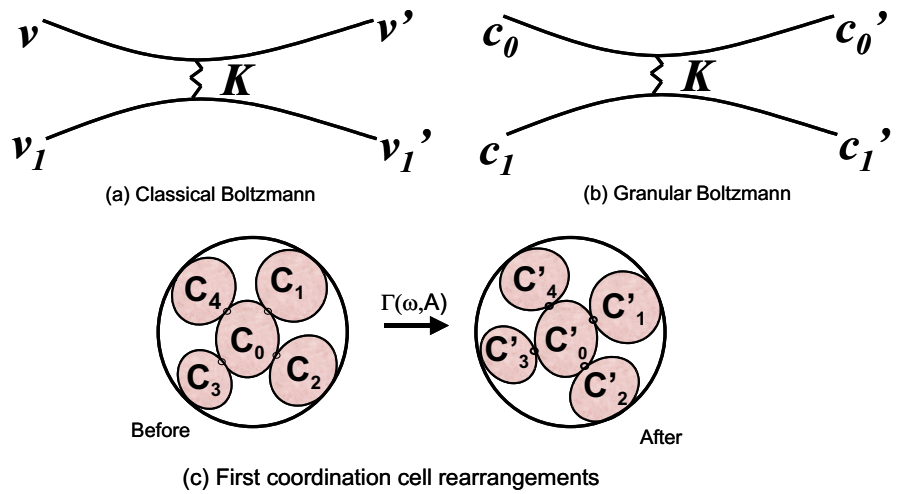

Figure 2.4: (a) Collision of two particles in a dilute gas. (b) "Collision of two configurations" given in terms of two contact points in a jammed material. (c) Rearrangements inside a pocket of mobile grains under the first coordination shell approximation for grain $\alpha = 0$.

Stosszahlansatz. This is also valid only for dilute gases, but the proof is more subtle.

Thus, Boltzmann proves Eq. (2.10) for a dilute gas only, but this is a readily available situation. The remaining assumptions have to do with the kinematics of particle collisions, i.e. conservation of kinetic energy, conservation of momentum, and certain symmetry of the particle scattering cross-sections.

Let $f(v, r)$ denote the probability of a particle having a velocity v at position r. This probability changes in time by virtue of the collisions. The two particle collision is visualised in Fig. 2.4a where v and v_1 are the velocities of the particles before the collision and v' and v_1' after the collision.

On time scales larger than the collision time, momentum and kinetic energy conservation apply:

$$mv + mv_1 = mv' + mv_1', \ \frac{1}{2}mv^2 + \frac{1}{2}mv_1^2 = \frac{1}{2}mv'^2 + \frac{1}{2}mv'^2_1. \tag{2.11}$$

Then, the distribution $f(v, r)$ evolves with time according to

$$\frac{\partial f}{\partial t} + v\frac{\partial f}{\partial r} + \int \mathcal{K}(v, v'; v_1, v_1') \ \Big(f(v)f(v_1) - f(v')f(v_1')\Big) \ d^3v_1 d^3v' d^3v_1' = 0. \tag{2.12}$$

The kernel $\mathcal{K}$ is positive definite and contains δ-functions to satisfy the conditions (2.11), the flux of particles into the collision and the differential scattering cross-section. We consider the case of homogeneous systems, i.e. $f = f(v)$, and define

$$S = -k_B \int f \log f. \tag{2.13}$$

Defining $x = ff_1/f'f_1'$ we obtain

$$\frac{\partial S}{\partial t} = \int \mathcal{K} \ \log x \ (1 - x) d^3v_1 \ d^3v' \ d^3v_1', (1 - x) \log x \geq 0, \mathcal{K} \geq 0. \tag{2.14}$$

Hence $\partial S/\partial t \geq 0$ (see standard text books on statistical mechanics).

It is also straightforward to establish the equilibrium distribution where $\partial S/\partial t = 0$ since it occurs when the kernel term vanishes. This occurs when the condition of detailed balance is achieved, $x = 1$:

$$f(v)f(v_1) = f(v')f(v_1'). \tag{2.15}$$

The solution of Eq. (2.15) subjected to the condition of kinetic energy conservation

is given by the Boltzmann distribution

$$f(v) = \left(\frac{k_B T}{m\pi}\right)^{3/2} \; e^{-\frac{1}{2}\beta m v^2}, \tag{2.16}$$

where $\beta = 1/k_B T$. Equation (2.16) is a reduced distribution and valid only for a dilute gas. The Gibbs distribution represents the full distribution and is obtained by replacing the kinetic energy in (2.16) by the total energy of the state to obtain:

$$P(E) \sim e^{-\beta E}. \tag{2.17}$$

The question is whether a similar form can be obtained in a granular system in which we expect

$$P(\mathcal{W}) \sim e^{-\mathcal{W}/\lambda X}, \tag{2.18}$$

where X is the compactivity in analogy with $T = \partial E/\partial S$. Such an analysis is shown in the next section in an approximate manner.

2.4 'Boltzmann Approach' to Granular Matter

The analogous approach to granular materials consists in the following: the creation of an ergodic grain pile suitable for a statistical mechanics approach via a method for the exploration of the available configurations analogous to Brownian motion, the definition of the discrete elements tiling the granular system via the volume function $\mathcal{W}$ (the sum of which provides the analogous 'Hamiltonian' to the energy in thermal systems), and an equivalent argument for the energy conserva-

tion expressed in terms of the system volume necessary for the construction of the Boltzmann equation.

We have already established the necessity of preparing a granular system adequate for real statistical mechanics so as to emulate ergodic conditions. The grain motion must be well-controlled, as the configurations available to the system will be dependent upon the amount of energy/power put into the system. This pretreatment is analogous to the averaging which takes place inherently in a thermal system and is governed by temperature.

As explained, the granular system explores the configurational landscape by the external tapping introduced by the experimentalist. The tapping is characterised by a frequency and an amplitude (ω, Γ) which cause changes in the contact network, according to the strength of the tap. The magnitude of the forces between particles in mechanical equilibrium and their confinement determine whether each particle will move or not. The criterion of whether a particular grain in the pile will move in response to the perturbation will be the Mohr-Coulomb condition of a threshold force, above which sliding of contacts can occur and below which there can be no changes. The determination of this threshold involves many parameters, but it suffices to say that a rearrangement will occur between those grains in the pile whose configuration and neighbours produce a force which is overcome by the external disturbance.

The concept of a threshold force necessary to move the particles implies that there are regions in the sample in which the contact network changes and those which are unperturbed, shown in Fig. 2.5. Of course, since this is a description of a collective motion behaviour, the region which can move may expand or contract,

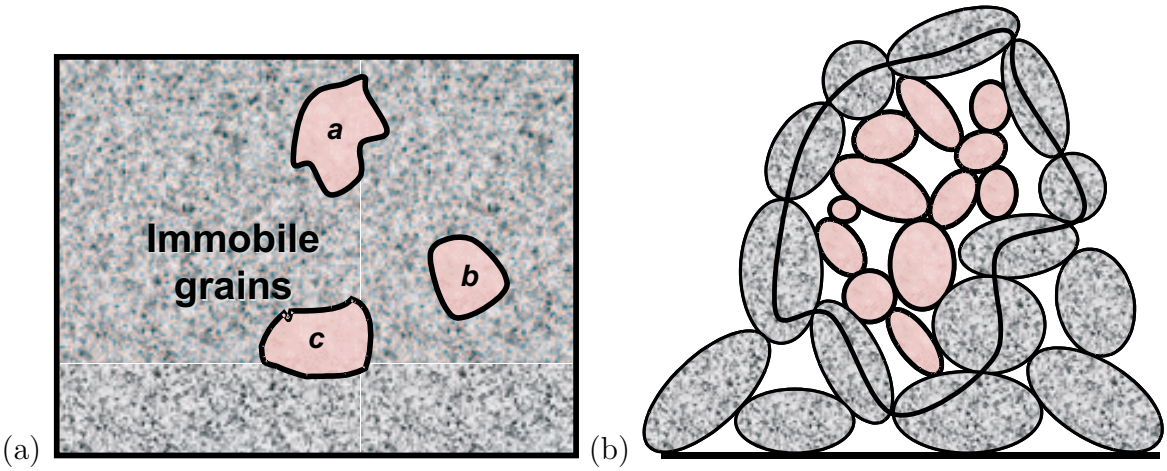

Figure 2.5: (a) Regions of mobile grains a, b, c in a matrix of immobile grains below the Coulomb threshold. (b) Detail of pocket of mobile grains a surrounded by immobile grains which are shaded.

but the picture at any moment in time will contain pockets of motion encircled by a static matrix. Each of these pockets has a perimeter, defined by the immobile grains. It is then possible to consider the configuration before and after the disturbance inside this well-defined geometry.

The present derivation assumes the existence of these regions. It is equivalent to the assumption of a dilute gas in the classical Boltzmann equation, although the latter is readily achieved experimentally.

The energy input must be on the level of noise, such that the grains largely remain in contact with one another, but are able to explore the energy landscape over a long period of time. In the case of external vibrations, the appropriate frequency and amplitude can be determined experimentally for different grain types, by investigating the motion of the individual grains or by monitoring the changes in the overall volume fraction over time. It is important that the amplitude does not exceed the gravitational force, or else the grains are free to fly up in the air,

re-introducing the problem of initial creation just as they would if they were simply poured into another container.

Within a region a we have a volume $\sum_{\alpha\in a}\mathcal{W}^{\alpha}$ and after the disturbance a volume which is now $\sum_{\alpha\in a}\mathcal{W}'^{\alpha}$ as seen in Fig. 2.4c. In Section 2.2.1 we have discussed how to define the volume function $\mathcal{W}^{\alpha}$ as a function of the contact network. Here the simplest "one grain" approximation is used as the "Hamiltonian" of the volume as defined by Eq. (2.6). In reality it is much more complicated, and although there is only one label α on the contribution of grain α to the volume, the characteristics of its neighbours may also appear. Instead of energy being conserved, it is the total volume which is conserved while the internal rearrangements take place within the pockets described above. Hence

$$\sum_{\alpha\in a}\mathcal{W}^{\alpha}=\sum_{\alpha\in a}\mathcal{W}'^{\alpha} \tag{2.19}$$

We now construct a Boltzmann equation. Suppose z particles are in contact with grain $\alpha=0$, as seen in Fig. 2.4c. For rough particles $z=4$ while for smooth $z=6$ at the isostatic limit (see Chapter 4.19). The probability distribution will be of the contact points which are represented by the tensor $\mathcal{C}^{\alpha}$, Eq. (2.5), for each grain, where α ranges from 0 to 4 in this case. So the analogy of $f(v)$ for the Boltzmann gas equation becomes $f(\mathcal{C}^{0})$ for the granular system and represents the probability that the external disturbance causes a particular motion of the grain. We therefore wish to derive an equation

$$\frac{\partial f(\mathcal{C}^0)}{\partial t} + \int \mathcal{K}(\mathcal{C}^\alpha, \mathcal{C}'^\alpha) \ \left(f_0 f_1 f_2 f_3 f_4 - f'_0 f'_1 f'_2 f'_3 f'_4 \right) \ d\mathcal{C}'^0 \prod_{\alpha \neq 0} d\mathcal{C}^\alpha d\mathcal{C}'^\alpha = 0 \quad (2.20)$$

The term $\mathcal{K}$ contains the condition that the volume is conserved (2.19), i.e. it must contain $\delta(\sum \mathcal{W}^\alpha - \sum \mathcal{W}'^\alpha)$. The cross-section is now the compatibility of the changes in the contacts, i.e. $\mathcal{C}^\alpha$ must be replaced in a rearrangement by $\mathcal{C}'^\alpha$, Fig. 2.4b (unless these grains part and make new contacts in which case a more complex analysis is called for). We therefore argue that the simplest $\mathcal{K}$ will depend on the external disturbance Γ, ω and on $\mathcal{C}^\alpha$ and $\mathcal{C}'^\alpha$, i.e.

$$\frac{\partial f(\mathcal{C}^0)}{\partial t} + \int \delta\Big(\sum_\alpha \mathcal{W}^\alpha - \sum_\alpha \mathcal{W}'^\alpha \Big) \, \mathcal{J}(\mathcal{C}^\alpha, \mathcal{C}'^\alpha) \ \Big(\prod_{\alpha=0}^{z} f_\alpha - \prod_{\alpha=0}^{z} f'_\alpha \Big) d\mathcal{C}'^0 \prod_{\alpha \neq 0} d\mathcal{C}^\alpha d\mathcal{C}'^\alpha = 0 \quad (2.21)$$

where $\mathcal{J}$ is the cross-section and it is positive definite.

The Boltzmann argument now follows. As before

$$S = -\lambda \int f \log f, x = \frac{f_0 f_1 f_2 f_3 f_4}{f'_0 f'_1 f'_2 f'_3 f'_4}, \quad (2.22)$$

and

$$\frac{\partial S}{\partial t} \geq 0, \quad (2.23)$$

the equality sign being achieved when $x = 1$ and

$$f_\alpha = \frac{e^{-\mathcal{W}^\alpha / \lambda X}}{Z}, \quad (2.24)$$

with the partition function

$$Z = \sum_{\alpha} e^{-\mathcal{W}^{\alpha}/\lambda X} \quad \Theta^{\alpha}, \tag{2.25}$$

and the analogue to the free energy being $Y = -X \ln Z$, and $X = \partial V/\partial S$.

The detailed description of the kernel $\mathcal{K}$ has not been derived as yet due to its complexity. Just as Boltzmann's proof does not depend on the differential scattering cross section, only on the conservation of energy, in the granular problem we consider the steady state excitation externally which conserves volume, leading to the granular distribution function, Eq. (2.24).

It is interesting to note that there is a vast and successful literature of equilibrium statistical mechanics based on $\exp(-\mathcal{H}/k_B T)$, but a meagre literature on dynamics based on attempts to generalise the Boltzmann equation or, indeed, even to solve the Boltzmann equation in situations remote from equilibrium where it is still completely valid. It means that any advancement in understanding how it applies to analogous situations is a step forward.

Chapter 3

A Phase Diagram For Jammed Matter

The problem of finding the most efficient way to pack spheres has an illustrious history, dating back to the crystalline arrays conjectured by Kepler [42] and the random geometries explored by Bernal [40]. This problem is as much of interest to the mathematician's pencil as it is to the granular processing industry all the way to the fruit packing in every corner grocery [43]. There are presently numerous experiments showing that the loosest way to pack spheres gives a density of $\sim$ 55% (named random loose packing, RLP [41, 44, 45]) while compactifying results in a maximum density of $\sim$ 64% (named random close packing, RCP [40, 41, 45]). While those values seem robustly true, to this date there is no physical interpretation for them. Here we show that random packings of hard spheres in 3d cannot pack above $\sim$ 63.4 %. This limit arises from a statistical picture of jammed states [46] in which the RCP can be interpreted as the ground state of the

ensemble of jammed matter. The results presented lead to a phase diagram that provides a common view of the hard sphere packing problem and further shedding light on a diverse spectrum of data, including the RLP state.

3.1 Nature of the random loose and random close packing of spheres

Difficulties in describing static granular materials and other jammed systems, such as compressed emulsions, stem from the lack of well-defined conservation laws on which a statistical description of the system is based. Unlike equilibrium statistical mechanics, energy no longer describes the microstates of the system due to the dissipative and athermal nature of jammed matter. Thus, many experimental and theoretical studies focus on the analysis of the system volume as the analogue of system energy in equilibrium thermal systems [46, 1, 39, 38, 47, 48, 49, 50, 51, 52]. Recent advances in X-ray tomography [48] and confocal microscopy [53] have revealed the detailed internal structure of jammed matter allowing for the study of the free volume per particle, denoted free volume function W [46]. By partitioning the space into a set of non-overlapping volumes with Voronoi diagrams, these studies show that W is distributed with exponential tails [48, 49, 53]. More importantly, experiments with monodisperse hard spheres [48] find that W is inversely proportional to the coordination number (number of contacts) of the particle, z.

From a theoretical perspective, the study of the ensemble of jammed matter requires an analytical form of the free volume W [46, 39, 38, 50]. We first derive the Voronoi volume in terms of the particle positions (see Appendix Section 3.2.1)

and then use statistical analysis to coarse-grain the Voronoi volume over a mesoscopic length scale, obtaining a mesoscopic free volume function (see Appendix Section 3.2.1) amenable to analytical calculations. For monodisperse hard spheres of volume V_g, we find:

$$W(z) = \frac{2\sqrt{3}}{z} V_g. \tag{3.1}$$

The inverse relation with z is in general agreement with experiments [48]. The calculation of $W(z)$ is based on the environment of the grains, where each particle is assumed to be in a uniform background field produced by the other particles and not influenced by the particle. Thus, Eq. (3.1) is akin to a mean-field theory. Quasi-particle theory makes similar assumptions; the coordination number z in Eq. (3.1) can be considered as a coarse-grained average associated with "quasiparticles" with free volume W. The key result is the relation between the Voronoi volume and the coordination number which allows to combine the volume function into a statistical mechanics approach of jammed hard spheres, by using the constraint of mechanical stability as we show below.

The canonical partition function in the volume ensemble is the starting point for the statistical mechanics of jamming [46], where the role traditionally played by the energy in thermal systems is replaced by the volume:

$$\mathcal{Q}(X) = \int g(W)\ e^{-W/X}\ \Theta_W\ dW. \tag{3.2}$$

Here X is the compactivity in units of volume [46] determining the macrostates of the system (see below for an interpretation of this temperature-like parameter), $g(W)$ is the density of jammed states for a given volume W, and Θ_W formally

imposes the condition of jamming on the ensemble through force and torque balance. The main components of the theory are the uniformity assumptions behind the calculation of the mesoscopic volume function (see Appendix Section 3.2.1), the identification of the isostatic condition with the ensemble of jammed configurations, and the derivation of the density of states, as we discuss below.

Distinguishing between metastable and mechanically stable packings that define the jammed state through the Θ_W function remains a problem under debate [56], related to the more fundamental question of whether or not a jammed packing is well-defined. In practice, it is widely believed that the isostatic condition is necessary for a jammed disordered packing [57, 58, 54, 55, 59]. That is, the number of force variables in the system is equal to the number of force and torque balance equations (see Appendix Section 3.2.2). Therefore, we consider that the Θ_W function in (3.2) restricts the ensemble to the isostatic packings.

It is important to note that the coordination number z, as defined in Eq. (3.1), refers to the geometry of the packing and does not refer to contact forces. Therefore, z can include "trivial" contacts with zero forces, not contributing to the mechanical balance. We call z the *geometrical* coordination number which is larger than the *mechanical* coordination number, $Z(\leq z)$, which includes the contacts with non-zero force (see Appendix Section 3.2.3). Then, Z directly corresponds to the isostatic condition of force and torque balance. For frictionless spherical particles (with interparticle friction coefficient $\mu = 0$, mimicking emulsion systems), the isostatic condition implies $Z = 2d = 6$ (d is the dimension of the system and in the following we work in $d = 3$). For infinitely rough particles having $\mu \to \infty$ the mechanical coordination number is $Z = d + 1 = 4$ (see Appendix Section 3.2.2

for details). Interpolating between these two limits there exist granular packings of finite μ with Z smoothly varying between $Z(\mu = 0) = 6$ and $Z(\mu \to \infty) = 4$ [59]. The relationship $Z(\mu)$ is an important assumption which is tested by numerical simulations in the Appendix Section 3.2.2 (see Fig. 3.10), where we find a common $Z(\mu)$ curve for different preparation protocols. The mechanical coordination number, Z, ranges from 4 to 6 as a function of μ, and provides a lower bound to the geometrical coordination number, $Z \leq z \leq 6$. These bounds are tested with computer simulations in Appendix Section 3.2.3.

By changing variables, Eq. (3.2) can be written as (see Appendix Section 3.2.4):

$$\mathcal{Q}_{\text{iso}}(X, Z) = \int_Z^6 e^{-W(z)/X} \; g(z) \; dz. \tag{3.3}$$

Due to the implicit volume coarse-graining in Eq. (3.1), each volume state $W(z)$ represents a mesoscopic state containing many microstates with common z and density of states $g(z)$ which can be calculated as follows (see Appendix Section 3.2.4). We consider that the packing of hard spheres is in a jammed configuration in which there can be no motion of any subset of particles leading to unjamming [60]. Thus, the configuration space of jammed matter is discrete since we cannot change one configuration continuously to another. We call the dimension per particle of the configuration space as $\mathcal{D}$ and assume that the distance between two configurations is not broadly distributed with a mean distance h_z. Therefore the number of configurations is proportional to $1/(h_z)^{\mathcal{D}}$, analogous with the one in quantum mechanics, h^{-d}, where h is the Planck constant and d the dimension. The fact that the particles are jammed by z contacting particles reduces the degrees of freedom to $\mathcal{D} - z$, and the number of configurations is then $1/(h_z)^{\mathcal{D}-z}$. Since

the term $1/(h_z)^{\mathcal{D}}$ is a constant, it will not influence the average in the partition function. Therefore, we consider $g(z) = (h_z)^z$.

From Eq. (3.3) we obtain the equations of state that define the phase diagram of jamming. We start by investigating two limiting cases (see Appendix Section 3.2.5):

(a) In the limit of vanishing compactivity ($X \to 0$), we obtain the ground state of jammed matter with a density:

$$\phi_{\mathrm{RCP}} = \frac{6}{6 + 2\sqrt{3}} \approx 0.634, \quad Z(\mu) \in [4, 6]. \tag{3.4}$$

(b) In the limit of infinite compactivity ($X \to \infty$) we obtain:

$$\begin{aligned} \phi_{\mathrm{RLP}}(Z) &= \frac{1}{\mathcal{Q}_{\mathrm{iso}}(\infty, Z)} \int_Z^6 \frac{z}{z + 2\sqrt{3}} (h_z)^z dz \\ &\approx \frac{Z}{Z + 2\sqrt{3}}, \quad Z(\mu) \in [4, 6]. \end{aligned} \tag{3.5}$$

The average in Eq. (3.5) is taken over all the states with equal probability, since $e^{-W(z)/X} \to 1$ as $X \to \infty$. The approximation in Eq. (3.5) applies since h_z is very small, and thus the most populated state, $z = Z$, is the dominant contribution to the average volume. The meaning of the subscripts RCP and RLP in (3.4) and (3.5) will become clear below.

The equations of state (3.4) and (3.5) are plotted in the (ϕ, Z) plane in Fig. 3.1 defining the phase diagram of jammed matter. The phase space is further delimited from below by the minimum coordination $Z = 4$ for infinitely rough grains, denoted the granular-line or G-line in Fig. 3.1. All mechanically stable disordered jammed packings lie within the confining limits of the phase diagram (indicated by the

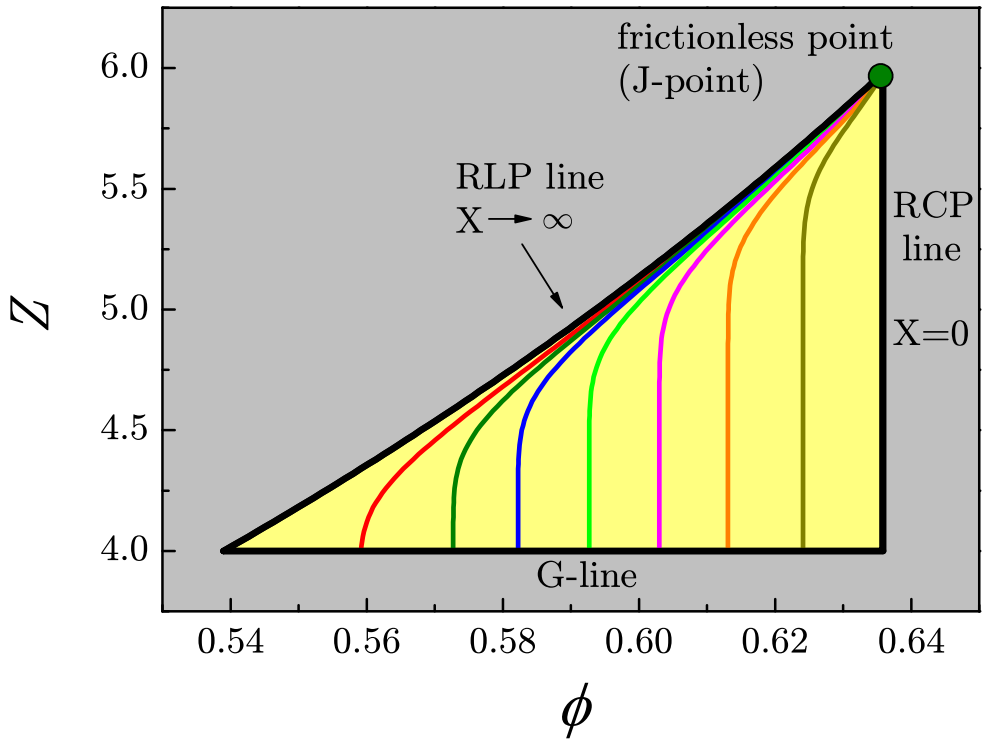

Figure 3.1: Phase diagram of jamming: Theory. Theoretical prediction of the statistical theory. All disordered packings lie within the yellow triangle demarcated by the RCP line, RLP line and G line. Lines of finite isocompactivity are in color. The grey area is the forbidden zone.

yellow zone in Fig. 3.1), while the grey shaded area in Fig. 3.1 indicates the forbidden zone. For example, a packing of frictional hard spheres with $Z = 5$ (corresponding to a granular material with interparticle friction $\mu \approx 0.2$ according to Fig. 3.10) cannot be equilibrated at volume fractions below $\phi < \phi_{\rm RLP}(Z = 5) = 5/(5 + 2\sqrt{3}) = 0.591$ or above $\phi > \phi_{\rm RCP} = 0.634$. Thus, these results provide a statistical interpretation of the RLP and RCP limits:

(i) Stemming from the statistical mechanics approach, the RCP limit arises as the result of the relation (3.4), which gives the maximum volume fraction of disordered packings. Beyond the fact that 63-64% is commonly quoted as RCP for monodisperse hard spheres [40, 41, 45], we present a physical interpretation of that value as the ground state of frictional hard spheres characterized by a given interparticle friction coefficient. In this representation, as μ varies from 0 to ∞, the RCP state changes accordingly. The present approach has led to an unexpected number of states that all lie in the RCP line from the frictionless point at $Z = 6$ to $Z = 4$ as depicted in Fig. 3.1, demonstrating that RCP is not a unique point in the phase diagram.

(ii) Equation of state (3.5) provides the lowest volume fraction for a given Z and represents a statistical interpretation of the RLP limit depicted by the RLP-line in Fig. 3.1. We predict that to the left of this line, packings are not mechanically stable or they are experimentally irreversible as discussed in [1, 47, 30]. A review of the literature indicates that there is no general consensus on the value of RLP as different estimations have been reported ranging from 0.55 to 0.60 [41, 44, 45]. The phase diagram proposes a solution to this problem. Following the infinite compactivity RLP-line, the volume fraction of the RLP decreases with increasing

friction from the frictionless point $(\phi, Z) = (0.634, 6)$ [54], denoted J-point in [55], towards the limit of infinitely rough hard spheres. Indeed, experiments [41] indicate that lower volume fractions are achieved for larger coefficient of friction. We predict the lowest volume fraction in the limit: $\mu \to \infty$, $X \to \infty$ and $Z \to 4$ ($h_z \ll 1$) at $\phi_{\rm RLP}^{\rm min} \approx \frac{4}{4+2\sqrt{3}} = 0.536$. Even though this is a theoretical limit, our results indicate that for $\mu > 1$ this limit can be approximately achieved. The finding of a random loose packing bound is an interesting prediction of the present theory. The RLP limit has been little investigated experimentally, and so far it was not certain whether this limit can or cannot be reached in real systems. Our prediction is close to the lowest stable volume fraction ever reported for monodisperse spheres, 0.550 ± 0.006 by Onoda and Liniger [44].

(iii) Between the two limits Eqs. (3.4) and (3.5), there are packings inside the yellow zone in Fig. 3.1 with finite compactivity, $0 < X < \infty$. In this case, the partition function is solved numerically obtaining $\phi(X, Z)$ along an isocompactivity line as shown in the color lines in Fig. 3.1. Since X controls the probability of each state, like in condensed matter through a Boltzmann-like factor in Eq. (3.3), it characterizes the number of possible ways to rearrange a packing having a given volume and entropy, S. Thus, the limit of the most compact and least compact stable arrangements correspond to $X \to 0$ and $X \to \infty$, respectively. Between these limits, the compactivity determines the volume fraction from RCP to RLP.

These results can be visualized in terms of a "volume landscape", analogous to the energy landscape in glasses [6]. Each jammed state (determined by the positions and rotations of the particles, denoted ξ, and its corresponding free volume W) is depicted as a point in Fig. 3.2. The volume landscape has different levels

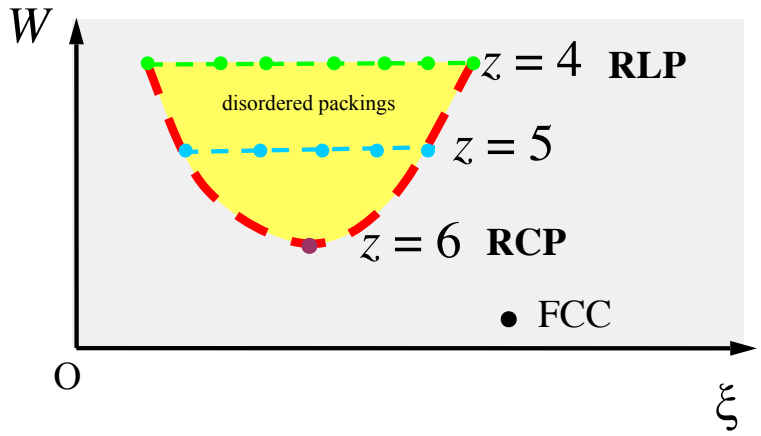

Figure 3.2: Schematic representation of the volume landscape of jammed matter (ξ, W). The multidimensional coordinate ξ represents the degrees of freedom: particle positions and rotations. Each dot represent a discrete jammed states at different z. We represent the case of $\mu = \infty$. The states represent those along the G-line in Fig. 3.1 as the compactivity varies from $X = 0$ (ground state) to $X \to \infty$ at the RLP. The horizontal lines indicate packings at constant volume. The ground state of jammed matter for this friction coefficient has $z = 6$ and the highest volume states are found for $z = 4$. For another finite μ, the space is delimited by above by a line of constant $z = Z(\mu)$. All disordered packings are in the yellow region of the phase space which corresponds to the isostatic plane of hard spheres at the jamming transition where our calculations are performed. Other ordered packings have lower volume, such as the FCC.

of constant W determined by z, analogous to energy levels in Hamiltonian systems. The lowest volume corresponds to the FCC/HCP structure (with $z = 12$), as conjecture by Kepler [42]. Other lattice packings, such as the cubic lattice and tetrahedron lattice, have higher volume levels in this representation. Beyond these ordered states, the ensemble of disordered packings is identified within the yellow area in Fig. 3.2, corresponding to a system with infinite friction. Equation (3.4) indicates that the RCP corresponds to the ground state of disordered jammed matter for a given friction which determines Z, while the RLP states are achieved for higher volume levels as indicated in Fig. 3.2.

Further statistical characterization of the jammed structures can be obtained through the calculation of the equations of state in the three-dimensional space (X, ϕ, S) as seen in Fig. 3.3 (see Appendix Section 3.2.5). Each curve in the figure corresponds to a system with a different $Z(\mu)$. The equation of state $\phi(X)$ for different values of Z can be seen in the projection of Fig. 3.3. The volume fraction diminishes with increasing compactivity according to the theoretical picture of the phase diagram. The curves $\phi(X)$ qualitatively reproduce the reversible branch of compaction curves in the experiments of [1] for shaken granular materials and oscillatory compression of grains [30] suggesting a correspondence between X and shaking amplitude. The intention is that, different control parameters in experiments could be related to a state variable, and therefore might help experimentalists to describe results obtained under different protocols. For any value of Z, there is a common limit $\phi \to \phi_{\mathrm{RCP}}$ as $X \to 0$, indicating the constant volume fraction for all the RCP states. The singular nature of the frictionless J-point is revealed as the volume fraction remains constant for any value of X, explaining

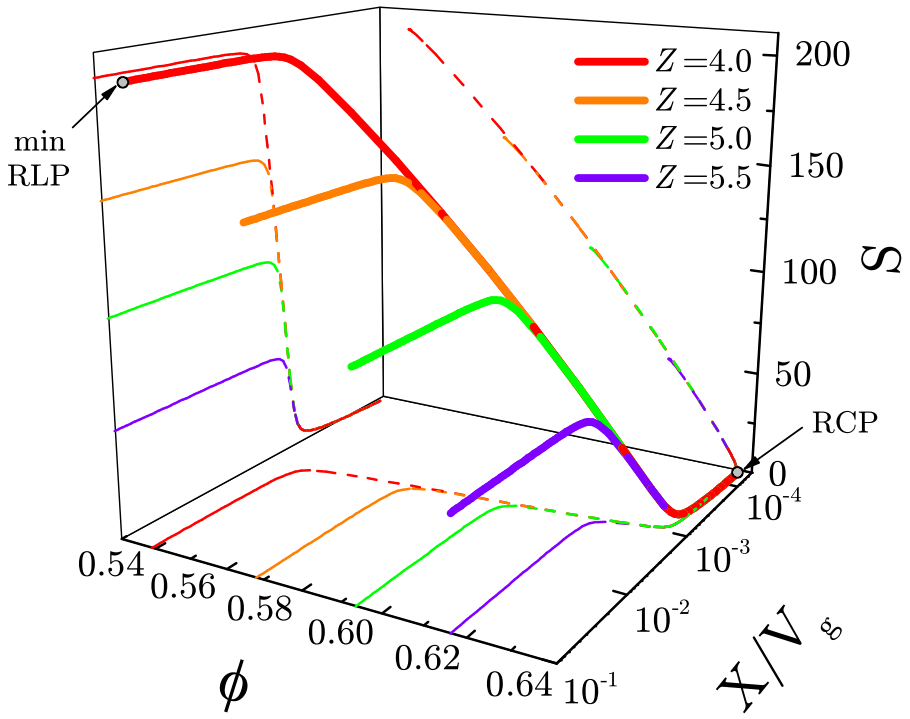

Figure 3.3: Predictions of the equation of state of jammed matter in the (X, ϕ, S) space. Each line corresponds to a different system with Z as indicated. The projection in the (X, ϕ) plane resembles qualitatively the compaction curves of the experiments [1, 47, 30].

why this point is the confluence of the isocompactivity lines, including RCP and RLP.

The existence of the theoretically inferred jammed states opens such predictions to experimental and computational investigation. We numerically test the predictions of the phase diagram by preparing monodisperse packings of Hertz-Mindlin spheres with friction coefficient μ at the jamming transition using methods previously developed [54, 61]. We achieve different packing states by compressing a system from an initial volume fraction ϕ_i with a compression rate Γ in a medium of viscosity (damping) η (see Appendix Section 3.2.6). While the simulations are not

realistic (no gravity, boundaries, or realistic protocol is employed), they provide a way to test the main predictions of the theory. We plot in Fig. 3.4 the final state (ϕ, Z) achieved by the system for every $(\phi_i, \Gamma, \eta, \mu)$ at the jamming transition of vanishing stress with a method explained in the Appendix Section 3.2.6. As in other out of equilibrium systems, such as glasses, the inherent path-dependency of jammed matter materializes in the fact that different packing structures can be realized with different preparation protocols [1, 47, 30]. Indeed, the present algorithm finds analogies with recent attempts to describe jamming using ideas coming from the theory of mean-field spin glasses and optimization problems [10, 62].

Changing the initial state ϕ_i produces different packings as seen in Fig. 3.4. As the initial volume fraction ϕ_i increases, the final volume fraction approaches the prediction of the vertical RCP line of zero compactivity as seen in the phase space in Fig. 3.4, demonstrating how to access the range of RCP states. All RCP states have approximately the same geometrical coordination number, $z \approx 6$, but differ in their mechanical one Z ranging from $Z = 6$ to $Z \approx 4$, as predicted by the theory. When considering packings prepared with the smallest ϕ_i, slower compression rates (see the inset of Fig. 3.4) or larger viscosities of the medium, we reproduce states with infinite compactivity along the RLP line in the figure. There results agree with the experiments of [44], finding RLP for slowly deposited grains. Furthermore, packings prepared with intermediate values of ϕ_i closely follow the lines of isocompactivity as seen in Fig. 3.4. Thus, with reasonable approximation and for this particular protocol, we identify the density of the initial state, ϕ_i with the compactivity of the packing, providing a way to prepare a packing with a desired compactivity. In general, all numerically generated jammed states lie

approximately within the predicted bounds of the phase diagram (see Appendix Section 3.2.6 for further details).

The numerical results suggest a way to experimentally test the existence of the predicted packings. By allowing the grains to settle in liquids of varying density, the speed of the particles can be varied and a systematic exploration of the jamming phase diagram can be achieved. Beyond the elucidation of some questions in the sphere packing problem, other problems can now be addressed systematically from the point of view of what we have learned from the phase diagram. This includes the investigation of the criticality of the jamming transition from frictionless to frictional systems by extending the phase space to (ϕ, Z, σ), with σ = stress, a characterization of jamming in the phase space of configurations, the problem of elasticity and Green's function and the study of the distribution of forces, volumes and coordination number, to name a few. An advantage of the present formalism is that it provides a classification of jammed packings from where these studies could be systematically performed.

3.2 Appendix

Here, we describe the details of the calculations leading to the phase diagram of jammed matter. The main theoretical result is the definition of the volume function based on the Voronoi volume of a particle explained in Section 3.2.1. Section 3.2.2 describes the isostatic condition that defines the ensemble of jammed matter through the Θ_W function. Section 3.2.3 explains the difference between the geometrical, z, and mechanical, Z, coordination number, which is important to

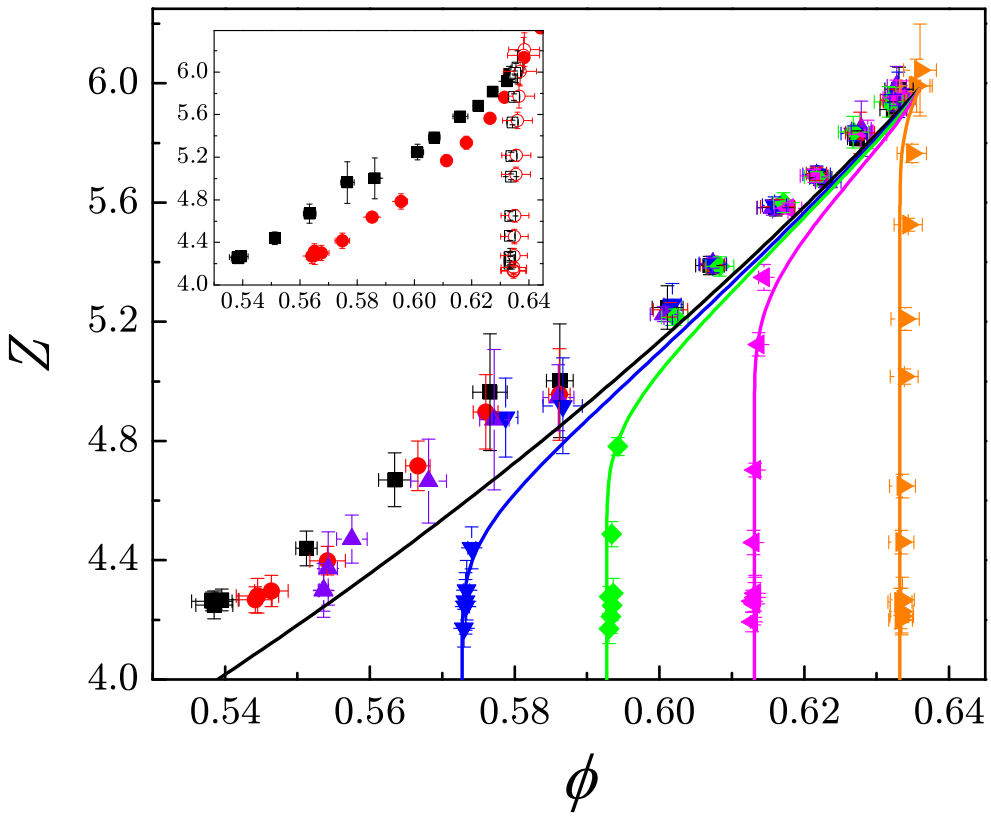

Figure 3.4: Phase diagram of jamming: Simulations. Numerical simulations demonstrate how to dynamically access the theoretically found states. The numerical protocol is parameterized by $(\phi_i, \Gamma, \eta, \mu)$. The main plot shows the dependence of the final jammed states (ϕ, Z) on ϕ_i for a fix $\Gamma = 10^{-7}$ and $\eta = 10^{-3}$. Each data point along an equal-color set represents a different μ (see Fig. 3.10 in the Appendix Section 3.2.2). Solid lines represent the theoretical results with $h_z = e^{-100}$ for different compactivities measured in units of $10^{-3}V_g$. From left to right $X = \infty$ (black solid line), 1.62 (blue solid line), 1.38 (green solid line), 1.16 (pink solid line) and 0.88 (orange solid line). The inset focuses on the dependence of (ϕ, Z) on (Γ, η) for two different ϕ_i. The error bars correspond to the s.d. over 10 realizations of the packings.

define the canonical partition function. Section 3.2.4 defines the partition function for the ensemble of jammed states under the isostatic condition, $\mathcal{Q}_{\text{iso}}$. Section 3.2.5 explains how to solve the partition function $\mathcal{Q}_{\text{iso}}$ which leads to the equations of state (3.4) and (3.5), and the phase diagram of Fig. 3.1. Finally, Section 3.2.6 explains the numerical studies to test the theoretical predictions.

3.2.1 Volume function

The aim of this section is to delineate the statistical theory for calculating the free volume, W, associated with each particle. First we find an analytical formula for the Voronoi volume of each particle. Then a statistical theory finds that the volume function is related to the coordination number:

$$W(z) = \frac{\kappa}{z} V_g, \tag{3.6}$$

where $\kappa = 2\sqrt{3}$. This free volume function is then used in the canonical partition function to calculate the phase diagram of jammed states.

Microscopic volume function

The definition of a Voronoi cell is a convex polygon whose interior consists of all points closer to a given particle than to any other (see Fig. 3.5a).

Formally, the volume of the Voronoi cell of particle i can be calculated as (see Fig. 3.5a):

$$\mathcal{W}_i^{\text{vor}} = \oint \int_0^{l_i(\hat{s})} r^{d-1} dr ds = \frac{1}{d} \oint l_i(\hat{s})^d ds, \tag{3.7}$$

where $l_i(\hat{s})$ is the distance from particle i to the boundary of its Voronoi cell in the $\hat{s}$

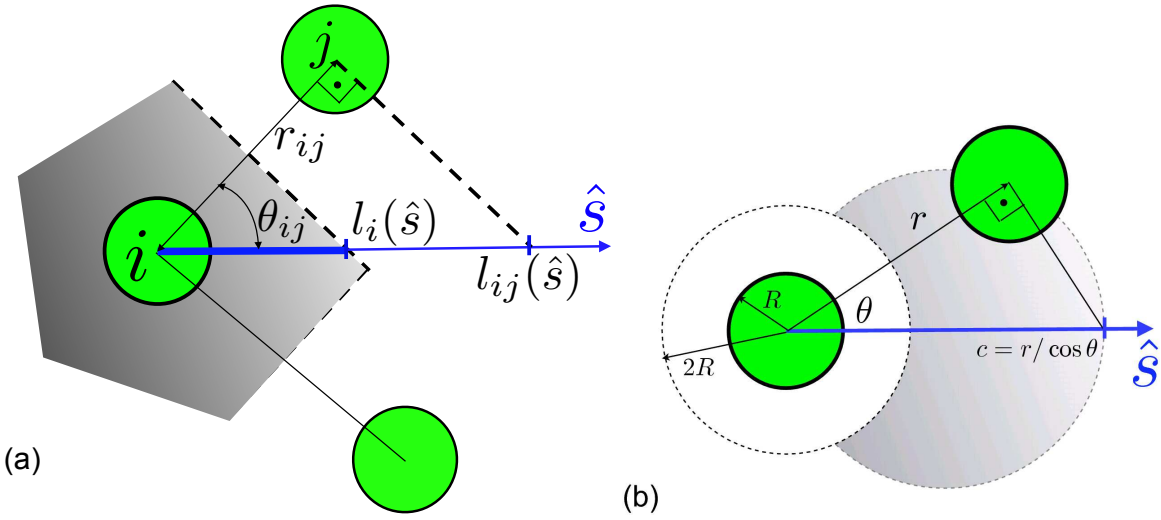

Figure 3.5: Definition of the volume function depicted in 2d for easier visualization. **a,** The Voronoi volume is the light grey area. The boundary of the Voronoi cell of particle i along the direction $\hat{s}$ is $l_i(\hat{s}) = l_{ij}(\hat{s})/2 = r_{ij}/2\cos\theta_{ij}$, where θ_{ij} is the angle between $\hat{s}$ and r_{ij}. The particle j is said to be closer, along the $\hat{s}$ direction, to i than any other particle. Then the Voronoi volume is proportional to the integration of $l_i(\hat{s})^3$ over $\hat{s}$ as in Eq. (3.8). **b,** Schematic illustration of the derivation of $P_{\rm B}(c)$. The considered particle (green) is located in the center, the closest particle in the $\hat{s}$ direction is at (r, θ), and the white area is the excluded zone $r < 2R$ for the center of any other grain. For a fixed $c = r/\cos\theta$, the light grey area is the region of the plane (r', θ') where $r'/\cos\theta' < c$. The computation of $P_{\rm B}$ involves the calculation of this volume as explained in the text.

direction, and d is the dimension. If one denotes the distance from particle i to any particle j as $\vec{r}_{ij} = r_{ij}\hat{r}_{ij}$ and its projection along the $\hat{s}$ direction as $l_{ij}(\hat{s}) \equiv r_{ij}/(\hat{s} \cdot \hat{r}_{ij})$, then $l_i(\hat{s})$ is the minimum of $l_{ij}(\hat{s})/2$ over all particles j for any $l_{ij}(\hat{s}) > 0$ (see Fig. 3.5a). This leads to $l_i(\hat{s}) = \min_{l_{ij}(\hat{s})>0} l_{ij}(\hat{s})/2 = \min_{\hat{s}\cdot\hat{r}_{ij}>0} \frac{r_{ij}}{2\hat{s}\cdot\hat{r}_{ij}}$. Substituting into Eq. (3.7), we find that the volume of the Voronoi cell of particle i is:

$$\mathcal{W}_i^{\rm vor} = \frac{1}{d}\oint (\min_{\hat{s}\cdot\hat{r}_{ij}>0} \frac{r_{ij}}{2\hat{s}\cdot\hat{r}_{ij}})^d ds. \tag{3.8}$$

The geometrical interpretation of this formula is given in Fig. 3.5a. Equation

(3.8) is relevant in that *(i)* it provides a formula for the Voronoi volume for any dimension in terms of the particle positions or contact network r_{ij}, and *(ii)* it allows for the calculation of macroscopic observables via statistical mechanics. However, further analytical developments are difficult since the volume function of a single particle depends on all particle positions in the system, implying intrinsically strong correlations. Such correlations are implicit in the global minimization of Eq. (3.8) which, in practice, is restricted to a few coordination shells, defining a mesoscopic Voronoi length scale. Next we present a theory of volume fluctuations to coarse grain $\mathcal{W}_i^{\text{vor}}$ over this mesoscopic length scale. The coarsening reduces the degrees of freedom r_{ij} to one variable, the geometrical coordination number z, and defines a mesoscopic volume function amenable to statistical calculations.

Equation (3.8) can be rewritten as $\mathcal{W}_i^{\text{vor}} = \frac{1}{\oint ds} \oint \mathcal{W}_i^s ds = \langle \mathcal{W}_i^s \rangle_s$, where we define the orientational volume for the i particle in the $\hat{s}$ direction as:

$$\mathcal{W}_i^s \equiv V_g \left(\frac{1}{2R} \min_{\hat{s}\cdot\hat{r}_{ij}>0} \frac{r_{ij}}{\hat{s}\cdot\hat{r}_{ij}} \right)^d . \tag{3.9}$$

The two volumes (3.8) and (3.9) are additive and tile the system so that the total system volume is $V = \sum_i \mathcal{W}_i^{\text{vor}} = \sum_i \langle \mathcal{W}_i^s \rangle_s$. For isotropic packings, $\mathcal{W}_i^s$ (without the orientational average over $\hat{s}$) is also additive since the choice of orientation $\hat{s}$ is arbitrary. Thus, we obtain:

$$V = \sum_i \langle \mathcal{W}_i^s \rangle_s = \langle \sum_i \mathcal{W}_i^s \rangle_s = \sum_i \mathcal{W}_i^s . \tag{3.10}$$

This property reduces the number of calculations, since there is no need for an

orientational average. The free volume function is defined as

$$W = \mathcal{W} - V_g, \tag{3.11}$$

and the reduced free volume function w for isotropic systems is defined as:

$$w \equiv \langle w^s \rangle_i \equiv \left\langle \frac{\mathcal{W}_i^s - V_g}{V_g} \right\rangle_i = \left\langle \left(\frac{1}{2R} \min_{\hat{s}\cdot\hat{r}_{ij}>0} \frac{r_{ij}}{\hat{s}\cdot\hat{r}_{ij}} \right)^d - 1 \right\rangle_i . \tag{3.12}$$

The isotropic free volume function (3.12) requires averaging over the particles i but not over $\hat{s}$. The more general form (3.8) allows study of anisotropic systems, a case left for future work.

Mesoscopic volume function

Next, we follow a statistical analysis to find the mesoscopic volume function by averaging the single grain function of Eq. (3.12). For a given grain i, the calculation of (3.12) reduces to finding the ball with $\min_j r_j/\cos\theta_j$, where the minimization is over all the grains j (see Fig. 3.5b for notation, here $r_j = r_{ij}$, $\cos\theta_j = \hat{s}\cdot\hat{r}_{ij}$, and we have set $2R = 1$ for simplicity and we now work in $3d$). We consider that the particle minimizing $r_j/\cos\theta_j$ is located at (r,θ) with $c = r/\cos\theta$ along the $\hat{s}$ direction (see Fig. 3.5b). We compute the inverse cumulative distribution function $P_>(c)$ to find all the particles j with $r_j/\cos\theta_j > c$. Thus, $P_>(c)$ is the probability that all particles have $r_j/\cos(\theta_j)$ larger than c. The mesoscopic free volume function is then obtained as the mean value $w \equiv \langle w^s \rangle_i = \langle c^3 \rangle - 1$ over the

probability density $-\frac{dP_>(c)}{dc}$, and therefore

$$w = \langle w^s \rangle_i = \int_1^\infty (c^3 - 1) \frac{d[1 - P_>(c)]}{dc} dc = -\int_1^\infty (c^3 - 1) \frac{dP_>(c)}{dc} dc = \\ = -\int_1^0 (c^3 - 1) dP_> = \int_0^1 (c^3 - 1) dP_>. \tag{3.13}$$

The integration in Eq. (13) ranges from 1 to ∞ respect to c since the minimum distance for a ball is for $r = 1$ and $\theta = 0$ which gives $c = 1$ and the maximum is at $r \to \infty$. When changing variables to $dP_>$, the limits of integration $c : [1, \infty)$ correspond to the inverse cumulative distribution function $P_> : [1, 0]$.

The inverse cumulative distribution function $P_>(c)$ has two contributions: from the contact balls, $P_{\rm C}(c)$, and from the balls in the bulk, $P_{\rm B}(c)$. $P_{\rm C}(c)$ is a surface term that depends on z while $P_{\rm B}(c)$ is the bulk contribution depending on the density of particles. Geometrically, they represent the probabilities for a particle in contact or in the bulk, respectively, to be located outside the light grey area in Fig. 3.5b, and therefore not contributing to the volume c^3. The contributions are assumed to be independent of each other, then $P_>(c) = P_{\rm B}(c) P_{\rm C}(c)$.

The background is assumed uniform, with mean free volume density $\rho(w) = N/(NV_g\phi^{-1} - NV_g) = 1/(V_g w)$ and inverse volume fraction $\phi^{-1} = w + 1$, and therefore $P_{\rm B}$ assumes a Boltzmann-like distribution of the form:

$$P_{\rm B}(c) = e^{-\rho(w) V^*(c)}, \tag{3.14}$$

where $V^*(c) = 2\pi \int_1^\infty \int_0^{\pi/2} \Theta(c - r/\cos\theta) d\vec{r}$ is the volume of the light grey area in

Fig. 3.5b. We obtain:

$$V^*(c) = V_g \left((c^3 - 1) - 3(1 - \frac{1}{c}) \right). \tag{3.15}$$

Therefore,

$$P_{\mathrm{B}}(c) = \exp\left[- \left((c^3 - 1) - 3(1 - 1/c) \right) / w \right]. \tag{3.16}$$

Similarly, the contact contribution is

$$P_{\mathrm{C}}(c) = e^{-\rho_S S^*(c)}, \tag{3.17}$$

where

$$S^*(c) = 2\pi \int_0^{\arccos(1/c)} \sin\theta d\theta = 2\pi(1 - \frac{1}{c}), \tag{3.18}$$

and $\rho_S(z)$ is the mean free surface density (the surface analogue of $\rho(w)$).

The contact distribution can be written as $P_C(c) = \exp(-zS^*(c)/S_f)$, where S_f is determined by the mean of $S^*(c)$, $\langle S \rangle$, as $\rho_S(z) \equiv 1/\langle S \rangle = z/S_f$. The exponential distribution is analogous to the background form $P_B(c)$ where we consider $\rho_S(z)$ as the mean free surface density [the surface analogue of $\rho(w)$] representing the inverse of the average area along one direction $\hat{s}$ left free by z contact balls. Formally, S_f is calculated by locating at random z non-overlapping spheres in contact with a given particle. For a given direction $\hat{s}$, the closest particle to $\hat{s}$ defines the angle θ^* from where the free surface is calculated as $S_f = 2\pi(1 - \cos\theta^*)$. In order to estimate the value of S_f, we first calculate the mean of $\cos\theta^*$ for a single particle $z = 1$, which is equal to $S_f = 2\pi$, since $\cos\theta^*$ ranges uniformly from 1 to -1. In the case of many contact particles, $z > 1$, many body constraints imply that the

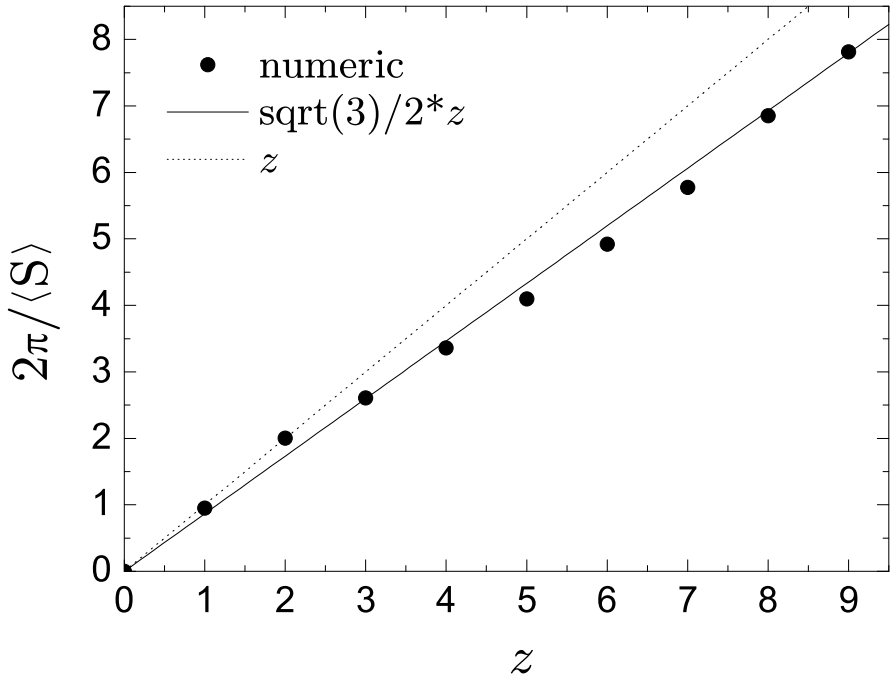

Figure 3.6: A numerical calculation of hard spheres confirms that $2\pi\rho_S(z) = \frac{2\pi}{\langle S\rangle}$ is better approximated by $\frac{\sqrt{3}}{2}z$ than z.

free surface should be corrected by the solid angle extended by a single ball. Thus, up to first order approximation, $S_f \approx 2\pi + S_{\rm occ}$, where $S_{\rm occ} = 2\pi\int_0^{\pi/6}\sin\theta d\theta = 2\pi(1-\sqrt{3}/2)$ is the surface occupied by a single contact ball. This analysis suggests that the surface term can be approximated as $\rho_S(z) \approx z\sqrt{3}/(4\pi)$, a result that is confirmed by computer simulations in Fig. 3.6. This numerical calculation considers randomly locating z non-overlapping spheres in contact with a given particle. The sphere closest to the direction $\hat{s}$ defines the free angle θ^* and the free surface $S_f = 2\pi(1-\cos\theta^*)$. We find:

$$P_{\rm C}(c) = \exp[-\sqrt{3}z(1-1/c)/2]. \tag{3.19}$$

The inverse cumulative distribution is then:

$$P_{>}(c) = \exp\left[-\frac{1}{w}\left((c^3-1) - 3(1-\frac{1}{c})\right) - \frac{\sqrt{3}}{2}z(1-\frac{1}{c})\right]. \tag{3.20}$$

Substituting into Eq. (3.13), we obtain a self-consistent equation to calculate w:

$$w = \int_0^1 (c^3-1)\ \ d\exp\left[-\frac{1}{w}\left((c^3-1) - 3(1-\frac{1}{c})\right) - \frac{\sqrt{3}}{2}z(1-\frac{1}{c})\right]. \tag{3.21}$$

Since $w = \int_0^1 (c^3-1) d\exp[-(c^3-1)/w]$, then Eq. (3.21) can be solved exactly. We start from the identity: $\int_0^\infty x/w \exp(-x/w)dx = w$,

$$1 = \int_0^1 \frac{1}{w}\left((c^3-1) - \alpha(1-\frac{1}{c})\right) d\exp\left[-\frac{1}{w}\left((c^3-1) - \alpha(1-\frac{1}{c})\right)\right], \tag{3.22}$$

where $\alpha = 3 - wz\sqrt{3}/2$. Or

$$\begin{aligned} 0 &= \int_0^1 \frac{1}{w}(c^3-1) d\exp\left[-\frac{1}{w}\left((c^3-1) - \alpha(1-\frac{1}{c})\right)\right] - 1 = \\ &= \alpha \int_0^1 \frac{1}{w}\left(1-\frac{1}{c}\right) d\exp\left[-\frac{1}{w}\left((c^3-1) - \alpha(1-\frac{1}{c})\right)\right]. \end{aligned} \tag{3.23}$$

The second integration in the right hand side is equal to zero only at $w = 0$ or $w \to \infty$, which correspond to two trivial solutions at $\phi = 1$ and $\phi = 0$ respectively. The only non-trivial solution happens at $\alpha = 0$, and therefore $w = 2\sqrt{3}/z$. To see why there are no other solutions, we see that the equation is of the form $\alpha \times I = 0$, where I stands for the second integration. Therefore, all the solutions are for $\alpha = 0$

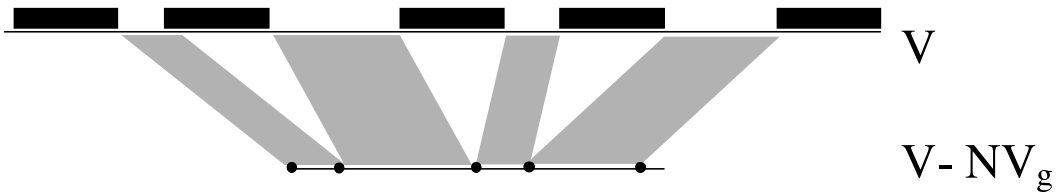

Figure 3.7: A mapping between hard sphere and ideal gas in the one dimensional system.

or $I = 0$. $I = 0$ gives us the two trivial solution and $\alpha = 0$ gives one non-trivial solution, completing the solution space of the original equation.

Thus, we arrive at the mesoscopic free volume function which is amenable to analytical calculations:

$$w = \frac{2\sqrt{3}}{z} \quad \Rightarrow \quad W = \frac{2\sqrt{3}}{z} V_g. \tag{3.24}$$

Equation (3.24) is a coarse-grained "Hamiltonian" or volume function that replaces the microscopic Eq. (3.8) in describing the mesoscopic states of jammed matter. While Eq. (3.8) is difficult to treat analytically, since it requires a field theory, the advantage of the mesoscopic Eq. (3.24) is that the partition function can be solved analytically since W depends on z only, instead of r_{ij}.

Test of the assumptions of the theory.

Below we test the different assumptions of the theory. In 3D, the volume associated with each ball should be greater than the size of the ball. In the case of 1D, a distribution of possible arrangements of hard-spheres corresponds to the distribution of ideal gas particles by removing the volume occupied by the size of the ball (see Fig. 3.7). Such a mapping is exact in 1D, which implies the exponential

distribution in terms of the free volume. To see this, consider a system of volume V (or a system of linear size L in 1D) and a smaller part of this volume, V^*. The probability for one particle to be outside the volume V^* is $P(1) = (1 - V^*/V)$. For N independent particles, we obtain $P(N) = (1 - V^*/V)^N$. We set $V^*/V = 1/x$ and the density $\rho = N/V$. Then $P(N) = (1 - 1/x)^{\rho V} = (1 - 1/x)^{\rho x V^*}$. In the limit $x \to \infty$, we obtain a Boltzmann-like distribution: $e^{-\rho V^*}$.

While the above derivation is an exact 1D solution, the extension to higher dimensions is an approximation, since there exists additional geometrical constraints. Even if there is a void with enough volume to be occupied by a particle (that is the volume of the void is larger or equal than the size of the particle), the constraint imposed by the geometrical shape of the particle (which does not exist in 1D) might prevent the void for being occupied. As the simplest approximation we assume the exponential distribution to be valid in 3D.

Next, we test the exponential forms of the cumulative distributions, as well as their correlations, by computer simulations of packings at the frictionless point. The results are plotted in Fig. 3.8. We first calculate independently $P_{\rm B}(c)$ and $P_{\rm C}(c)$. For a given ball, we choose a direction $\hat{s}$ at random and then find the ball [situated at (r, θ)] with the minimum value of $r/\cos\theta$. More precisely, we find $\min_{\hat{s}\cdot\hat{r}_{ij}>0} \frac{r_{ij}}{2\hat{s}\cdot\hat{r}_{ij}}$, for a fixed direction $\hat{s}$. We then collect data for 400 different directions.

For a given direction, we find two minimum values of c independently as c_b and c_c over all particles in the packing. The c_b is only provided by the ball in the background, and c_c is only provided by the ball in contact. From the probability density, we then calculate the cumulative probability to find a ball at position r

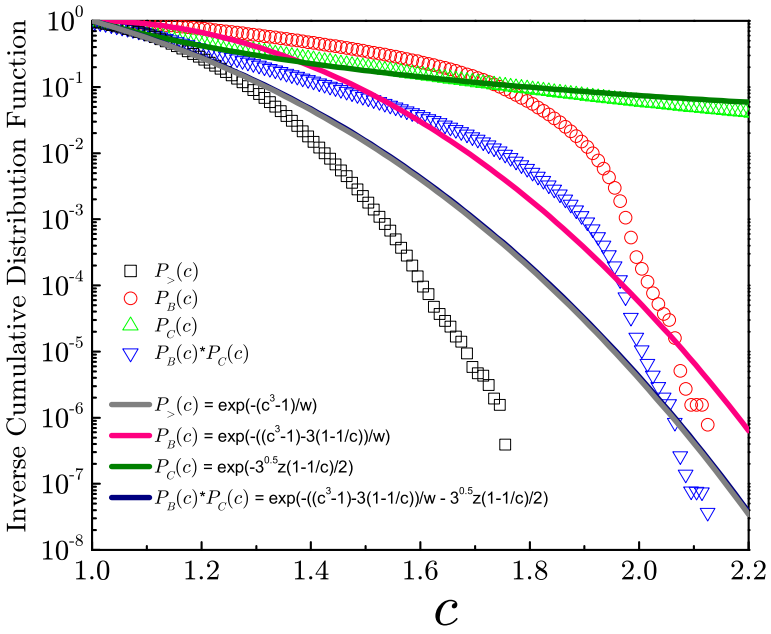

Figure 3.8: Comparison between theory and simulations for the inverse cumulative distributions, $P_{\rm B}(c), P_{\rm C}(c)$, $P_{\rm B}(c) \times P_{\rm C}(c)$ and $P_>(c)$ for a packing at the frictionless point with $z = 6$. Similar results are obtained for frictional packings.

and θ such that $r/\cos\theta > c$. That is, we calculate the cumulative distribution of c_b and c_c individually, i.e., $P_{\rm B}(c)$ and $P_{\rm C}(c)$.

The purpose of this calculation is, firstly, to test the predictions of the theory Eq. (3.16) and (3.19) for $P_{\rm B}(c)$ and $P_{\rm C}(c)$, and, secondly, to test whether the background distribution is independent of the contact one by comparing $P_{\rm B}(c) \times P_{\rm C}(c)$ with $P_>(c)$. The latter is calculated from the simulations by counting all the balls without differentiating between background and contact balls.

The inverse cumulative distributions in Fig. 3.8 show that the theory approximately captures the trend of these functions but deviations exist as well, especially for large c values. The contact term $P_{\rm C}(c)$ is well approximated by the theory, while the background term shows deviations for larger c; for smaller c the theory is not

too far from simulations. We point out that the mesoscopic volume function, w, is extracted from the mean value of $\langle w^s \rangle$ as $w = \langle w^s \rangle = \langle c^3 \rangle - 1$. Indeed, we find that the average $\langle w^s \rangle$ is well reproduced by the theory, and that the deviations from the theoretical probabilities for $w^s > \langle w^s \rangle$ appear not to contribute significantly towards the average volume function. This is seen in the fact that we obtain a good approximation to the volume fraction of the packing even though the full distributions show deviations at larger w^s. For instance, the packing used to obtain the results of Fig. 3.8 has a volume fraction $\phi = 0.64$ as measured from the particle positions. This value agrees with the average $\langle w^s \rangle$ obtained from the prediction of the probability distribution $P_>(c)$. We find $\langle c^3 \rangle = 1.561$, then $\langle w^s \rangle = \langle c^3 \rangle - 1 = 0.561$ and $\phi = 1/\langle c^3 \rangle = 1/(\langle w^s \rangle + 1) = 0.641$ in agreement with the volume fraction of the entire packing obtained from the position of all the balls, 0.64. This shows that the theory approximates well the mean value $\langle w^s \rangle$ (which is needed to obtain accurate estimations of the volume fraction), even though the full distribution presents deviations from the theory. Therefore, the main results of the theory, that is that the Voronoi or quasi-particle volume decreases with the number of contacts, and that the coordination number decreases by increasing friction are not affected by the assumption of the theory.

From Eqs. (3.20) and (3.24) we find the distribution of orientational Voronoi volumes. We reproduce the exponential tail in the Voronoi distribution found in experimental studies of Aste *et al.* [48] and Dauchot *et al.* [49]. We calculate $P(w^s)$ from computer simulations at the frictionless point (details are given in Section 3.2.6). The results are shown in Fig. 3.9 where we see that the theory is able to reproduce the exponential tail in the distribution. However, the distribution

from simulations is not a pure exponential but there are corrections at small w^s. We observe that the average value $\langle w^s \rangle$ is well described by the theory. We find $\langle w^s \rangle = 0.561$, which gives a volume fraction $\phi = 1/(1 + \langle w^s \rangle) = 0.641$, in agreement with the direct measurement of the volume fraction of the packing which is 0.64. Thus, the present theory gives a good approximation to the average Voronoi volume needed for the mesoscopic volume function. The theory underestimates the simulations in the range from $w^s \approx 1.5$ to $w^s \approx 2$ and overestimates in the range from $w^s \approx 2$ to $w^s \approx 4$, providing a good estimation of the average while still showing deviations in the full distribution. In order to capture all the moments of the distribution a more refined theory is needed. Such a theory will include the corrections to the exponential forms of $P_{\rm B}(c)$ and $P_{\rm C}(c)$ and their correlations.

The correlations between the contact and bulk term are quantified by comparing $P_{\rm B}(c) \times P_{\rm C}(c)$ with $P_{>}(c)$ in Fig. 3.8. From the figure we see that below and around the mean $\langle c \rangle$, the full distribution is close to the theoretical result while deviations appear for larger c. Further, a test of the existence of correlations between $P_{\rm B}(c)$ and $P_{\rm C}(c)$ is obtained by calculating the product-moment coefficient of Pearson's correlation as follows.

In the simulation, we pick up a direction $\hat{s}$ randomly, and collect c_b and c_c defined as:

$$c_b = \min_{\hat{s}\cdot\hat{r}_{ij}>0} \frac{r_{ij}}{2\hat{s}\cdot\hat{r}_{ij}}, \quad r_{ij} > 2R, \qquad c_c = \min_{\hat{s}\cdot\hat{r}_{ij}>0} \frac{r_{ij}}{2\hat{s}\cdot\hat{r}_{ij}}, \quad r_{ij} \leq 2R. \tag{3.25}$$

The Pearson's coefficient is:

$$r^2 = \frac{{S_{bc}}^2}{S_{bb}S_{cc}}, \tag{3.26}$$

where $S_{bb} = \Sigma({c_b}^2 - \bar{c}_b^2)$, $S_{cc} = \Sigma({c_c}^2 - \bar{c}_c^2)$, and $S_{cb} = \Sigma(c_b c_c - \bar{c}_b \bar{c}_c)$. We find that the Pearson coefficient $r^2 = 0.0173$ is close to zero, meaning that the correlations between $P_B(c)$ and $P_C(c)$ are weak.

The present numerical results imply that the current assumptions of the theory are reasonable. The conclusions are that while the cumulative distributions present deviations from the theory in their tails, the average value of the Voronoi volumes are well captured by the approximations of the theory, which provides, then, an accurate value for the volume function. While the theory considers the full probability distribution of volumes, the w function is defined as the average of this distribution as indicated in Eqs. (3.13) and (3.21).

More importantly, the present approach indicates a way to improve the theory to provide more accurate results. Our current studies indicate that we might be able to solve exactly the distribution $P_>(c)$ for a fixed z-ensemble by taking into account the contribution to the volume function from the second coordination shell of particles. Due to the fact that the range of Voronoi cell is finite, it is possible, in principle, to work out a description for the finite, but large, number of degrees of freedom for both disordered and ordered packings through computational linear programming. This approach is related to the Hales' proof of the Kepler conjecture [42]. The present theory is a mean-field version in terms of the restricted description of the disordered packings, which allows us to reduce the dimensionality of the original problem in order to write down the analytic form of the volume function in reasonable agreement with the know values of RCP and RLP. The present

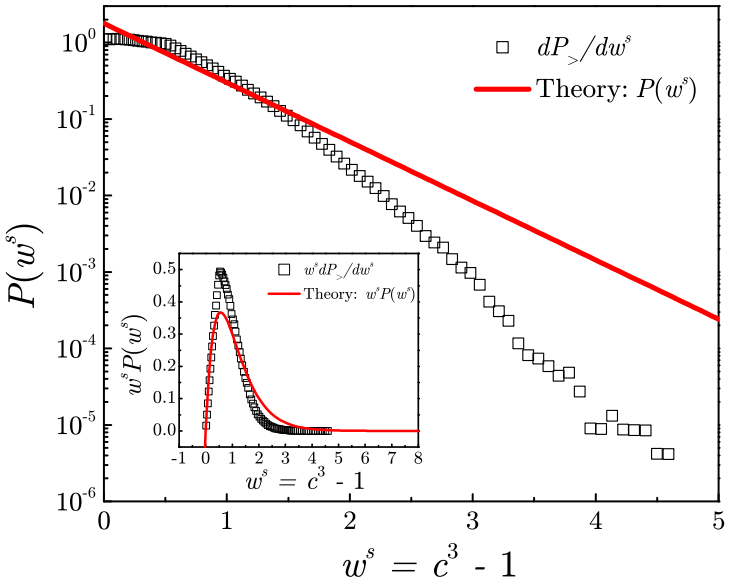

Figure 3.9: PDF of w^s. The black squares are simulation results, and the red solid line is the theoretical prediction. The inset plots $w^s P(w^s)$, the integrations of the black square and red solid line give the same value of $\langle w^s \rangle = \phi^{-1} - 1$ despite the observed deviations.

approximations of the theory are further supported by the agreement between the obtained form of the volume function and the empirical findings of the experiments of [13].

Below we test the formula Eq. (3.24) with the well-known example of the FCC lattice at $z = 12$ to assess the approximations in the current version of the theory. At this limiting number of neighbors the entire class of attainable Voronoi cells have volumes in a narrow range around 0.7 Vg which is significantly larger than the prediction from Eq. (3.24). The current theory is developed under the assumption of isotropic packings. Isotropic packings are explicitly taken into account in the theory when we consider the orientational Voronoi volume $\mathcal{W}_i^s$ (along a direction $\hat{s}$) as a simplification of the full Voronoi volume, $\mathcal{W}_i^{\text{vor}}$. Such a simplification is

equivalent to $\mathcal{W}_i^{\text{vor}}$ at the mean-field level and meaningful for isotropic packings but fails for anisotropic or ordered packings. The extension of the current theory to anisotropic packings, such as the FCC lattice at $z = 12$, can be carried out, but remains outside of the scope of the present work. In this case, the full Voronoi volume Eq. (3.8) needs to be used. In fact, it is possible to describe the finite number of degrees of freedom for ordered packings, which is related to the Hales' proof of the Kepler conjecture [42], through computational linear programming.

3.2.2 Isostatic condition

Here we explain the usual constraint arguments leading to the existence of the minimal mechanical coordination number at the isostatic point [57, 58, 54, 59, 55]. We consider a set of spherical particles interacting via normal and tangential contact forces. These can be the standard Hertz and Mindlin/Coulomb forces of contact mechanics, respectively, see Section 3.2.6. We set N: number of particles, N_n: number of unknown normal forces, N_t: number of unknown tangential forces, E_f: number of force balance equations, E_t: number of torque balance equations, d: dimension, $Z = 2M/N$: average coordination number of the packing, where M is the total number of contacts, $f_1(\mu)$: undetermined function of the friction coefficient μ such that $1 - f_1(\mu)$ is the fraction of spheres that can rotate freely ($f_1(0) = 0$ and $f_1(\infty) = 1$), and $f_2(\mu)$: undetermined function of μ indicating the ratio of contacts satisfying $F_t < \mu F_n$, where F_n, and F_t are the normal and tangential forces respectively at the contact, which satisfies $f_2(0) = 0$ and $f_2(\infty) = 1$.

A packing is isostatic when the number of contact forces equal the number of

force and torque balance equations, i.e.:

$$N_n + N_t = E_f + E_t. \tag{3.27}$$

The average coordination number at the isostatic point is then (see Table 3.1):

$$Z(\mu) = 2d\frac{1 + 1/2(d-1)f_1(\mu)}{1 + (d-1)f_2(\mu)}, \tag{3.28}$$

reducing to the known $Z = 2d$ for frictionless particles and $Z = d+1$ for infinitely rough particles. The relation $Z(\mu)$ is an important assumption of the theory. Figure 3.10 shows $Z(\mu)$ obtained in simulations for different preparation protocols explained in Section 3.2.6. It should be noted that other protocols could give rise to other dependence of Z on μ. However, since the phase diagram is given in terms of Z, the main prediction of Fig. 3.1 would still be valid.

Another way to see the equation $Z(\mu)$ is the following. For finite μ, we have to consider additional Coulomb conditions. The calculation of $Z(\mu)$ becomes a non-linear problem except when $\mu \to 0$ and $\mu \to \infty$. The problem can be understood as an optimization of an outcome based on a set of constraints, i.e., minimizing a Hamiltonian of a system over a convex polyhedron specified by linear and non-negativity constraints. Equation (3.27) can be augmented to indicate the number of extra equations for contacts satisfying the Coulomb condition, which is analogous to the number of redundant constraints in Maxwell constraint counting of rigidity percolation. This suggests that, for a finite value of μ, the original non-linear problem can be mapped to a linear equation problem if we know how many extra equations should be added.

Table 3.1: Number of constraints and variables determining the isostatic condition for different systems.

Friction	N_n	N_t	E_f	E_t
$\mu = 0$	$\frac{1}{2}NZ$	0	dN	0
μ finite	$\frac{1}{2}NZ$	$\frac{1}{2}(d-1)NZf_2(\mu)$	dN	$\frac{1}{2}d(d-1)Nf_1(\mu)$
$\mu = \infty$	$\frac{1}{2}NZ$	$\frac{1}{2}(d-1)NZ$	dN	$\frac{1}{2}d(d-1)N$

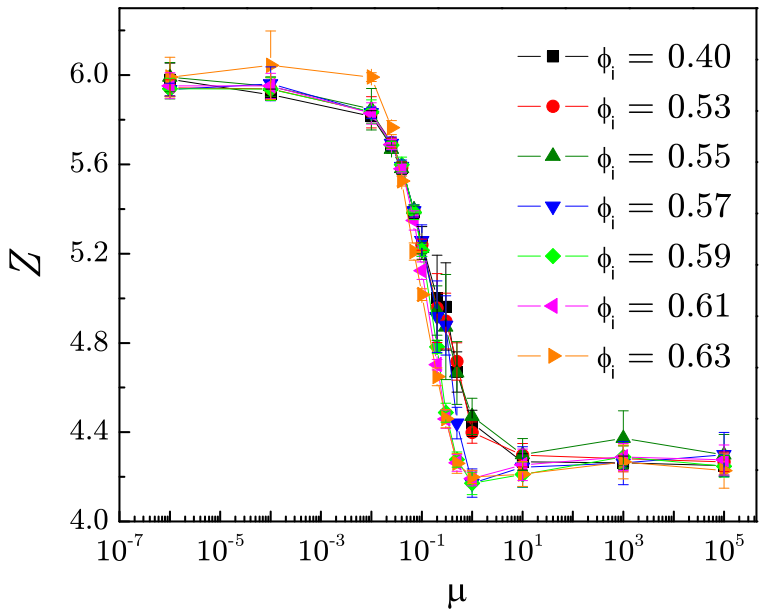

Figure 3.10: Mechanical coordination number versus friction μ obtained in our numerical simulations explained in Section 3.2.6 for different preparation protocols characterized by the initial volume fractions ϕ_i indicated in the figure. The symbols and parameters used in these simulations are the same as in the plot of Fig. 3.4.

3.2.3 Geometrical and mechanical coordination number

The derivation of the volume function in Section 3.2.1 implies nothing about the value of the contact forces; the volume function represents the contribution arising purely from the geometry of the packing. Thus, the coordination number z appearing in Eq. (3.1) is the *geometrical* coordination number related to volume, which is different from the *mechanical* coordination number Z that can be measured through the force contact network relating to the isostatic condition. In general we expect $Z \leq z$, since some geometrical contacts may carry no force. To show this, imagine a packing of infinitely rough ($\mu \to \infty$) spheres with volume fraction close to 0.64. There must be $z = 6$ nearest neighbors around each particle on the average. However, the mechanical balance law requires only $Z = 4$ contacts per particle on average, implying that 2 contacts have zero force and do not contribute to the contact force network.

Such a situation is possible: starting with the contact network of an isostatic packing of frictionless spheres having $z = 6$ and all contacts carrying forces (then $Z = 6$ also), we simply allow the existence of tangential forces between the particles and solve the force and torque balance equations again for this modified system of infinitely rough spheres. Such a solution is guaranteed to exist due to the isostatic condition. The resulting packing is mechanically stable and is obtained by setting to zero the forces of two contacts per ball, on average, to satisfy the new force and torque balance condition for the additional tangential force at the contacts. Despite mechanical equilibrium, giving $Z = 4$, there are still $z = 6$ geometrical contacts contributing to the volume function. Therefore, we identify two types of coordination number: the geometrical coordination number, z, contributing to

the volume function and the mechanical coordination number, Z, measuring the contacts that carry forces only.

These ideas are corroborated by numerical simulations in Section 3.2.6 and explained in Section 3.2.3, below. The packings along the vertical RCP line found in the simulations (see Fig. 3.4 in the main text) have approximately the same geometrical coordination number, $z \approx 6$. However, they differ in mechanical coordination number, going from the frictionless point $Z = 6$ to $Z \approx 4$ as the friction coefficient is increased (see Section 3.2.6).

Bounds of the geometrical coordination number, z.

We have proposed in the main text that the bounds of the geometrical coordination number are $Z \leq z \leq 6$ imposed by the isostatic condition. Below we test these bounds with computer simulations (for technical details of the computer simulations we refer to Section 3.2.6). The interpretation of z considers it as a coarse-grained average associated with "quasiparticles" with free volume W. The reason to use a coarse grained measure to define the coordination number is in the quasiparticle character of the theory. The calculation of the W function implies a coarse graining over a distance which is found to be of the order of two beads diameters; below we find numerically that the 'quasiparticles" size is of the order of two particle diameters. Once z is averaged over this range, we find that z is ranging approximately between $(Z, 6)$. Thus the theory considers the mesoscopic fluctuations associated with each quasi-particle. In the limiting case of no mesoscopic fluctuations, when $X = 0$ along the RCP line, we find a very narrow distribution at $z = 6$ for any value of Z and μ, after averaging z over a mesoscopic region of

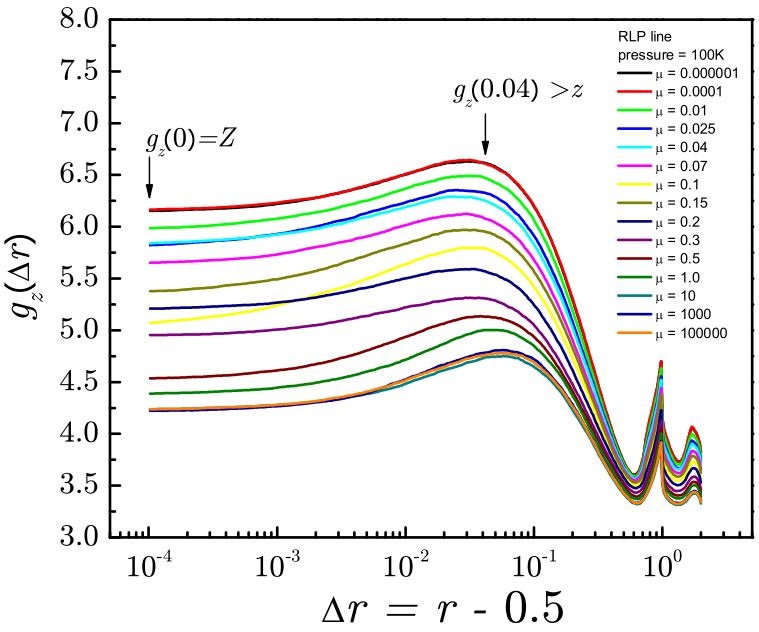

Figure 3.11: $g_z(\Delta r)$ of packings with various friction coefficient μ along RLP line.

two particle diameters. The distribution is even narrower when z is coarse-grained over a region of four particle diameters.

Thus, the bounds $(Z, 6)$ are shown to hold under reasonable accuracy; well approximated by the assumption in the theory. The X-ray tomography experiments of Aste [48] (Fig. 6a) reveal the trend predicted by Eq. (3.1) between the inverse of the Voronoi volume and the average number of neighbors of a set of Voronoi cells with similar volumes. However, it is evident from the figure that such average number of neighbors is spanning a range of values between ~ 4 and ~ 10. The reason why the Aste's group found wider range of z is possibly due to the fact they did not consider such a range of coarse-graining.

In order to identify the geometrical coordination number, z, and the mechanical coordination number, Z, we define a modified radial distribution function $g_z(r)$ as:

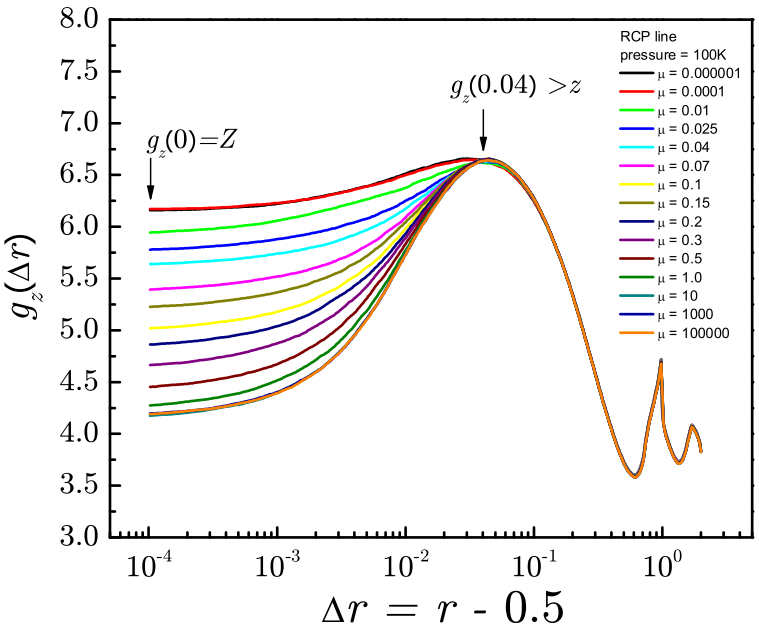

Figure 3.12: $g_z(\Delta r)$ of packings with various friction coefficient μ along RCP line.

$$g_z(r) = \frac{1}{N}\frac{R^2}{r^2}\sum_{i}^{N}\sum_{j\neq i}^{N}\Theta(\frac{r_{ij}}{r-R})\Theta(\frac{r+R}{r_{ij}}), \quad r > R \tag{3.29}$$

where R is the radius of particle, N is the number of particles, r_{ij} is the distance of two particle's centers, $r_{ij} = |\vec{r}_i - \vec{r}_j|$, and Θ is the Heaviside step function. $g_z(r)$ describes the average value of the number of grains in contact with a virtual particle of radius r, and the factor of R^2/r^2 is the ratio of a real sphere's area and the virtual one's. Figures 3.11 and 3.12 plot the $g_z(\Delta r)$ of packings with various friction coefficient μ on the isostatic plane along the RLP and RCP lines respectively, where we define $\Delta r = \frac{r-R}{2R}$ (noticed that in the figures, we set $2R = 1$ for simplicity). Following the definition of Eq. (3.29), g_z with $\Delta r = 0$ should be directly equal to the mechanical coordination number, Z, and should range from 4 to 6 along both RLP and RCP lines which is confirmed by our numerical

simulations in Fig. 3.11 for the RLP line and Fig. 3.12 for the RCP line.

Furthermore, as shown in the figures, we find that $g_z(\Delta r)$ along the RCP line, increases slightly as Δr increases, and finally reach the same value of g_z at $\Delta r = 0.04$ as shown in Fig. 3.12, indicating that all RCP states have approximately the same geometrical coordination number, $z \sim 6$. This is in agreement with the theoretical bounds. We notice that $g_z(\Delta r = 0.04) = 6.65 > 6$, which results from the increasing of the coordination number at the critical point as the local volume fraction ϕ increases slightly as $Z - Z_c \sim (\phi - \phi_c)^\beta$.

Furthermore, we study the coarse-grained coordination number $\langle z \rangle_l$ as defined as,

$$\langle z \rangle_l = \frac{1}{N_l} \frac{R^2}{r^2} \sum_i^{N_l} \sum_{j \neq i}^{N_l} \Theta(\frac{r_{ij}}{r - R}) \Theta(\frac{r + R}{r_{ij}}), \quad r > R \tag{3.30}$$

where N_l is the number of the particles inside a coarse-grained spherical range with a radius of l. Fig. 3.13 and Fig. 3.14 plot the PDF of $\langle z \rangle_l$ for all the packings along the RLP and RCP lines respectively. The distributions show a Gaussian shape, and the average value gives the value of $g_z(r)$, i.e.,

$$\overline{\langle z \rangle_l} = g_z(r). \tag{3.31}$$

We find that all the $P(\langle z \rangle_l)$ along RCP line coincide at $\Delta r = 0.04$ as shown in Fig. 3.14b and 3.14c, demonstrating that all the states have approximately the same average value (as it should be since the RCP line is at $X = 0$), but also the distribution of the geometrical coordination number. The distribution gets narrower as the coarse-graining parameter l increase from $l = 2$ to $l = 4$ as shown

in Fig. 3.14c. This demonstrate that the bounds proposed by the theory are satisfied for the RCP line.

Along the RLP line, the situation is analogous. Since this line corresponds to $X \to \infty$ we should expect different average z as we move along the line varying the friction coefficient. This is clearly demonstrated in Fig. 3.13b which should be compared with the analogous Fig. 3.14b for the RCP line. More importantly, we find that the bounds of $\langle z \rangle_l$ are well approximated between the bounds given by the isostatic condition $(4, 6)$ in agreement with the assumptions of the theory. The slight shift towards higher coordinations observed in Fig. 3.13b is due to the small increment in volume fraction from the critical point of jamming, as discussed above. Overall, we conclude that the bounds assumed by the theory are a good approximation.

3.2.4 Partition Function

According to the statistical mechanics of jammed matter proposed by Edwards [46], the volume partition function $\mathcal{Q}$ is defined as:

$$\mathcal{Q} = \int g(W) e^{-W/X} \Theta_W dW, \tag{3.32}$$

where W is the free volume function, X is the compactivity measured in units of volume, $g(W)$ is the density of states for a given volume W, and Θ_W imposes the condition of jamming.

Since W is directly related to the geometrical coordination number z through

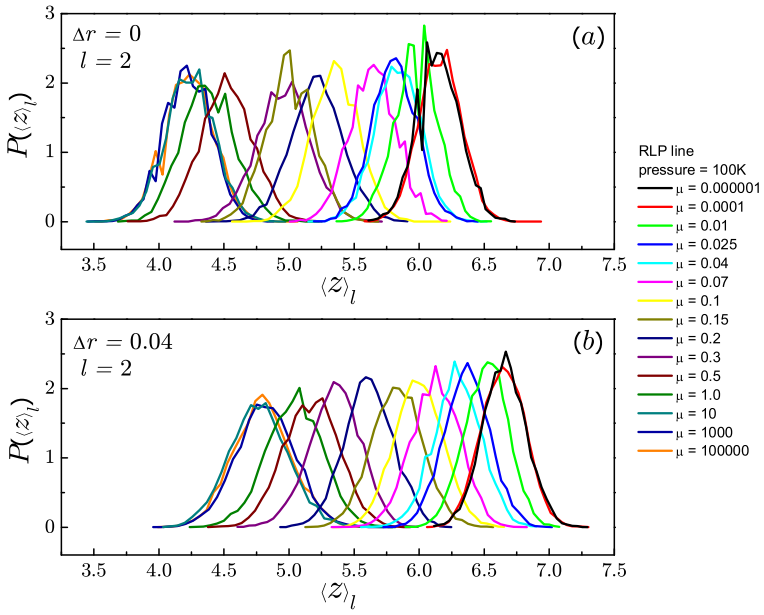

Figure 3.13: PDF of the coarse-grained coordination number $\langle z \rangle_l$ for packings with various friction coefficient μ along the RLP line. (a) $\Delta r = 0$ and $l = 2$; (b) $\Delta r = 0.04$ and $l = 2$.

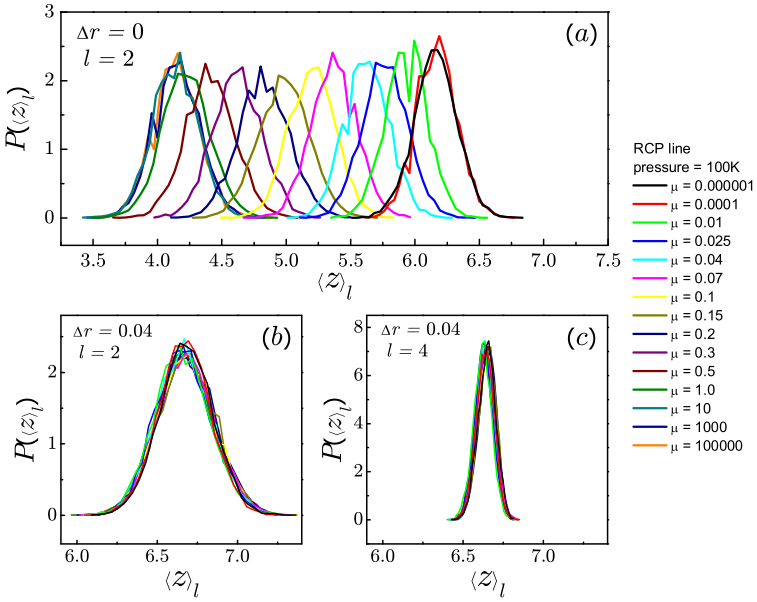

Figure 3.14: PDF of the coarse-grained coordination number $\langle z \rangle_l$ for packings with various friction coefficient μ along the RCP line. (a) $\Delta r = 0$ and $l = 2$; (b) $\Delta r = 0.04$ and $l = 2$; (c) $\Delta r = 0.04$ and $l = 4$.

Eq. (3.6), $g(W)$ is computed by changing variables,

$$g(W) = \int P(W|z)g(z)dz, \tag{3.33}$$

where $P(W|z)$ is the conditional probability of a free volume W for a given z, and $g(z)$ is the density of states for a given z.

Here, z is the geometrical coordination number related with volume, different from the mechanical one, Z. From the arguments explained in Section 3.2.3, z must be larger than or equal than the mechanical coordination number Z and bounded by the maximum coordination number for a random packing, which is $2d = 6$. That is,

$$g(W) = \int_Z^6 P(W|z)g(z)dz. \tag{3.34}$$

The density of states $g(z)$ can be understood in three step. First, we consider that the packing of hard spheres is in a jammed configuration in which there can be no collective motion of any contacting subset of particles that leads to unjamming. This definition corresponds to the collectively jammed category proposed by Torquato and co-workers [60]. It is a sensible definition of jammed configurations since it goes beyond the merely locally jammed configuration of packings that are unstable to the motion of a single particle. While the degrees of freedom are continuous, the fact that the packing is collectively jammed implies that the jammed configurations in the volume space are not continuous. Otherwise there would be a continuous transformation in the position space that would unjam the system contradicting the fact that the packing is collectively jammed. Thus, we consider that the configuration space of jammed matter is discrete since we cannot change

one configuration to another in a continuous way.

Second, we call the dimension per particle of the configuration space as $\mathcal{D}$ and consider that the distance between two jammed configurations is not broadly distributed (meaning that the average distance is well-defined). We call the mean distance between configurations in the volume space as h_z, and therefore the number of configuration is proportional to $1/(h_z)^{\mathcal{D}}$.

Third, we add z constraints per particle due to the fact that the particle is jammed by z contacts. Thus, there are Nz position constrains ($|\vec{x}_i - \vec{x}_j| = 2R$, where $\vec{x}_i$ is the position of the particle i) for a jammed state of hard spheres as compared to the unjammed "gas" state. Therefore, the number of degrees of freedom is reduced to $\mathcal{D} - z$, and the number of configurations is then $1/(h_z)^{\mathcal{D}-z}$. Since the term $1/(h_z)^{\mathcal{D}}$ is a constant, it will not influence the partition function. Therefore, we obtain $g(z) = (h_z)^z$.

The situation is analogous to the discreteness of the configuration space imposed by the Heisenberg principle in quantum mechanics. While the degrees of freedom $\{p_i, q_i\}$ are continuous, the uncertainty principle imposes the discreteness $\Delta p \Delta q \sim h$. In equilibrium statistical mechanics the dimension per particle of the configuration space is d, and a density of states is obtained as $1/h^d$.

The conditional probability $P(W|z)$ depends on the W function, $W = \frac{2\sqrt{3}}{z} V_g$. The average is taken over a certain mesoscopic length scale since the volume of a particle depends on the positions of the particles surrounding it. Practically, such length scale is approximately of several particle diameters. W is a coarse-grained

volume and independent of the microscopic partition of the particles, implying:

$$P(W|z) = \delta(W - \kappa/z). \tag{3.35}$$

Substituting Eq. (3.35) and Eq. (3.34) into Eq. (3.32), we find the isostatic partition function used in Eq. (3.3) in the main text (we set $V_g = 1$ for simplicity, i.e. we measure the compactivity in units of V_g):

$$\mathcal{Q}_{\rm iso}(X, Z) = \int_Z^6 (h_z)^z \exp\left(-\frac{2\sqrt{3}}{zX}\right) dz. \tag{3.36}$$

3.2.5 Calculation of the equations of state.

Here we provide details of the calculations leading to the equations of state (3.4) and (3.5). From the partition function (3.36), we calculate the average volume fraction $\phi^{-1} = W/V_g + 1 = 2\sqrt{3}/z + 1 = (2\sqrt{3} + z)/z$ as:

$$\phi(X, Z) = \frac{1}{\mathcal{Q}_{\rm iso}(X, Z)} \int_Z^6 \frac{z}{z + 2\sqrt{3}} \exp\left(-\frac{2\sqrt{3}}{zX} + z \ln h_z\right) dz, \tag{3.37}$$

where $(h_z)^z = \exp[z \ln h_z]$, note that $\ln h_z < 0$, since $h_z \ll 1$. In the limit of $X \to 0$, only the minimum volume or ground state at $z = 6$ contributes to the partition function. Then Eq. (3.37) gives Eq. (3.4):

$$\phi_{\rm RCP} = \phi(X = 0, Z) = \frac{6}{6 + 2\sqrt{3}} \approx 0.634, \quad Z(\mu) \in [4, 6], \tag{3.38}$$

plotted in Fig. 3.1 as the RCP line.

When $X \to \infty$, $\exp(-2\sqrt{3}/(zX)) \to 1$, and the average in (3.37) is over all

states with equal probability:

$$\phi_{\mathrm{RLP}}(Z) = \phi(X \to \infty, Z) = \frac{1}{\mathcal{Q}_{\mathrm{iso}}(\infty, Z)} \int_Z^6 \frac{z}{z + 2\sqrt{3}} \exp\left(z \ln h_z\right) dz. \tag{3.39}$$

The constant h_z determines the minimum volume in the phase space and therefore $h_z \ll 1$. Then the leading contribution to Eq. (3.39) is from the highest volume at $z = Z$ and therefore:

$$\phi_{\mathrm{RLP}}(Z) \approx \frac{Z}{Z + 2\sqrt{3}}, \quad Z(\mu) \in [4, 6], \tag{3.40}$$

plotted in Fig. 3.1 as the RLP line. For finite X, Eq. (3.37) can be solved numerically. For each X, the function $\phi(X, Z)$ can be obtained and is plotted as each isocompactivity color line in Fig. 3.1. Finally, the entropy can also be calculated as

$$S(X, Z) = \langle W \rangle / X + \ln \mathcal{Q}_{\mathrm{iso}}(X, Z) \tag{3.41}$$

This equation is obtained in analogy with equilibrium statistical mechanics and it is analogous to the definition of free energy: $F = E - TS$ where $F = -T \ln \mathcal{Q}$ is the free energy, T is the temperature and E the average energy. We replace $T \to X$, $E \to \langle W \rangle$. Therefore, $F = E - TS$ or $S = (E - F)/T = E/T + \ln \mathcal{Q}$ is now $S(X, Z) = \langle W \rangle / X + \ln \mathcal{Q}_{\mathrm{iso}}(X, Z)$, which is plotted as the equation of state in Fig. 3.3. For the calculation of S we consider $g(z) = {h_z}^{z-2d}$ since for $z = 2d$ there is only one mesoscopic state or $g(z) = e^{-\frac{z-2d}{z_c}}$ with $z_c = \frac{1}{\ln(h_z^{-1})} = 0.01$ as

used in Fig. 3.3 and 3.4. This correction is irrelevant for average quantities like $\phi(X, Z)$ but important for the entropy.

3.2.6 Simulations

Molecular dynamics simulations of grains

We prepare static packings of spherical grains interacting via elastic forces and Coulomb friction. The system size ranges from $N = 1,024$ to $N = 10,000$ particles. In the microscopic model, two spherical grains in contact at positions $\vec{x}_1$ and $\vec{x}_2$ and with radius R interact with a Hertz normal repulsive force

$$F_n = \frac{2}{3}\, k_n R^{1/2} \delta^{3/2}, \tag{3.42}$$

and an incremental Mindlin tangential force

$$\Delta F_t = k_t (R\delta)^{1/2} \Delta s, \tag{3.43}$$

(see [54] for more details). Here the normal overlap is $\delta = (1/2)[2R - |\vec{x}_1 - \vec{x}_2|] > 0$. The normal force acts only in compression, $F_n = 0$ when $\delta < 0$. The variable s is defined such that the relative shear displacement between the two grain centers is $2s$. The prefactors $k_n = 4G/(1-\nu)$ and $k_t = 8G/(2-\nu)$ are defined in terms of the shear modulus G and the Poisson's ratio ν of the material from which the grains are made. Typically, $G = 29$ GPa and $\nu = 0.2$ for spherical glass beads and we use $R = 5 \times 10^{-3}$ m and the density of the particles, $\rho = 2 \times 10^3$ kg/m^3. Viscous dissipative forces are added at the global level affecting the total velocity of each particle through a term $-\gamma \dot{\vec{x}}$ in the equation of motion, where γ is the damping

coefficient related to the viscosity of the medium $\eta = \gamma/(6\pi R)$. Sliding friction is also considered:

$$F_t \leq \mu F_n. \tag{3.44}$$

That is, when F_t exceeds the Coulomb threshold, μF_n, the grains slide and $F_t = \mu F_n$, where μ is the static friction coefficient between the spheres. We measure the time in units of $t_0 = R\sqrt{\rho/G}$, the compression rate in units of $\Gamma_0 = 5.9t_0^{-1}$ and the viscosity in units of $\eta_0 = 8.2R^2\rho/t_0$.

Preparation protocols: Packings at the jamming transition

The preparation protocol consists of first preparing a gas of non-interacting particles at an initial volume fraction ϕ_i in a periodically repeated cubic box. The particles do not interact and therefore the stress in the system is $\sigma = 0$ and $Z = 0$. To achieve any particular volume fraction in this initial stage, we apply an isotropic compression without friction. The final results do not depend on the details of this preparation since the system is still below the jamming condition, retaining the characteristics of a fluid. After obtaining this state with initial volume fraction ϕ_i, a compression is applied with a compression rate Γ until a given volume fraction ϕ_1. Then the compression is stopped and the system is allowed to relax to mechanical equilibrium by following Newton's equations for translations and rotations without further compression.

This protocol can generate packings with different volume fractions. Simulations reveal that there is a critical volume fraction at the jamming transition ϕ_c, below which a jammed packing with nonzero pressure can not be obtained. After the compression with Γ, two things can occur:

(a) The system jams: If the system is above the jamming point $\phi_1 > \phi_c$, then the stress will decrease and ultimately stabilize to a finite nonzero value, meaning that the pressure of the system remains unchanged (usually $\Delta\sigma < 10^{-3}$ Pa) over a large period of time (usually $\sim 10^7$ MD steps). The coordination number usually has a first initial decrease, but if the system is jammed it will also stabilize at a constant value above the isostatic minimal number.

(b) The system is not jammed: here the stress and the coordination number will relax to zero. If the packing has $\phi_1 > \phi_c$, it stabilizes at a non-zero pressure above the jamming transition, but the pressure decreases very fast to zero (the system is not jammed) if $\phi_2 < \phi_c$, even though ϕ_1 and ϕ_2 may differ only by 2×10^{-4}.

In order to identify the exact volume fraction of the jamming transition, we apply a split algorithm to find ϕ_c as follows [61]. A search procedure consisting of several cycles is applied such that in each cycle we fix the lower and upper boundaries of ϕ_c. The difference between the boundaries gets smaller as the cycles proceed, meaning that ϕ_c is fixed with higher and higher precision. We start from the packing of high volume fraction $\phi_1 > \phi_c$ and generate a series of packings with step-decreasing volume fractions until the first packing with zero pressure is observed, which has a volume fraction $\phi = \phi_1 - \Delta\phi$. Thus, ϕ_c is bounded between $\phi_1 - \Delta\phi$ and ϕ_1. Then we test $\phi = \phi_1 - \Delta\phi/2$. If $\phi = \phi_1 - \Delta\phi/2$ is stable, ϕ_c is between $\phi_1 - \Delta\phi$ and $\phi_1 - \Delta\phi/2$. If $\phi = \phi_1 - \Delta\phi/2$ is unstable, ϕ_c is between $\phi_1 - \Delta\phi/2$ and ϕ_1. Therefore, in this cycle, we reduce the region where ϕ_c possibly lies in from $\Delta\phi$ to $\Delta\phi/2$. If we carry out this cycle for n times, we improve the precision to $\Delta\phi_n = \Delta\phi/2^n$. In our simulations cycling ceases when $\Delta\phi_n$ gets

below 2×10^{-4} and $n = 12$. A similar algorithm was employed in [61] to study the approach to the jamming transition by preparing packings at a finite pressure. In the present work we are interested in jammed packings at vanishing pressure, right at the jamming transition in the isostatic plane defined for all friction coefficients.

This algorithm obtains packings at the critical density of the jamming transition with high precision, $\phi_c \pm 2 \times 10^{-4}$ (notice that in the main text we denote $\phi_c = \phi$ for simplicity). In Fig. 3.4 we simulate jammed packings by starting with configurations with ϕ_i and performing the split algorithm to find ϕ_c. We repeat this procedure 10 times with different random initial configurations to get a better average of ϕ_c. Each data point in Fig. 3.4 corresponds to a single set of $(\phi_i, \Gamma, \eta, \mu)$ and is averaged over these 10 realizations. We consider $0.40 \leq \phi_i \leq 0.63$, $10^{-7} \leq \Gamma \leq 10^{-3}$, $10^{-4} \leq \eta \leq 10^{-3}$, and $0 \leq \mu \leq \infty$. The error of ϕ_c obtained over the 10 realizations as shown in Fig. 3.4 is usually 5×10^{-4}, larger than the precision of the split algorithm (2×10^{-4}).

It is important to determine whether the packings are jammed in the sense that they are not only mechanically stable but also they are stable under perturbations. Our numerical protocols assure that the system is at least locally jammed since each particle is in mechanical equilibrium [60]. To test if the system is collectively jammed is more involved. For frictionless systems, where tangential forces are removed, we use the Hertz energy $U_{\text{hertz}} = \frac{4}{15}\ k_n R^{1/2} \delta^{5/2}$ to test whether the Hessian of the jammed configurations is positive [55]. We find that the frictionless configurations have positive Hessian indicating that they are collectively jammed. However, this method is not useful when considering frictional systems. The energy of deformation depends on the path taken to deform the system and cannot be

defined uniquely. In this case, a numerical test of the stability of the packings applies a small random velocity to each jammed particle. We find that the packings are stable to small perturbations consisting of external forces of the order of 0.1 times the value of the average force, indicating that the packings may be collectively jammed.

To test for more strict jammed conditions involves studying the stability under boundary deformations. We have tested that our packings are stable under the most common strain deformations to isotropic packings by performing a uniaxial compression test, a simple shear and a pure shear test.

For instance, a simple shear test implies a strain deformation $\Delta\epsilon_{12} = \Delta\epsilon_{21} \neq 0$, while the rest of the strain components ϵ_{ij} remain constant. A pure shear test is done with $\Delta\epsilon_{11} = -\Delta\epsilon_{22} \neq 0$ and a uniaxial compression test along the 1-direction is performed by keeping the strain constant in $\Delta\epsilon_{22} = \Delta\epsilon_{33} = 0$, and $\Delta\epsilon_{11} \neq 0$. Here, the strain ϵ_{ij}, is determined from the imposed dimensions of the unit cell. For example, $\epsilon_{11} = \Delta L/L_0$ where ΔL is the infinitesimal change in the 11 direction and L_0 is the size of the reference state.

In all cases the packings are stable under strain perturbations. A full investigation of the elasticity of the jamming phase diagram is left for future studies. It suffices to state that the numerically found states can be considered to be mechanically stable jammed states.

Results

Knowledge of the existence of the packings in the phase diagram opens such predictions to numerical and experimental investigation. Next, we test the theoretical

predictions and show how to dynamically generate all the packings in the phase space of configurations through different preparation protocols. In particular we provide a scheme to reproduce the RCP and RLP-lines amenable to experimental tests. We parameterize the preparation protocol by the initial volume fraction ϕ_i, the compression rate Γ, and the dissipative properties of the medium where the particles are disperse, the viscosity η. The system is defined by the friction coefficient μ.

In Fig. 3.4 we plot the final state ϕ against the mechanical coordination number of the packings Z for different preparation protocols parameterized by $(\phi_i, \Gamma, \eta, \mu)$.

The main plot in Fig. 3.4 explores the dependence of the packings (ϕ, Z) on the initial state ϕ_i. We plot our results for a fixed quench rate $\Gamma = 10^{-7}$ and damping coefficient $\eta = 10^{-3}$ (except for the last orange curve on the right with $\eta = 10^{-4}$) and for different initial states ranging from left to right (see Fig. 3.4 for details) $\phi_i = 0.40$ (blacks quare), 0.53 (red bullet), 0.55 (violet triangle), 0.57 (blue triangle down), 0.59 (green lozenge), 0.61 (pink triangle left) and 0.63 (orange triangle right). Each data point corresponds to a prepared system at a given friction from $\mu = 0$ at $Z \approx 6$ to $\mu \to \infty$ at $Z \approx 4$.

We find that the packings prepared from the larger initial densities ϕ_i closely reproduce the RCP line of zero compactivity at ϕ_{RCP}. Therefore RCP exists not only at the frictionless J-point at $Z = 6$ but extend along the vertical line until $Z \approx 4$. This corroborates one of the predictions of the theory that RCP states can be found for any value of friction coefficient, not just for frictionless packings. We conclude that RCP is not confined to a single point in the phase diagram but corresponds to the many states along the RCP line.

We find that the packings along the RCP-line have equal geometrical coordination number $z \approx 6$ but differ in their mechanical one from $Z = 6$ to $Z \approx 4$, in agreement with theory. These states are then identified with the ground state of jammed matter as depicted in the volume landscape picture of Fig. 3.2a.

In the limit of small densities for the initial state (see curves for $\phi_i = 0.40, 0.53, 0.55$ in the phase space Fig. 3.4), we reproduce approximately the predictions of the RLP-line. These packings follow the theoretical prediction for infinite compactivity except for small (less than 5%) deviations in the coordination number for packings close to the lower value of $Z = 4$. We find the lowest possible volume fraction at $\phi_{\rm RLP}^{\rm min} = 0.539 \pm 0.003$, close to the theoretical prediction, $\phi_{\rm RLP}^{\rm min} = 0.536$, which approximately agrees with the lowest stable volume fraction ever reported experimentally by Onoda and Liniger, $\phi_{\rm RLP}^{\rm min} = 0.550 \pm 0.006$ for monodisperse hard spheres [44].

Packings with the lowest Z correspond to infinitely rough spheres. The deviation of coordination number between theory and simulation (specially at low volume fraction) could be from the system not achieving an isostatic state at infinite friction. In general, we find that while there are many states along the RLP line, the barriers of these states decrease as the coordination number decreases towards $Z = 4$, i.e. when the friction increases. Thus, the states at the lower left part of the phase diagram are the most difficult to equilibrate.

Besides the states delimiting the phase space, we generate other packings with intermediate values of $\phi_i = 0.57, 0.59, 0.61$ as shown in Fig. 3.4. Interestingly, we find that these states (all obtained for fixed $\Gamma = 10^{-7}$ and $\eta = 10^{-3}$) closely follow the predicted lines of isocompactivity as indicated in the figure. We find that the

simulations from $\phi_i = 0.57, 0.59, 0.61$ correspond to compactivities $X = 1.62, 1.38,$ and 1.16, respectively (measured in units of $10^{-3}V_g$). The constant h_z weakly affects the finite compactivity states. We find that $h_z = 0.01$ provides the best fit to the data for finite isocompactivity lines in Fig. 3.4. Other values of h_z produce approximately the same phase diagram boundaries (i.e., the RLP and RCP lines, as long as $h_z \ll 1$) but with different isocompactivity lines within.

At this point we do not have a theoretical explanation for why packings with the same initial state ϕ_i have the same compactivity. We may conjecture that ϕ_i determines a type of disorder quenched in the initial configuration that leads to systems with the same compactivity but different volume fractions and coordination numbers, evidenced by our results. We can use this empirical result to control the compactivity of the packing, at least for this particular protocol. Laboratory measurements of compactivity usually involve indirect measures through fluctuation-dissipation relations between fluctuations and response functions [1, 47, 64]. Our results can be used to, at a minimum, define packings with equal compactivity. The empirical identification of X with ϕ_i promotes the possibility of controlling X within this particular protocol.

We also test the dependence on the state of the packings with the compression rate Γ and viscosity η. Both parameters should have similar effects since they slow down the dynamics of the grains. In general, we reproduce the RLP line for slow quenches or for large viscosities as seen in the inset of Fig. 3.4. In this case, the grains are allowed to slide and develop large transversal displacements and Mindlin forces with the concomitant low ϕ and large compactivity. Therefore we find a predominance of the Mindlin forces over the normal Herztian forces as a

characteristic of the lower volume fractions of RLP, having large compactivity in the packing. When the compression rate is increased or the damping is reduced we find packings with higher volume fractions as indicated in the inset of Fig. 3.4.

Chapter 4

Particle Dynamics and Effective Temperature of Jammed Granular Matter In a Slowly Sheared 3D Couette Cell

In this chapter, we report experimental measurements of particle dynamics on slowly sheared granular matter in a three-dimensional (3D) Couette cell. A closely-packed ensemble of transparent spherical beads is confined by an external pressure and filled with fluid to match both the density and refractive index of the beads. This allows us to track tracer particles embedded in the system and obtain three-dimensional trajectories, $(r(t), \theta(t), z(t))$, as a function of time. We study the PDF of the vertical and radial displacements, finding Gaussian and exponential distributions, respectively. For slow shear rates, the mean-square fluctuations in

all three directions are found to be dependent only on the angular displacement of the Couette cell, $\Delta\theta_e$, $\langle\Delta z^2\rangle \sim \Delta\theta_e$, $\langle\Delta r^2\rangle \sim \Delta{\theta_e}^{\alpha}$, $\langle\Delta\theta^2\rangle \sim \Delta{\theta_e}^{\beta}$, where α and β are constants. With $\Delta\theta_e$ proportional to the time between measurements, the values of the constants, α and β, are found to be sub-diffusive and super-diffusive, respectively. The linear relation between $\langle\Delta z^2\rangle$ and angular displacement implies a diffusive process, from which we can calculate an "effective temperature", T_{eff}, in the vertical direction, through a Fluctuation-Dissipation relation. It is of interest to determine whether these systems can be described by analogous equilibrium statistical mechanics concepts such as "effective temperature" and "compactivity". By studying the dynamics of tracer particles, we find the effective temperature defined by the Stokes-Einstein relation to be independent of the tracer particle characteristic features, such as density and size, and dependent only on the packing density of the system. For slow shear rate, both the diffusivity and mobility of tracer particles are proportional to the shear rate, giving rise to a constant effective temperature, characteristic of the jammed system. We finally discuss the significance of the existence of T_{eff} for a statistical mechanics formulation of granular matter.

4.1 Introduction

Fluctuation-Dissipation (FD) relations are commonly used in equilibrium systems, derived from the notion that small perturbations and Brownian fluctuations produce the same response in a given system [65]. Mobility, the constant of proportionality between a particles drift speed and a constant external force, is extracted

from velocity statistics of particles in a given system. Diffusivity, calculated from fluctuation displacements of particles in a system over time, represent the Brownian motion. The temperature of a system in thermodynamic equilibrium can be extracted from a FD relation, defined as the ratio of diffusivity and mobility, as is commonly used in the Einstein relation. In equilibrium this temperature is taken to be the bath temperature.

As studies in granular matter have grown more important within the environmental and industrial fields, the need to establish a scientific framework that accurately predicts granular system responses on the continuum level, beyond merely geometrical features, has also escalated. Granular matter, when condensed to sufficiently high volume fractions, undergoes a 'jamming' transition to the jammed state. The jammed state is defined as the condition when a many-body system is blocked in a configuration far from equilibrium, such that relaxation cannot occur within a measurable time-scale. For granular matter, the jammed state indicates a transition between a solid-like behavior, and a liquid-like behavior. At high volume fractions, the physical size of the constituent grains inhibits particle motion, thereby rendering the system out of equilibrium, and the granular system behaves more like a solid. Thermal motion does not govern the exploration of states in jammed granular matter.

Theories proposed by Edwards and collaborators [46] propose a statistical mechanics for granular matter based on jamming the constituent grains at a fixed total volume such that all microscopic jammed states are equally probable and exhibit ergodicity. The exploration of reversible jammed states is achieved via an external perturbation such as tapping or shear, not Brownian motion as in ther-

mal systems. There is an important difference between reversible jammed states, and states that are only mechanically stable within certain limits of perturbation magnitude. For example, pouring grains into a container results in a pile at a particular angle of repose. This mechanical equilibrium configuration is jammed regularly but not reversibly jammed because in response to an external perturbation, the constituent particles will irreversibly rearrange, approaching a truly jammed configuration. Studying an ensemble of truly jammed, reversible states is thereby suitable for a plausible application of statistical mechanics under the present theory. These ensembles, inherently non-equilibrium systems, will not be governed by the commonly used parameters of equilibrium statistical mechanics, such as a bath temperature.

In recent studies theoretical mean-field models of glasses [66] have introduced the concept of an "effective temperature" as extracted from the FD relations in non-equilibrium systems. While not equivalent to the equilibrium bath temperature, the effective temperature reflects a change in the relaxation time-scale of the system. These non-equilibrium systems extend beyond glasses, and into granular media, where physical size of the constituent grains inhibits motion, allowing for jammed systems far from equilibrium. This concept has been furthered by computer simulations of granular media and other non-equilibrium soft-matter systems [67, 19, 68, 69, 70, 64]. It remains a question whether or not granular media can be characterized by an effective temperature, thus revealing a dynamic counterpart to the static "compactivity" as proposed by Edwards [46].

Athermal systems require the input of energy by an external source to explore the effective temperature [71]. One proposed method of calculating the effective

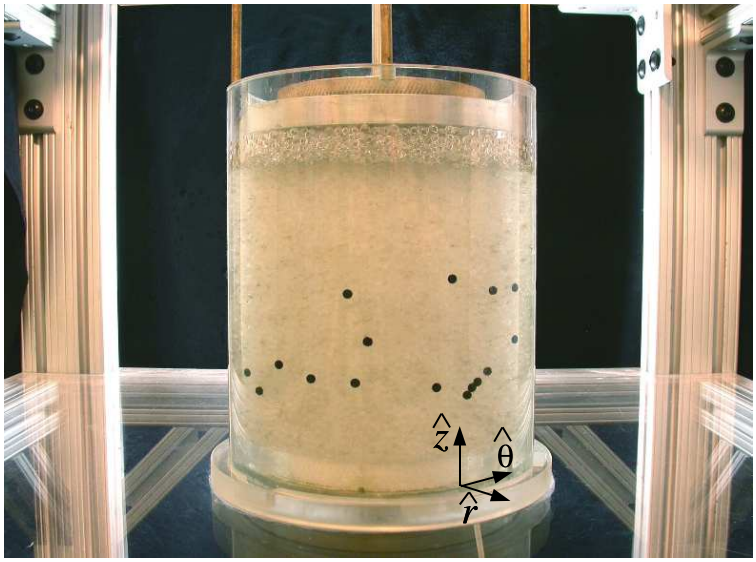

Figure 4.1: Picture of experimental set-up. Transparent acrylic grains and black tracers in a refractive index and density matched solution are confined between the inner cylinder of radius 5.08cm and the outer cylinder of radius 6.67cm.

temperature of a jammed granular system is a slow shearing procedure [72, 73, 74, 75, 76, 77, 78], leading to the design of the experiment we present in [79]. Slow shearing, at the quasi-static limit, allows for extrapolation towards an effective temperature of jammed, static, systems. The jammed system of interest is one of identical, spherical grains, confined between the two cylindrical walls of a 3D Couette cell. The grains are further confined by an external pressure in the vertical direction. The inner cylinder of the Couette cell is slowly rotated to induce shearing in the system. Tracer particles are inserted in the system, and their trajectories recorded via multiple cameras surrounding the system. The Couette cell is partially filled with a refractive index matched fluid to allow for system transparency. The cylindrical walls are roughened by gluing grains, identical to those of the bulk, such that crystallization is avoided.

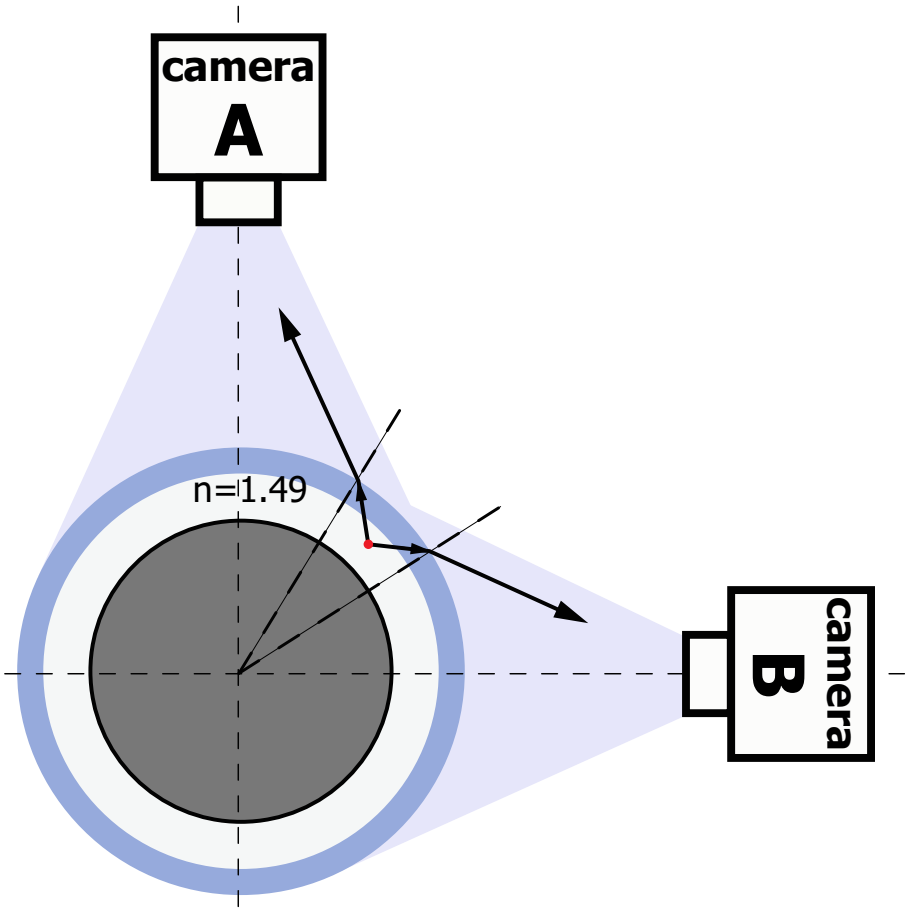

Figure 4.2: Top view of experimental set-up. The outer cylinder is made of the same material as acrylic grains ($n \simeq 1.49$). Once the refractive index is matched, light scattering from tracers will refract only one times on the outer surface of the outer cylinder. A single particle is captured by two cameras allowing the determination of the 3-dimensional coordinates of the particle, (r, θ, z).

The cameras record tracer particle trajectories throughout the bulk, recording data in cylindrical coordinates, $(r(t), \theta(t), z(t))$. Distributions of tracer particle displacements are measured in each direction. As gravity is the external force applicable to the mobility calculation in the current formalism, only displacements in the z-direction are applied to the FD relation. Additionally, average velocity profiles are calculated for each direction, first with constant shear rate, $\dot{\gamma}_e$, and further studied to determine shear rate dependence. Displacement measurements are further limited to the "constant mobility and diffusivity" (CMD) region, defined as the narrow range of radial coordinates such that the average vertical velocity is roughly independent on radial distance. The PDF of displacement distributions for each direction is presented. Further, fluctuations in displacement are determined for each cylindrical direction, and studied as a function of time. Radial displacement fluctuation is found to be sub-diffusive, while angular displacement fluctuation is found to be super-diffusive. Vertical displacement fluctuation is purely diffusive within the time scales of the experiment, allowing for the validity of the FD relations used herein. All displacement fluctuations are reduced to functions of angular displacement, and the results are presented. Such relationships permit scaling of the PDF curves with varying angular displacements due to changing shear rates.

Utilizing the FD relations presented above, the diffusivity and mobility in the z-direction are extracted from the tracer particle trajectories and the effective temperature is realized. This effective temperature is found to be independent of tracer particle properties, as shown in [79], and further independent of the slow-shear rate. Moreover, the effective temperature may then be considered a physical variable that characterizes the jammed granular system, with respect to

the generalization of the equilibrium statistical mechanics of Boltzmann, as applied to non-equilibrium systems.

We further study the limits within which this effective temperature may be a valid physical variable, as we determine mobility and diffusivity as a function of shear rate. While diffusivity appears independent of shear rate, even somewhat above the 'slow' regime, mobility shows a clear decrease in magnitude as we explore shear rates above the slow regime, resulting in an increase in the effective temperature as a function of shear rate.

In this paper, we will further report the experimental detail of particle dynamics in [79]. The outline is as follows:

4.2 Experimental Method

4.2.1 Experimental Setup

The experiment is performed using a three-dimensional (3D) Couette cell, as shown in Fig. 4.1, 4.2 and 4.3. The grains are confined between two cylinders of height 19.0cm. The inner cylinder is rotated via a motor, while the outer cylinder remains fixed. The walls of the cylinders, in contact with the grains, are roughened by means of a glued layer of identical granular material, thereby minimizing wall slip. The walls of the inner and outer cylinders are roughened by acrylic beads with diameter 3.97 and 1.59mm, respectively. Testing the experiment with a rough inner wall and a smooth outer wall resulted in packing crystallization. The grains are compacted by an external pressure of a specific value (typically 386 Pa), introduced by a moving piston at the top of the granular material, acting in the negative z-

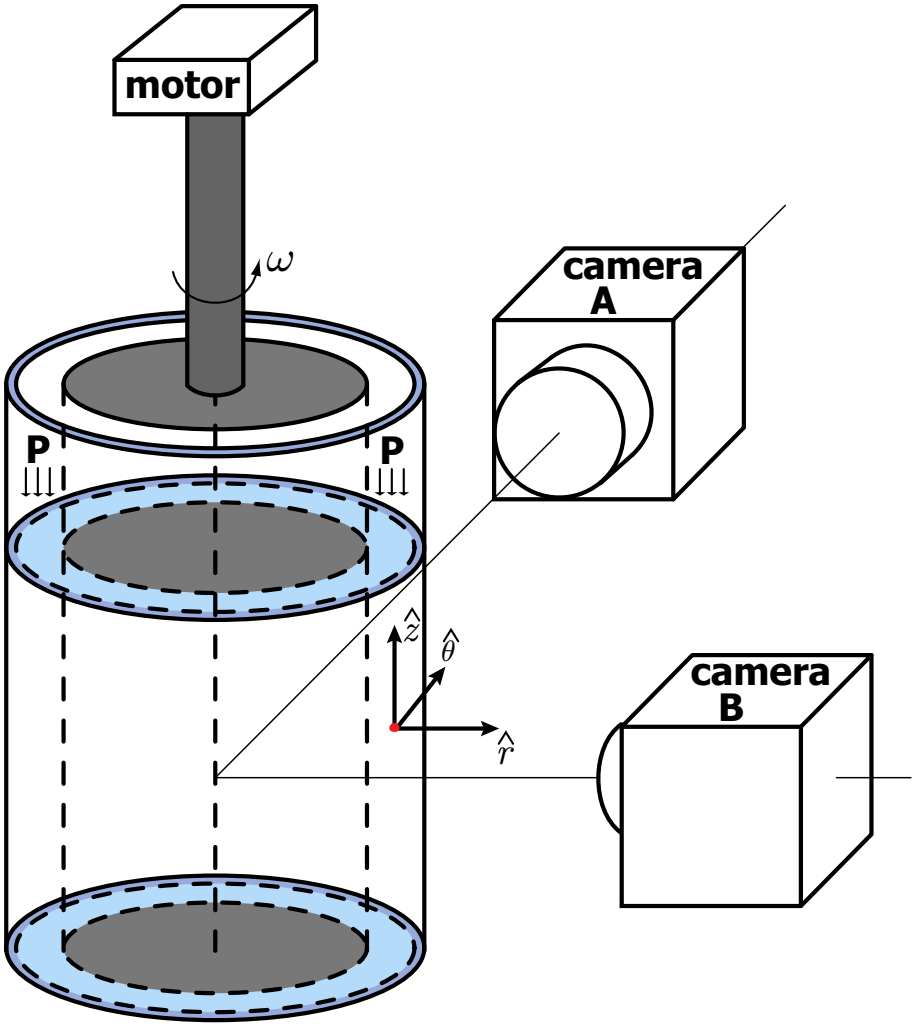

Figure 4.3: Sketch of experimental set-up. Note that the cylinder is surrounded by 4 cameras, in the sketch we plot only two cameras. A single particle is captured by two cameras allowing the determination of the 3-dimensional coordinates of the particle, (r, θ, z).

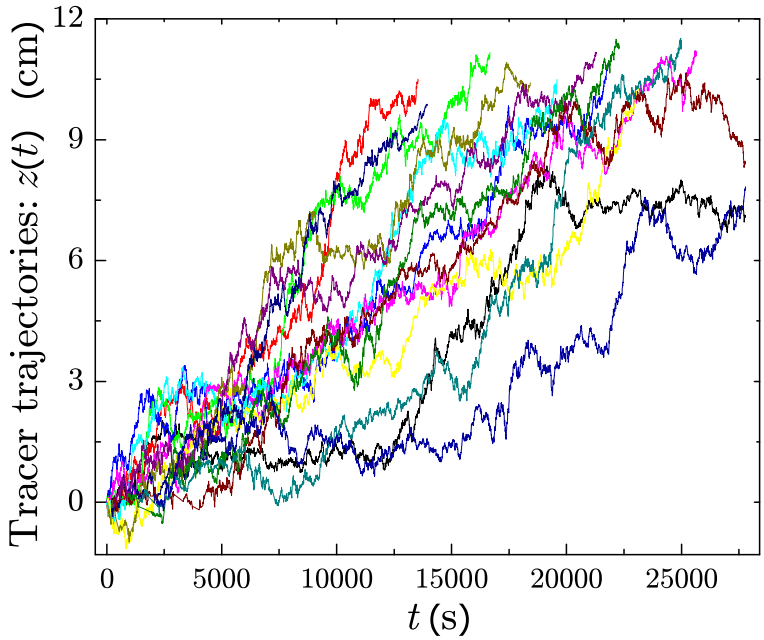

Figure 4.4: Trajectories of the 3.97mm nylon tracers in Packing 1 showing the diffusion and response to the gravitational force when sheared in the Couette cell.

direction.

Observation techniques are used to monitor the granular packing evolution as it explores the available jammed configurations. The Couette cell is sheared at the quasi-static limit, with slow frequencies $f = 0.2 \sim 4.2$ mHz defining the external shear-rate $\dot{\gamma}_e = 2\pi f R_1/(R_2 - R_1) = \omega R_1/(R_2 - R_1) = 0.004 \sim 0.084$ $\mathtt{s}^{-1}$, where $R_1 = 5.08$cm and $R_2 = 6.67$cm are the radius of the inner and outer cylinders, respectively, and ω is the angular velocity of the inner cylinder (Notice that R_1 and R_2 are measured after the walls are roughened by a glued layer of beads). The experiment is designed to measure the diffusivity and mobility of tracer particles [64, 79, 81], as opposed to tracking the motion of all constituent grains. The distance between the inner and outer cylinder is less than 10 grain diameters to prevent bulk shear band formation [77, 78, 74, 73, 76] that may interfere with the

experimental measurements by altering the diffusivity.

A refractive index matching suspending solution is employed in order to create a transparent sample. The suspending solution is also density matched to the grains in order to eliminate pressure gradients derived from gravity in the vertical direction, circumventing problems seen in previous experiments of compactivity [80] and other effects such as convection and size segregation such as the Brazil nut effect inside the cell [43]. The solution used in this experiment is approximately 74% weight fraction of cyclohexyl bromide and 26% decalin [82]. These steps avoids problems encountered in previous tests of compactivity.

4.2.2 Packing Preparation

The granular system is a bidisperse, 1:1 by mass, mixture of spherical, transparent Poly-methyl methacrylate (acrylic) particles, with density $\rho = 1.19$ and index of refraction $n \simeq 1.49$. The bidisperse mixture is used in an effort to inhibit crystallization of the system. The respective particle diameters are either 3.17mm and 3.97mm (Packing 1) or 3.97mm and 4.76mm (Packing 2). The approximate same size ratio of each bidisperse packing leads to approximately the same value of volume fraction for both, being 0.62 before shearing and 0.58 during shearing.

A negative consequence of utilizing a suspending solution includes possible modification of the friction coefficient between the grains. While this cannot be completely avoided, it is important to note that the liquid only partially fills the cell (see Fig. 4.1), such that the pressure of the piston is transmitted to the granular material exclusively, not to the fluid. Additionally, hydrodynamic effects from partial cell filling are avoided by the extremely slow rotational speeds applied

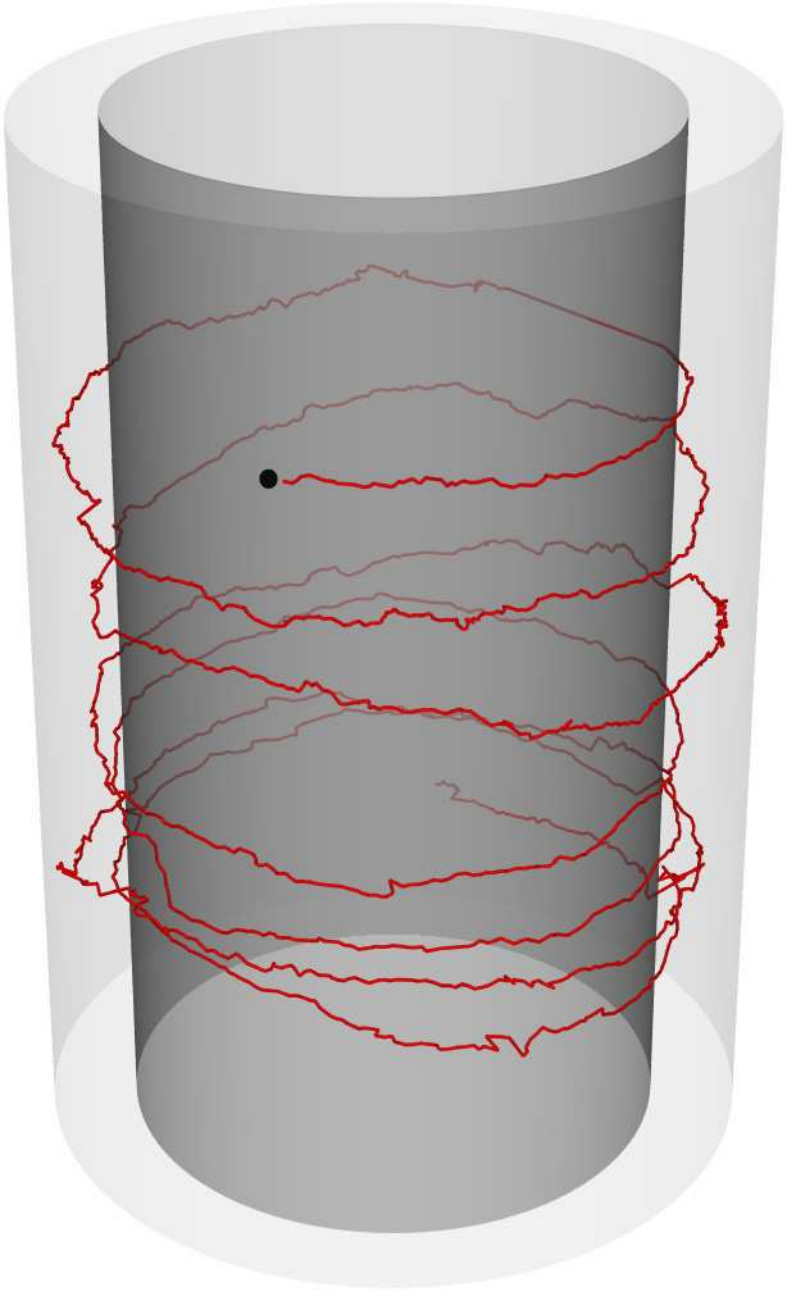

Figure 4.5: A typical trajectory of the 3.97mm nylon tracer for 3 hours in 3D plot. The dark gray and light gray cylinder indicate the outer surface of the sheared inner cylinder and the inner surface of the static outer cylinder respectively.

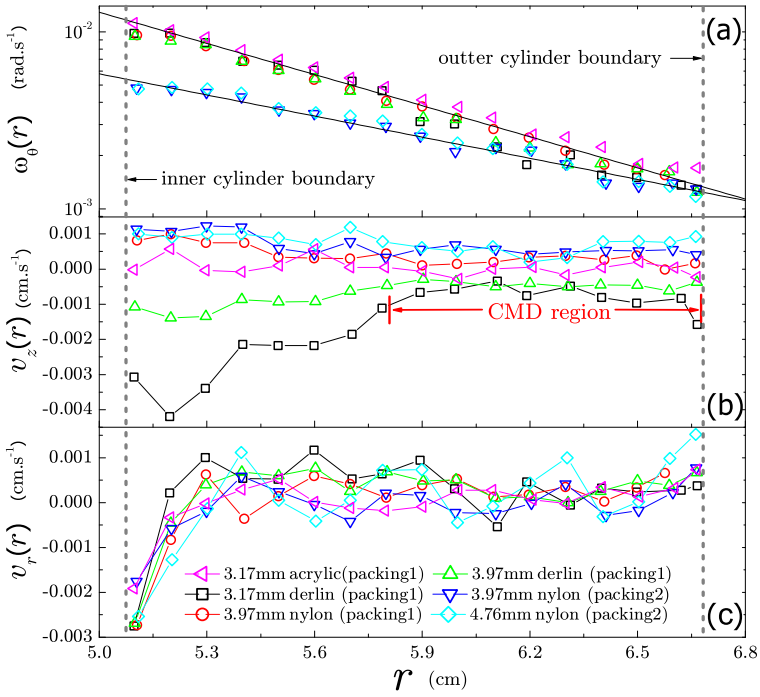

Figure 4.6: (a) Average angular velocity, $\omega_\theta(r)$, (b) Average vertical velocity, $v_z(r)$, and (c) Average radial velocity, $v_r(r)$, versus radial distance r for various tracers and different packings. Packing 1 and Packing 2 are run at $\dot{\gamma}_e = 0.048, 0.024\text{s}^{-1}$, respectively. In (a), solid lines are exponential fitting. In (b), the positive velocity of nylon tracer is due to the smaller density than acrylic's. The negative velocity of delrin tracer is due to the higher density than acrylic's.

to our system. The system remains very closely packed, such that particles are not free to float in the fluid. Therefore, the random motion of the particles is controlled by the 'jamming' forces exerted by the contacts between neighboring grains, not fluid mechanics.

4.2.3 Implementation of Fluctuation-Dissipation Theory

Cylindrical coordinates, $(r(t), \theta(t), z(t))$, of tracer particles are obtained by analyzing images acquired by four digital cameras surrounding the Couette cell. For

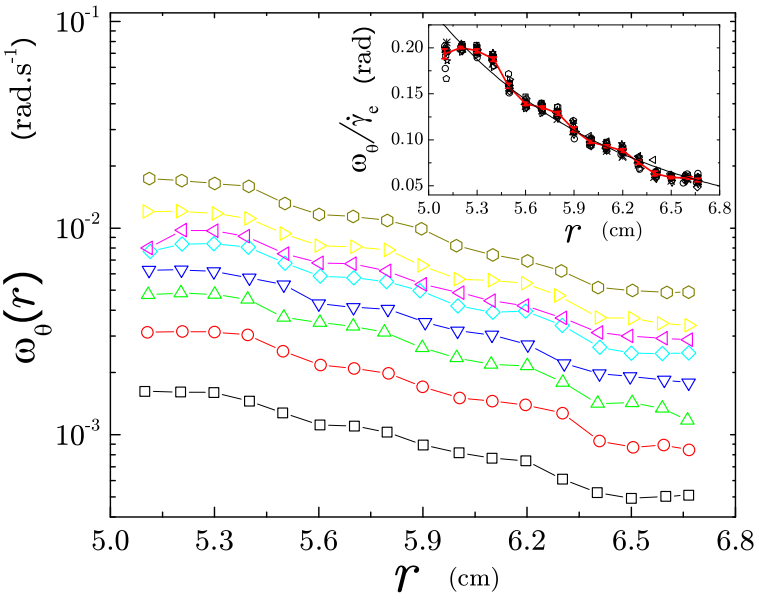

Figure 4.7: Average angular velocity of tracers, $\omega_\theta(r)$, versus radial distance r for various shear rate $\dot{\gamma}_e$ in Packing 2. Black square, red circle, green triangle, blue triangle-down, cyan diamond, magenta triangle-left, yellow triangle-right, dark yellow hexagon are corresponding to $\dot{\gamma}_e = 0.008, 0.016, 0.024, 0.032, 0.041, 0.048, 0.060, 0.084\text{s}^{-1}$, respectively. The inset plots the collapsing of average angular velocity scaled by shear rate, $\omega_\theta(r)/\dot{\gamma}_e$, versus radial distance r for various shear rate $\dot{\gamma}_e$. The red solid curve is the average result of the collapsing. The black solid curve is a exponential fitting.

systems in thermal equilibrium, a Fluctuation-Dissipation (FD) relation may be utilized in an effort to calculate the bath temperature of the system. This method may be extended to non-equilibrium systems, such as jammed granular systems presented in this study. The FD relation is defined as follows:

$$\langle [x(t+\Delta t) - x(t)]^2 \rangle \sim 2D\Delta t, \tag{4.1}$$

$$\langle [x(t+\Delta t) - x(t) \rangle \sim MF\Delta t, \tag{4.2}$$

$$\langle [x(t+\Delta t) - x(t)]^2 \rangle = \ 2T_{\text{eff}} \ \frac{\langle x(t+\Delta t) - x(t) \rangle}{F}. \tag{4.3}$$

The tracer particles must experience a constant force, F, in order to calculate the mobility as defined above. The most convenient constant, external, force, is gravity in the z-direction. If the effective temperature is to be regarded as an intensive variable of the non-equilibrium system, it requires independence from the tracer particles properties, and we present data in favor of this result. However, we acknowledge that temperature measures from multiple observables would be necessary to analyze the underlying thermodynamic meaning of T_{eff}.

4.2.4 Properties of Tracer Particles

Tracer particles added to the bulk must have properties unique from the grains comprising the bulk. However, tracer particles too small, or too large, with respect to the acrylic grains described previously, would result in erroneous measurements. Dynamics of tracer particles that were too small would be dominated by "perco-

lation effects" [83], resulting in larger than expected tracer particle displacements. Those too large would require shear rates above the quasi-static limit we propose to study, or possibly have no dynamics at all due to size limitations. With these notions in mind, two different types of tracers, nylon ($\rho' = 1.12$) and delrin ($\rho' = 1.36$), are employed, which result in different external forces, $F = (\rho' - \rho)Vg$, where ρ and ρ' are the densities of the acrylic particles and the tracers, respectively, V is the volume of the tracer particle and g the gravitational acceleration. Variations in tracer particle diameter and density allow us to study dynamical changes due to a change in constant external force, while we remain within a range appropriate to achieve results expected to be governed by the effective temperature.

4.2.5 Particle Tracking Technique

Four digital cameras symmetrically surround the shear cell to track the tracer particles with frame rate ~ 5 frame/s, as shown in Fig. 4.3. The outer cylinder is made of the same material as the grains (acrylic, $n \simeq 1.49$). The refractive index is matched by the fluid such that the system can be regarded as an optical whole, i.e., the light scattered from tracers refracts only once at the outer surface of the outer cylinder, as shown in Fig. 4.2. The determination of the 3D tracer position is achieved by a simple calculation considering both system geometry and 2D projections captured by two adjacent cameras.

Camera calibration and determination of relative position is important as a minimal asymmetry will result in a large calculation error of the tracer particles coordinates, $(r(t), \theta(t), z(t))$. As opposed to directly measuring relative positions of the cameras by physical devices, we utilize computer programming. In order to

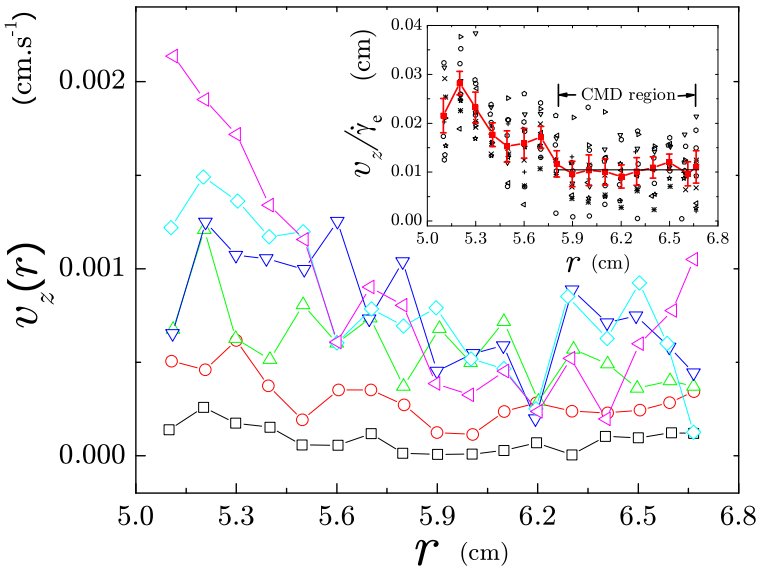

Figure 4.8: Average vertical velocity of tracers, $v_z(r)$, versus radial distance r for various shear rate $\dot{\gamma}_e$ in Packing 2. Black square, red circle, green triangle, blue triangle-down, cyan diamond, magenta triangle-left are corresponding to $\dot{\gamma}_e = 0.008, 0.016, 0.032, 0.048, 0.060, 0.084\text{s}^{-1}$, respectively. The inset plots the collapsing of average vertical velocity scaled by shear rate, $v_z(r)/\dot{\gamma}_e$, versus radial distance r for various shear rate $\dot{\gamma}_e$. The red solid curve is the average result of the collapsing.

simplify the calculation, we assume the camera to be a pinhole, meaning all light coming into the camera coincides at a single focal point.

Before each experiment, we record the images of a piece of grid paper attached to the surface of the outer cylinder, acting as the 2D projections of the outer cylinder for each camera. Next, we adjust the positions of four cameras until each camera can give the approximately same 2D projections of the outer cylinder. Then we use the computer program to generate a virtual cylinder, along with four virtual cameras, according to the geometry of the shear cell, In other words, we build a virtual space of the entire experimental setup and the respective geometrical relations between its elements.

From the previous calibration procedure, we have the relative positions of the four cameras to the shear cylinder with sufficient accuracy. In order to further calibrate and know the exact position of cameras, we adjust the relative position of cameras in our virtual space until the virtual 2D projection of the cylinder to the cameras coincides exactly with the actual projection, being the grid paper attached to the outer cylinder. When this procedure is accomplished, the virtual space exactly coincides with the real experimental setup space. Therefore the virtual relative position of cameras are also the real positions.

Furthermore, in our virtual space, any point with 3D coordinates, (r, θ, z), we can calculate its 2D coordinates in four virtual 2D projections, $(x_1, y_1) \sim (x_4, y_4)$, by considering the geometry relation to cameras. Oppositely, for any tracer particle, if we know its 2D coordinates in four 2D projections, $(x_1, y_1) \sim (x_4, y_4)$, we can exactly locate its 3D positions, (r, θ, z), since the virtual space is equal to the actual one. The resulting vertical trajectories of the tracers $z(t)$ are depicted in

Fig. 4.4 showing that the nylon tracers not only diffuse, but also move with a constant average velocity to the top of the cell. Fig. 4.5 shows a typical trajectory of tracer particle in 3D plotting.

4.3 Results

4.3.1 Average Velocity Profiles

We first study the velocity profiles for a fixed shear rate, $\dot{\gamma}_e$, followed by a study on the shear rate dependence in the next section. The average velocity profiles in the angular direction, $\omega_\theta(r)$, in the vertical direction, $v_z(r)$, and in the radial direction, $v_r(r)$, are obtained by averaging the velocities of all tracer particles over all times at each radius r, as shown in Fig. 4.6.

As observed in previous work [75], we find that $\omega_\theta(r)$ can be expressed in the exponential form demonstrated in Fig. 4.6a:

$$\begin{aligned}\omega_\theta(r) &= \lambda_1 \frac{\dot{\gamma}_e(R_2 - R_1)}{R_1} \exp(-\lambda_2 \frac{r - R_1}{R_2 - R_1}) \\ &= \lambda_1 \omega \exp(-\lambda_2 \frac{r - R_1}{R_2 - R_1}),\end{aligned} \tag{4.4}$$

where λ_1 and λ_2 are constants independent of shear rate, tracer size and tracer type, depending only on the type of packings and geometry of the shear cell. We find that $\lambda_1 = 0.77$ and 0.73, and $\lambda_2 = 2.15$ and 1.43 for Packing 1 and Packing 2, respectively. When $r = R_1$, $\omega_\theta(R_1) = \lambda_1\omega$ being the angular velocity of the first layer of grains closest to the sheared inner cylinder with angular velocity ω.

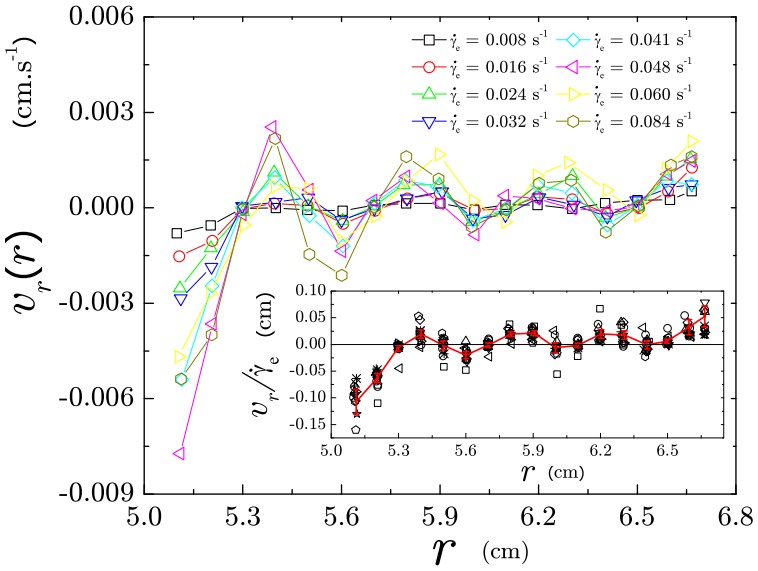

Figure 4.9: Average radial velocity of tracers, $v_r(r)$, versus radial distance r for various shear rate $\dot{\gamma}_e$ in Packing 2. Black square, red circle, green triangle, blue triangle-down, cyan diamond, magenta triangle-left, yellow triangle-right, dark yellow hexagon are corresponding to $\dot{\gamma}_e = 0.008, 0.016, 0.024, 0.032, 0.041, 0.048, 0.060, 0.084\text{s}^{-1}$, respectively. The inset plots the collapsing of average radial velocity scaled by shear rate, $v_r(r)/\dot{\gamma}_e$, versus radial distance r for various shear rate $\dot{\gamma}_e$. The red solid curve is the average result of the collapsing.

Therefore λ_1 $(0 < \lambda_1 < 1)$ can be taken as the efficiency of shearing, describing the amount of slip between the inner rotating cylinder and the first layer of grains it contacts. Packing 1 has a higher value of λ_1 than Packing 2, as the smaller grains follow the rotating inner cylinder more easily. On the other hand, when $r = R_2$, we find $\omega_\theta(R_2) = \lambda_1 \omega \exp(-\lambda_2)$, the velocity of the last layer of grains closest to the static outer cylinder. This velocity is non-zero, so that the shear band is located right at the outer cylinder, avoiding the formation of shear bands in the bulk.

In order to avoid the tracer particles sticking to the outer cylinder surface and forcing its velocity to zero, we glue smaller size particles to roughen the outer

cylinder. This roughens the surface of the outer cylinder and avoids crystallization. Further, this allows slipping of the bulk particles at the outer cylinder, forcing the shear band to be located exactly at the outer cylinder, not in the bulk. The glued particles are 1.59mm, smaller than the sheared granular material. The mean angular and vertical velocity, ω_θ and v_z, of tracer particles do not decay to zero even if the tracers come close to outer cylinder surface. (See Fig. 4.7 and Fig. 4.8 at $r = R_2$).

The exponential decay of $\omega_\theta(r)$ results in a local shear rate, $\frac{d\omega_\theta(r)}{dr}$, dependent on radial distance. In the region near the outer cylinder, $\omega_\theta(r)$ decays slowly with increasing r which leads to weak dependence of $\frac{d\omega_\theta(r)}{dr}$ on the radial distance r. If we do Taylor expansion at $r = R_2$, the average angular velocity of the tracers, $\omega_\theta(r)$, can be approximated to a linear function of r, i.e., $\omega_\theta(r) \approx \lambda_1\omega \exp(-\lambda_2) - r\frac{d\omega_\theta(r)}{dr}$ with constant local shear rate $\frac{d\omega_\theta(r)}{dr} = 0.021\ \mathrm{s}^{-1}\mathrm{cm}^{-1}$. The diffusivity and mobility of the tracer particles strongly depend on the local rearrangement of the grains. A constant shear rate results in homogenous local rearrangement of the packings ensuring that the diffusivity and mobility of tracers, dependent on local shear rate, remain approximately independent of r. As shown in Fig. 4.6b, we find a plateau in the vertical velocity profile which can be further seen in Fig. 4.8. Similar behavior is observed in the vertical diffusivity profile, $D_z(r)$ as shown in Fig. 4.16, which we will discuss in detail in Section 4.3.4. We denote this the "constant mobility and diffusivity region", i.e., CMD region, $5.80\mathrm{cm} < r < 6.67\mathrm{cm}$. Contrary to prior work [72, 73, 74, 75, 76, 77, 78] on sheared granular matter in the Couette cell, our experiment focuses only a narrow gap, 15.9mm, of Couette cell. The CMD region allows us to well define the diffusivity and mobility of the tracer particles, such

that we can calculate the average vertical velocity, v_z, and the average vertical diffusivity, D_z, by averaging the velocities of all tracers over all times in the CMD region, significantly improving the statistics. In this study, the statistical average and the measurements of tracer fluctuations will be confined only to the CMD region.

We find $v_r(r)$ to be flat for different types of tracer particles and for different packings except when the tracers are close to the inner and outer cylinder, i.e., $r = R_1$ and $r = R_2$, as shown in Fig. 4.6c. $v_r(R_1)$ is negative and $v_r(R_2)$ is positive, indicating the inner and outer cylinder walls can slightly attract the tracers. It should be noted that the statistics presented in this study does not incorporate data from the regions close to the inner and outer cylinder to avoid these boundary effects.

4.3.2 Shear Rate Dependent Average Velocity Profiles

Next, we study the dependence of the particle velocity on the external shear rate. According to Eq. (4.4), the velocity profile in the angular direction, $\omega_\theta(r)$, is proportional to the external shear rate $\dot{\gamma}_e$. We can collapse $\omega_\theta(r)$ by scaling the shear rate. The results are shown in the inset of Fig. 4.7 for Packing 2. The collapsing of $\omega_\theta(r)/\dot{\gamma}_e$ shows a periodic shape superimposed to exponential decay with a very small amplitude, also found in the velocity profile of $v_r(r)$ (see Fig. 4.9). The periodic length is roughly equal to the grain particle size and reflects the different layers of grains in the radial direction. This periodicity is weaker in Packing 1 than Packing 2, since the particle size of Packing 1 is smaller than that of Packing 2.

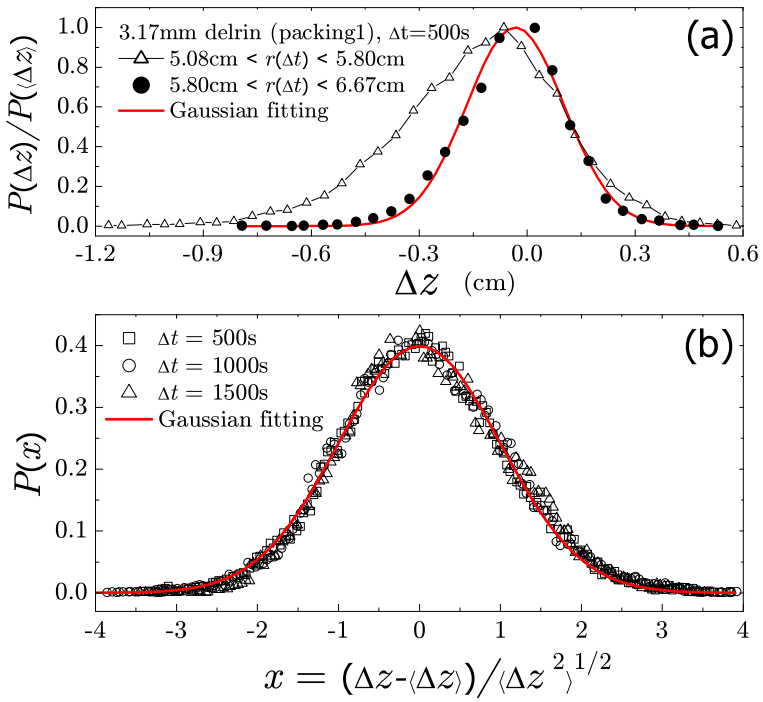

Figure 4.10: (a) PDF of the vertical displacements, $P(\Delta z)$, of the 3.17mm delrin tracers in Packing 1 for a given time interval $\Delta t = 50$s, and with $\dot{\gamma}_e = 0.048\text{s}^{-1}$. Tracer trajectories are split into sub-trajectories confined in two regions, (i): 5.08cm $< r <$ 5.80cm, which is close to inner rotating cylinder, and (ii): 5.80cm $< r <$ 6.67cm, which is far away from inner rotation cylinder. We compared the calculated $P(\Delta z)$ by using the sub-trajectories from the regions of (i) and (ii) respectively, which are plotted as black triangle and black circle. See more details in the main text. (b) PDF of the vertical displacements, $P(\Delta z)$, of the 3.97mm nylon tracers in Packing 1 with $\dot{\gamma}_e = 0.048\text{s}^{-1}$, shifted by the average displacement $\langle \Delta z \rangle$ and scaled by the root-mean-square deviation $\langle \Delta z(t)^2 \rangle^{1/2}$. The red solid curve is a Gaussian distribution, $P(x) = 0.4\text{e}^{-x^2/2}$.

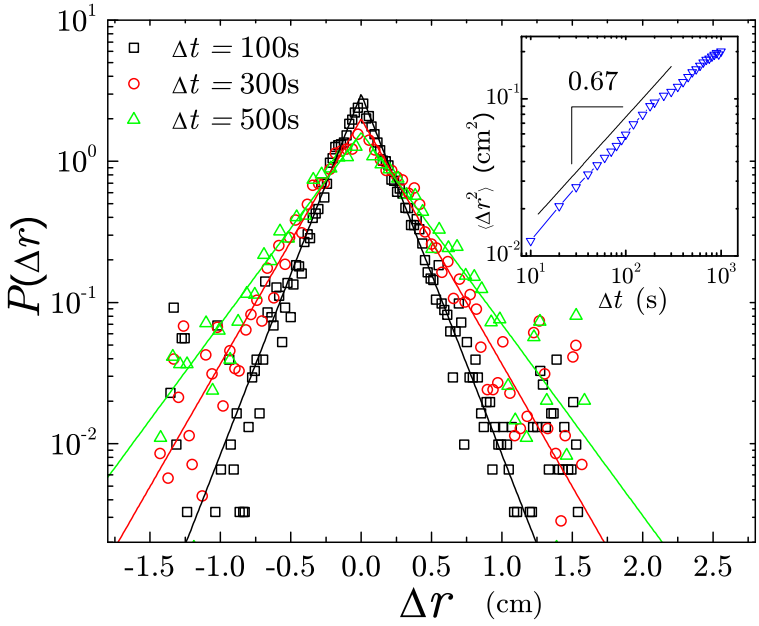

Figure 4.11: PDF of the radial displacements, $P(\Delta r)$, of the 3.97mm nylon tracers in Packing 1 with $\dot{\gamma}_e = 0.048\text{s}^{-1}$ for different time intervals. A symmetric distribution around zero displacement indicates that there is no net flow in the radial direction. The solid lines are exponential fitting, $P(\Delta r) \sim \exp(-\frac{|\Delta r|}{r_o})$, where $r_o = 0.17, 0.25, 0.32$ for $\Delta t = 100, 300, 500$s, respectively. The inset shows the rms fluctuations, which gives the value of $\alpha = 0.67$.

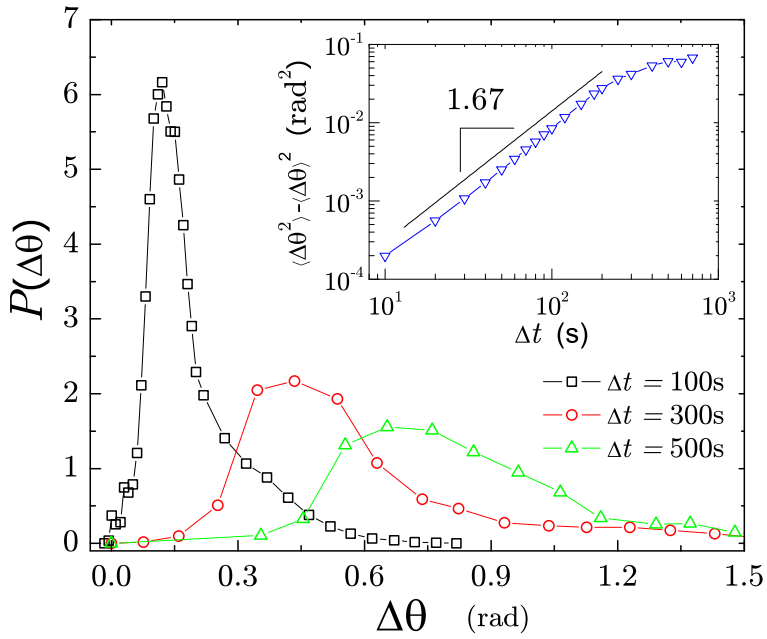

Figure 4.12: PDF of the angular displacements, $P(\Delta\theta)$, of the 3.97mm nylon tracers in Packing 1 with $\dot{\gamma}_e = 0.048\text{s}^{-1}$ for different time intervals. Due to Taylor dispersion effects the distribution shows an asymmetric shape. The rms fluctuations shown in the inset reveal a faster than diffusion process.

The collapsing method can be further applied to $v_z(r)$, as seen in Fig. 4.8. After scaling by the shear rate, $v_z(r)/\dot{\gamma}_e$ also shows a flat plateau indicating the CMD region.

4.3.3 Probability Distribution of Displacements

Fig. 4.10a shows the results of the probability distribution of the displacements Δz in the vertical direction for a given time interval Δt. The data corresponds to the 3.17mm delrin tracers in Packing 1. Usually, 20 tracers are used for calculations. Tracer trajectories are split into sub-trajectories confined in two regions, (i): 5.08cm $< r <$ 5.80cm, close to the inner rotating cylinder, and (ii): 5.80cm $< r <$ 6.67cm, i.e., CMD region, close to the outer cylinder. We compare the calculated $P(\Delta z)$ by using the sub-trajectories from the regions of (i) and (ii) respectively, which are plotted as black triangle and black circle in the Fig. 4.10a. The data in the inner region (i) clearly display an asymmetric tail for $\Delta z < 0$. This extra spreading is similar to the phenomena of the Taylor dispersion [84].

Taylor dispersion appears when diffusion couples with the gradient of flow giving rise to a larger dispersion along the flowing direction (see for instance [76] for a study of Taylor dispersion in granular materials). In the present experiment, the shear rate of granular flow in the angular direction exhibits exponential decay, as shown in Fig. 4.6b. The larger shear rate in the inner region (i) results in larger packing rearrangement, which gives rise to a larger dispersion in the vertical direction. In this case it is not possible to extract the bare diffusion constant. On the contrary, for the region (ii), i.e., CMD region, as we mentioned, the gradient of the flow, i.e., the shear rate is approximately constant, giving rise to a Gaussian

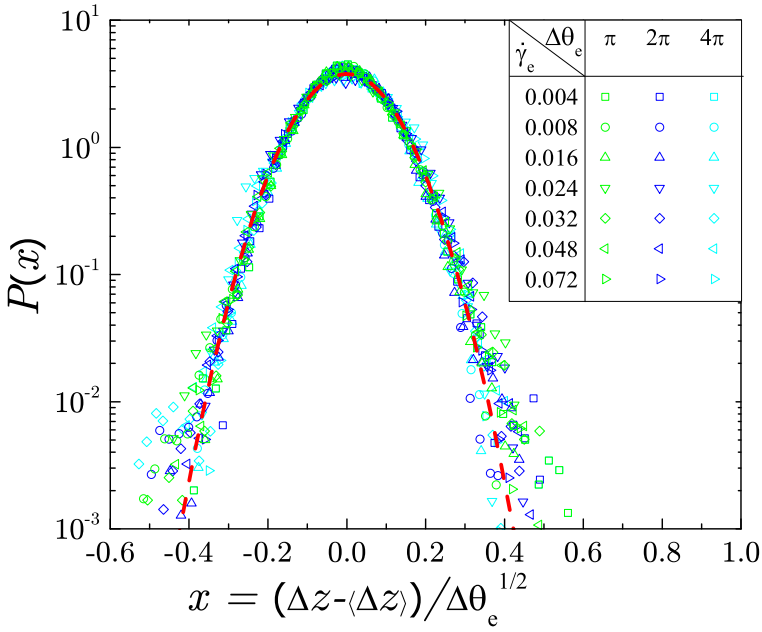

Figure 4.13: PDF of the vertical displacements, $P(\Delta z)$, of the 4.76mm nylon tracers in Packing 2 for various effective angular displacement $\Delta\theta_e$ and effective shear rate γ_e. The PDFs are scaled by ${\Delta\theta_e}^{1/2}$ and shifted by the mean displacement $\langle\Delta z\rangle$. The red dashed line is the Gaussian fitting, $P(x) \sim \exp[-(\frac{x}{0.147})^2]$. The collapsing of PDFs indicates that the RMS fluctuations of the vertical displacements follow the relation, $\langle\Delta z^2\rangle \sim \Delta\theta_e$.

diffusion, as shown in Fig. 4.10a. By measuring the width and the mean value of this Gaussian distribution of

$$\begin{aligned} P(\Delta z) &\sim \exp[-\frac{(\Delta z - \langle \Delta z \rangle)^2}{2\langle \Delta z^2 \rangle}] \\ &\sim \exp[-\frac{(\Delta z - M_z F \Delta t)^2}{4 D_z \Delta t}], \end{aligned} \tag{4.5}$$

we can define the diffusivity and mobility, D_z and M_z, which lead to the effective temperature of the granular packing discussed in the following section. In the Fig. 4.10b, we define a new scaled variable $x = \frac{\Delta z - \langle \Delta z \rangle}{\langle \Delta z^2 \rangle^{1/2}}$ and plot $P(x)$ for different Δt, all the curves are found to collapse into a single curve

$$P(x) \sim \mathrm{e}^{-x^2/2}. \tag{4.6}$$

In this experiment, we will focus our measurements in the region away from the inner boundary (region (ii), i.e., CMD region), where the mobility is a constant (as shown a plateau in the inset of Fig. 4.8) and Taylor dispersion effects are absent.

We find exponential fluctuations for the probability distributions of the tracer particles in the radial direction as shown in Fig. 4.11,

$$P(\Delta r) \sim \mathrm{e}^{-\frac{|\Delta r|}{r_o}}, \tag{4.7}$$

where r_o is a function of Δt. The symmetric shape for $P(\Delta r)$ indicates the absence of a shear induced segregation, as observed with multiple sizes of grains, as there is no net flow of the tracer particles towards either cylindrical wall within the time-scales of the experiment. We also observe no average motion of the tracer

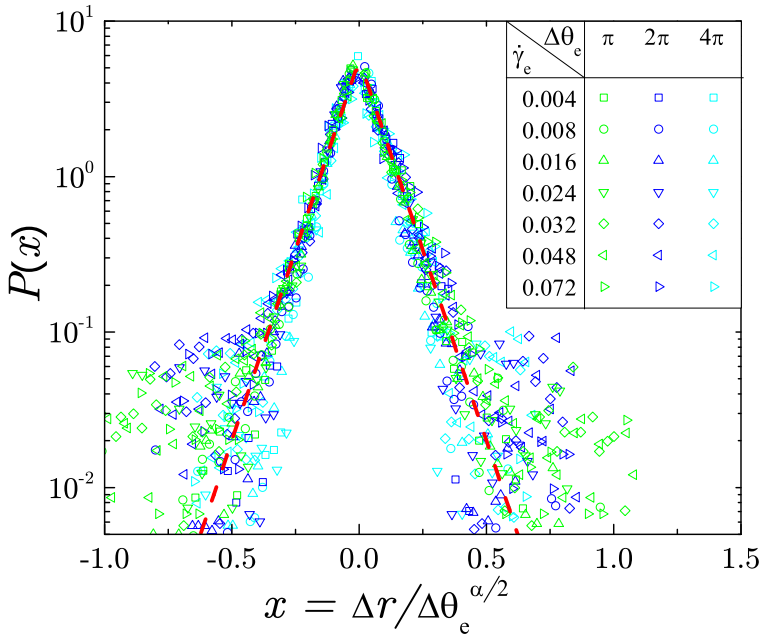

Figure 4.14: PDF of the radial displacements, $P(\Delta r)$, of the 4.76mm nylon tracers in Packing 2 for various effective angular displacement $\Delta\theta_e$ and effective shear rate γ_e. The PDFs are scaled by ${\Delta\theta_e}^{\alpha/2}$, where $\alpha = 0.67$. The red dashed line is exponential fitting, $P(x) \sim \exp(-\frac{|x|}{0.089})$. The collapsing of PDFs indicates that the RMS fluctuations of the radial displacements follow the relation, $\langle \Delta r^2 \rangle \sim {\Delta\theta_e}^{\alpha}$.

particles towards the center of the Couette cell except within a small range of radial distance, around 0.12cm, close to both walls where particles experience a slight attraction to boundaries. These features are shown in Fig. 4.6c and Fig. 4.9.

The analysis of the radial displacement fluctuation reveals a power law, sub-diffusive, process:

$$\langle \Delta r^2 \rangle \sim \Delta t^{\alpha} \tag{4.8}$$

as shown in Figure 8, where $\alpha = 0.67$ for both the delrin and nylon tracers.

The data taken for the angular displacement is in the direction of the flow, and affected by Taylor dispersion as shown in the non-Gaussian tail of the displacement distribution $\Delta\theta(t)$ in Fig. 4.12. This leads to a power law, super-diffusive process, illustrated by

$$\langle \Delta\theta^2 \rangle \sim \Delta t^{\beta} \tag{4.9}$$

as seen in the analysis of the fluctuations of $\Delta\theta$ shown in Fig. 4.12, where $\beta = 1.67$ and 1.30 for Packing 1 and Packing 2 respectively.

We further study how shear rate affects the displacement probability distribution. We find that for small shear rate, the probability distributions of displacements in the three cylindrical coordinates are independent of the shear rate, depending only on the sheared displacement, i.e., the external rotating displacement, defined as

$$\begin{aligned}\Delta\theta_e &= \dot{\gamma}_e \Delta t \\ &= \omega \Delta t R_1/(R_2 - R_1) \\ &= \Delta\theta_i R_1/(R_2 - R_1)\end{aligned} \tag{4.10}$$

where $\Delta\theta_i$ is the rotating displacement of the inner cylinder. This result is expected. Since we shear the Couette cell very slowly, the diffusion of the tracers depends only the number of granular packing configurations sampled by the Couette cell, which depends only on the sheared displacement.

As emphasized in the previous text, the statistical average and the measurements of the tracer fluctuations is confined to the CMD region, such as the D_z shown in Fig. 4.17a. We calculate the D_z by measuring the width and the mean value of the Gaussian distribution of $P(\Delta z)$, and obtain the $P(\Delta z)$ by averaging the displacement fluctuations of all tracers over all time in the CMD region. Next, we apply a different method to reveal how $D_z(r)$ depends on the radial distance r, as shown in the Fig. 4.16. We first obtain $P(\Delta z, r)$ for a certain radial distance r, then we calculate $D_z(r)$ by measuring the width and the mean value of the Gaussian distribution of $P(\Delta z, r)$. In Fig. 4.16, we see that the tracer particles have higher diffusivity close to the inner cylinder than the outer. Since $D_z \sim \dot{\gamma}_e$, we can collapse all the $D_z(r)$ for various shear rates, as shown in the inset of Fig. 4.16. The collapse of $D_z(r)/\dot{\gamma}_e$ shows a plateau close to the outer cylinder, consistent with our previous discussion of the CMD region.

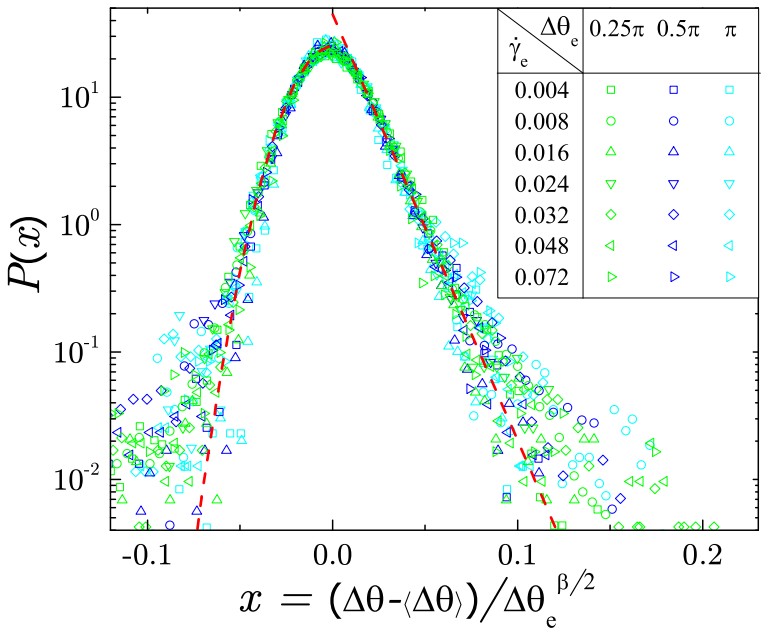

Figure 4.15: PDF of the angular displacements, $P(\Delta\theta)$, of the 4.76mm nylon tracers in Packing 2 for various effective angular displacement $\Delta\theta_e$ and effective shear rate γ_e. The PDFs are shifted by the mean displacement $\langle\Delta\theta\rangle$ and scaled by ${\Delta\theta_e}^{\beta/2}$, where $\beta = 1.30$. The red dashed line are Gaussian and exponential fittings for $x < 0$ and $x > 0$, respectively. The collapsing of PDFs indicates that the rms fluctuations of the angular displacements follow the relation, $\langle\Delta\theta^2\rangle \sim {\Delta\theta_e}^{\beta}$.

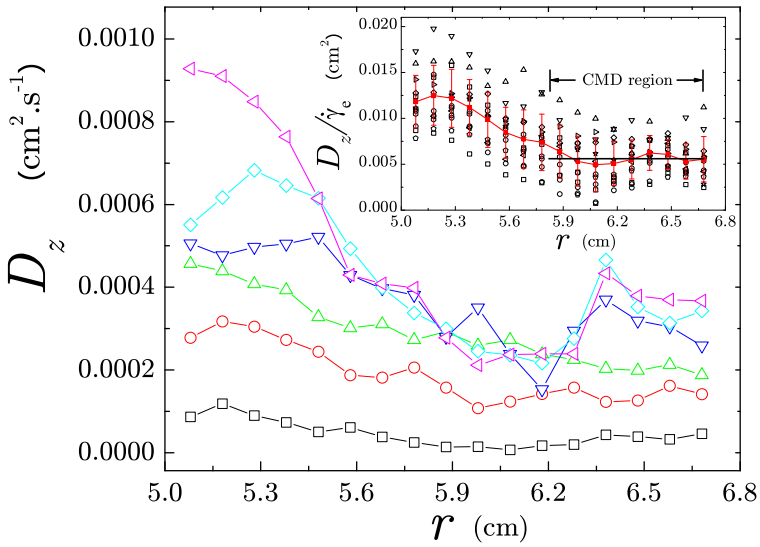

Figure 4.16: Diffusivity D_z versus radial distance r for various shear rate $\dot{\gamma}_e$ in Packing 2. Black square, red circle, green triangle, blue triangle-down, cyan diamond, magenta triangle-left are corresponding to $\dot{\gamma}_e = 0.008, 0.016, 0.032, 0.048, 0.060, 0.084\text{s}^{-1}$, respectively. The inset plots the collapsing of diffusivity scaled by shear rate, $D_z/\dot{\gamma}_e$, versus radial distance r for various shear rate $\dot{\gamma}_e$. The red solid curve is the average result of the collapsing.

$$\langle [z(t+\Delta t) - z(t)]^2 \rangle \sim \Delta\theta_e \tag{4.11a}$$

$$\langle [r(t+\Delta t) - r(t)]^2 \rangle \sim \Delta\theta_e{}^{\alpha} \tag{4.11b}$$

$$\langle [\theta(t+\Delta t) - \theta(t)]^2 \rangle \sim \Delta\theta_e{}^{\beta} \tag{4.11c}$$

Eq. (4.11) implies that one can collapse the probability distribution of the displacements, $P(\Delta z)$, $P(\Delta r)$ and $P(\Delta\theta)$ for different shear rates and time intervals by scaling Δz, Δr and $\Delta\theta$ respectively to $\Delta z/\Delta\theta_e{}^{1/2}$, $\Delta r/\Delta\theta_e{}^{\alpha/2}$ and $\Delta\theta/\Delta\theta_e{}^{\beta/2}$. The results are presented in Fig. 4.13, 4.14 and 4.15.

Packing 1, 1:1 mass mixture of 3.17mm & 3.97mm acrylic beads, $\dot{\gamma}_e = 0.048\text{s}^{-1}$					
tracer	d (mm)	ρ (g·cm^{-3})	D_z (10^{-8} m^2·s^{-1})	M_z (10^{-2} s·kg^{-1})	T_{eff} (10^{-7} J)
acrylic	3.17	1.19	2.5 ± 0.3		
delrin	3.17	1.36	2.4 ± 0.3	24 ± 3	1.0 ± 0.2
delrin	3.97	1.36	1.2 ± 0.1	9.3 ± 0.9	1.3 ± 0.2
nylon	3.97	1.12	1.1 ± 0.1	9.5 ± 0.9	1.2 ± 0.2
ceramic	3.97	3.28		2.2 ± 0.2	
brass	3.97	8.4		1.7 ± 0.1	
Packing 2, 1:1 mass mixture of 3.97mm & 4.76mm acrylic beads, $\dot{\gamma}_e = 0.024\text{s}^{-1}$					
tracer	d (mm)	ρ (g·cm^{-3})	D_z (10^{-8} m^2·s^{-1})	M_z (10^{-2} s·kg^{-1})	T_{eff} (10^{-7} J)
nylon	3.97	1.12	1.8 ± 0.1	19.0 ± 0.9	0.95 ± 0.07
nylon	4.76	1.12	1.6 ± 0.1	15.7 ± 0.4	1.0 ± 0.1

Table 4.1: Diffusivity and mobility for the different types of tracer and packings.

4.3.4 Effective Temperature

We present results for the diffusivity in the z direction, the only direction where the effective temperature can be calculated due to the vertically acting external force. The Gaussian distribution in $P(\Delta z)$ allows us to apply the FD relation to the particle displacements, as the diffusivity is proportional to the variance of a Gaussian distribution in displacements. Exponential fluctuations do not possess this same property, but it is important to note that the radial direction has no constant applied external force. It remains a possibility that a well-defined effective temperature for displacements in the radial direction could exist. To test whether the effective temperature is isotropic, as done in [85], may be of great interest in future studies.

A common method of performing a time average to measure transport coefficients is employed (see Chapter 5.3 in [86]) by dividing the trajectory of a single tracer particle into a series of trajectories, having evenly spaced start times, separated by time interval Δt. The diffusion constant is obtained by averaging over

the aggregate of tracers and over the initial time intervals, allowing for the use of merely 20 tracer particles in this particular system. Correlations between measurements are ensured to have decayed almost to zero, rendering time-translational invariance valid in this system, without any measurable"aging", since under shearing, system reaches the "stationary state" [51]. Furthermore, doubling the number of tracer particles leaves D_z unchanged, indicating independence of the diffusion constant from the number of tracers that explore the jammed configurations of this non-equilibrium system.

Analysis of the vertical particle displacements in the CMD region reveals a Gaussian distribution, broadening over time, as seen in Fig. 4.10 and Fig. 4.13. For sufficiently long times period, the mean square fluctuations grow linearly (see Fig. 4.17a):

$$\langle [z(t+\Delta t) - z(t)]^2 \rangle \sim 2D_z \Delta t, \tag{4.12}$$

where D_z is the self-diffusion constant in the vertical direction. For the both nylon and delrin 3.97mm tracers in Packing 1 we obtain $D_{z\ 3.97\text{mm}} \approx (1.15 \pm 0.1) \times 10^{-8}$ m^2/s.

Figure 4.17b shows mean value tracer particle positions, extracted from the peak of the Gaussian distribution, as a function of time. The mobility in the vertical direction, M_z, is defined as

$$\langle z(t+\Delta t) - z(t) \rangle \sim M_z F \Delta t. \tag{4.13}$$

The applied force on the tracers, $F = (\rho - \rho')Vg$, is the gravitational force due to density mismatch where ρ and ρ' are the densities of the acrylic particles and the

tracers, respectively, V is the volume of the tracer particle and g the gravitational acceleration. The value of the mobility for the both nylon and delrin 3.97mm tracers in Packing 1 is $M_{z\ 3.97\text{mm}} \approx (9.4 \pm 0.9) \times 10^{-2}$ s/kg.

Fig. 4.17a further reveals a downward curvature of the mean-square fluctuations, for sufficiently long times period. Additionally, an apparent cut-off time for the tracer particles fluctuation measurements is shown. These effects are due to the finite size effect imposed upon the tracers by the finite trajectories and should be inversely proportional to the tracer particles velocities. Tracer particles with larger mobility will have larger mean velocities and take a shorter time to complete its trajectory in the cell. The cut-off discussed in reference to Fig. 4.17a is prominently displayed in the 3.17mm delrin tracers of Packing 1, having the largest mobility, hence increased mean velocities, as shown in Fig. 4.17b. The larger mobility results in the shortest cut-off time for the diffusivity. Conversely, 3.97mm delrin tracers of Packing 1 have a smaller mobility, hence a longer cut-off time for the diffusivity. It is important to note that for all tracer particles studied here, the cut-off is observed for distances larger than a few particles diameters, ensuring that the study examines the structural motion of the grains and not internal motion inside of "cages".

According to a Fluctuation-Dissipation relation, we calculate T_{eff}:

$$T_{\text{eff}} = \frac{F\langle[z(t+\Delta t) - z(t)]^2\rangle}{2\langle z(t+\Delta t) - z(t)\rangle}. \tag{4.14}$$

Fig. 4.17c shows a parametric plot of fluctuations and responses, with Δt, as the parameter, as extracted from Fig. 4.17a and Fig. 4.17b. A linear relationship exists between diffusivity and mobility, with a slope of T_{eff}. We obtain for the both

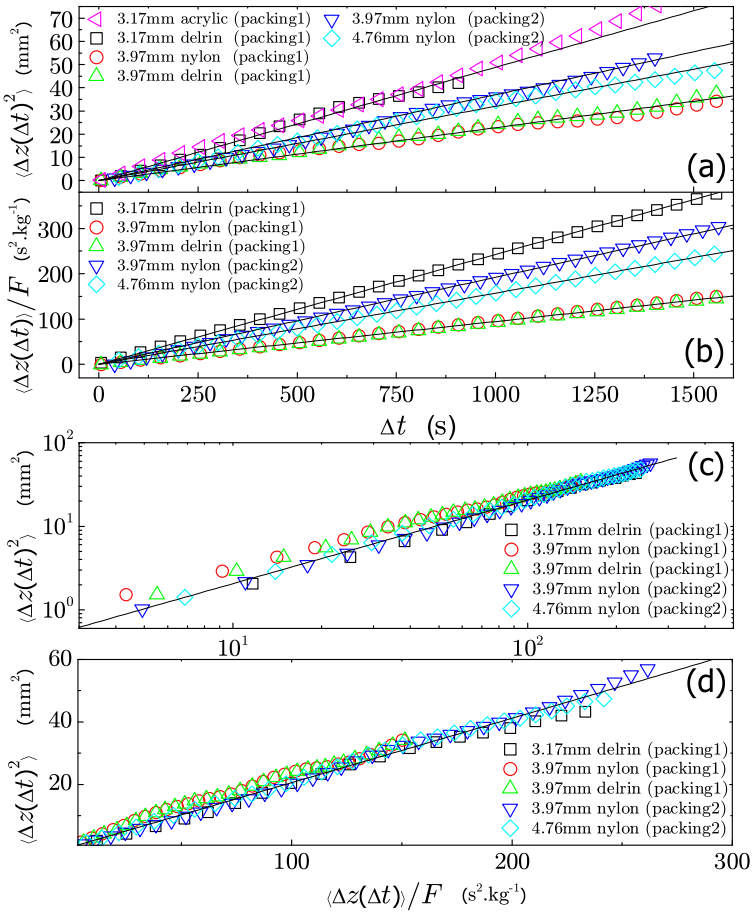

Figure 4.17: (a) Autocorrelation function of tracers. (b) Response function of tracers. (c) Log-log plot of effective temperatures for various tracers and different packings as obtained from a parametric plot of their autocorrelation function versus response function. (d) Same as (c) but in a linear-linear plot. The slopes for different tracer diffusivity vs. mobility curves return the same average value of $T_{\text{eff}} \approx (1.1 \pm 0.2) \times 10^{-7}$J as given by Eq. (4.3).

nylon and delrin 3.97mm tracers in Packing 1, $T_{\text{eff}} \approx (1.25 \pm 0.2) \times 10^{-7}$J.

If the effective temperature is to be regarded as an intensive thermodynamic quantity, changing the tracer particle size should give rise to a different diffusion and mobility yet result in the same measurement of effective temperature. The above calculation is repeated for delrin tracers of 3.17mm in Packing 1. We find that while the mobility and diffusivity change dramatically with respect to tracers of 3.97mm, ($D_{z\ 3.17\text{mm}} = (2.4 \pm 0.3) \times 10^{-8}$ m^2/s and $M_{z\ 3.17\text{mm}} = (2.4 \pm 0.3) \times 10^{-1}$ s/kg) as shown in Table 4.1, due to the change in tracer size, their ratio remains unchanged. In all cases D_z and M_z are inversely proportional to the size of the tracers, but the effective temperature remains approximately the same, as seen in Fig. 4.17c, with an average value over all tracers of

$$T_{\text{eff}} \approx (1.1 \pm 0.2) \times 10^{-7}\text{J}. \tag{4.15}$$

Though this effective temperature is high with respect to the bath temperature, we note that a plausible scale for the system energy [71], is $(\rho - \rho')gd$, the gravitational potential energy to move a nylon tracer particle one particle diameter, d. A corresponding temperature would arise from the conversion of this energy into a temperature via the Boltzmann constant, k_B, is $T_{\text{eff}} = 2.7 \times 10^{13} k_B T$ at room temperature (T = 300K). This specific value serves as a coarse-grained estimate, since the tracer size and density clearly shift its value, and we focus on the order of magnitude. This large value is expected [71], and agrees with computer simulation estimates for an athermal granular system [64]. Therefore, our calculated value for T_{eff} in a sheared granular system appears reasonable within the boundaries of the present theory.

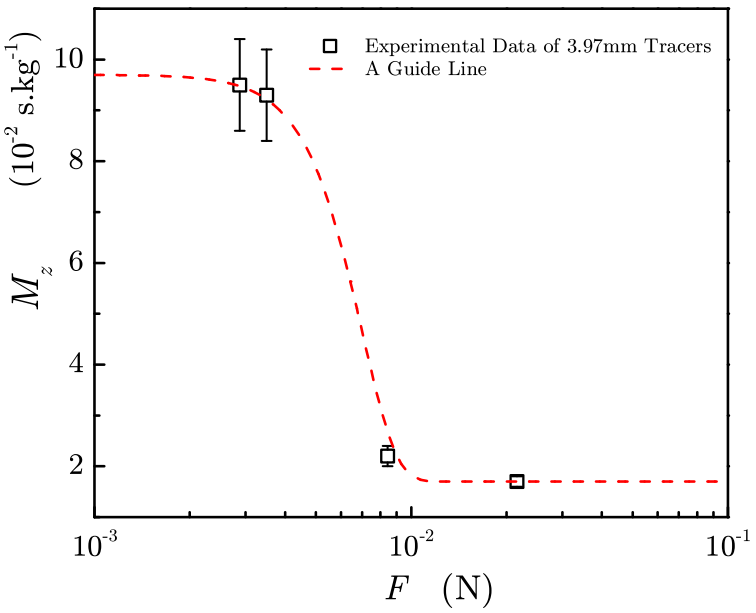

Figure 4.18: Mobility, M_z, versus the external force, F, for 3.97mm tracers in Packing 1. The black squares are experimental data which is coming from different types of tracer, they are (from left to right) nylon, delrin, ceramic and brass. The red dashed guide line is a function of $8.0\exp\left[-(x/0.007)^4\right]+1.7$.

4.3.5 Linear Response Regime

In an effort to further test the concept of the effective temperature as an intensive quantity, a linear response regime in the system is of great interest. Such a regime would imply that mobility and diffusivity are independent of the external gravitational force as $F \to 0$. The external force is varied by changing the density of the tracers of the same size. This is realized experimentally in Packing 1 by the introduction of delrin ($\rho' = 1.36$) tracers of 3.97mm diameter, the density of which is higher than that of nylon ($\rho' = 1.12$).

Analysis of the trajectories reveals that the mobility is approximately the same for both the delrin and nylon tracers with the same diameter and is thereby inde-

pendent of the external force, as shown in Fig. 4.17b and Fig. 4.18. Further, the external force should have no effect on the diffusivity. By calculating the diffusivity of the non-tracer particles via dying acrylic tracers and analyzing their trajectories, as shown in Fig. 4.17a, the diffusion of the acrylic tracers of size 3.17mm (for which no external force is applied) is the same as the diffusion of the delrin tracers of the same size (for which the gravitational force is applied). A further example of this property would be using two different tracers with different sizes, but having the same external force applied. One would calculate two different values of the diffusivity, due to the variation in tracer size, without having any variation in external force.

Nonlinear effects appear for tracers heavier than delrin, implying that mobility depends on the external force for large enough forces. We find that for a 3.97mm ceramic tracer ($\rho' = 3.28$) in Packing 1 the mobility is $M_{z\ \mathrm{ceramic}} = (2.2 \pm 0.2) \times 10^{-2}$ s/kg and for a brass tracer ($\rho' = 8.4$), $M_{z\ \mathrm{brass}} = (1.7 \pm 0.1) \times 10^{-2}$ s/kg as shown in Table 4.1, smaller than the mobility of the nylon and delrin tracers of the same size. This behavior is expected since if a linear regime exists in the system, it will be valid only within certain limits, i.e., M_z remains a constant for small value of external force, F, as shown in Fig. 4.18. It is here that our experiments approach the boundaries presented above for estimated of energy scales for the sheared granular system. Our effective temperature measurements are therefore limited to those tracer particles for which we experience a linear regime with respect to both mobility and diffusivity.

Lastly, the experiment is again repeated for a different packing of spherical particles, noted earlier as Packing 2. Having nearly the same volume fraction

of particles being both packings of spherical particles, one would expect T_{eff} to remain unchanged, as it is a measure of how dense the particulate packing is (i.e. a large T_{eff} implies a loose configuration, e.g. random loose packing, while a reduced T_{eff} implies a more compact structure, e.g. random close packing). It is found that although differences exist between the two packings with respect to mobility and diffusivity, as shown in Fig. 4.17a,b, the effective temperature remains approximately the same, as shown in Fig. 4.17c. It should be noted that both packings are composed of spherical particles and the statement regarding effective temperature as a measure of particulate packing density would not be true if the packings are composed of particles of, for instance, different shapes, even if they have the same volume fraction.

4.3.6 Shear Rate Dependence

We further explore the effective temperature as an intensive quantity by analyzing diffusivity and mobility as a function of the shear rate. We show in Fig. 4.19 that the effective temperature seems to become approximately constant, as long as the particulate motion is slow enough such that the system is very close to jamming. We find that

$$D_z \sim \dot{\gamma}_e, \dot{\gamma}_e \leq 0.06\text{s}^{-1} \tag{4.16}$$

$$M_z \sim \dot{\gamma}_e, \dot{\gamma}_e \leq 0.04\text{s}^{-1} \tag{4.17}$$

while $T_{\text{eff}} = D_z/M_z$ remains approximately constant for sufficiently small $\dot{\gamma}_e$.

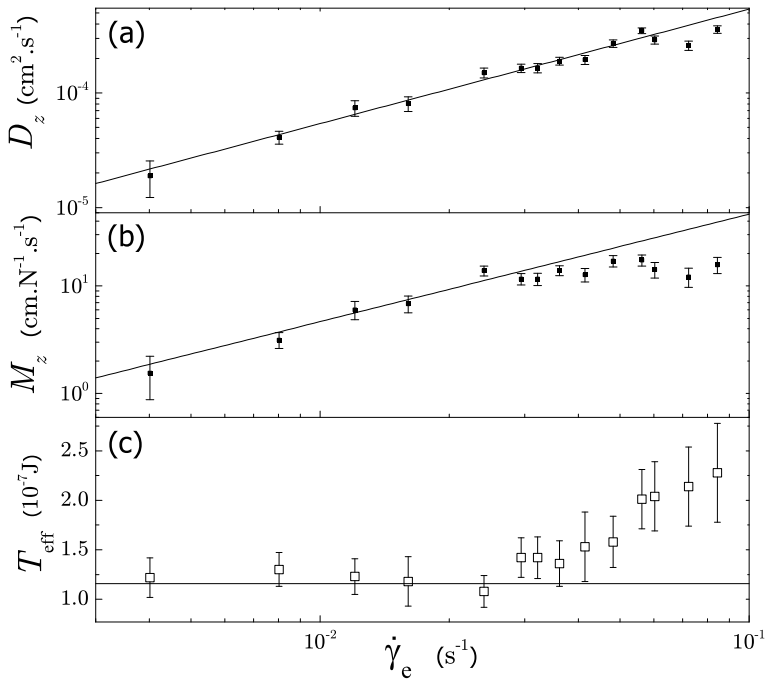

Figure 4.19: The dependence of (a) diffusivity D_z, (b) mobility M_z and (c) effective temperature T_{eff} on the shear rate $\dot{\gamma}_e$ for the 4.76mm nylon tracers in Packing 2. The solid lines in (a) and (b) are linear fitting [note that the line in (b) is a fitting only for the first 6 data points at the small value of shear rate $\dot{\gamma}_e$]. We find that $D_z \sim \dot{\gamma}_e$ and $M_z \sim \dot{\gamma}_e$, while $T_{\text{eff}} = D_z/M_z$ is approximately constant for sufficiently small $\dot{\gamma}_e$. This quasi-static regime coincides with the appearance of a rate-independent stress in experiments [87], that T_{eff} is interpreted as the temperature of the jammed states. The height of flat solid line in (c) is calculated from the slope of lines in (a) and (b), which indicates a constant effective temperature $T_{\text{eff}} = (1.2 \pm 0.2) \times 10^{-7}$J at the small value of shear rate $\dot{\gamma}_e$.

It is within this quasi-static range where the effective temperature could be identified with exploration of the jammed configurations. As it remains an important assumption of this study that the system is being continuously jammed, shear rates high enough to impact the effective temperature measurement imply systems that are not continuously exploring jammed configurations. As we study the nature of the jammed granular packings, it is logical to presume that quasi-static shearing will provide systems of interest. The limit of T_{eff} as $\dot{\gamma}_e \to 0$ may result in an effective temperature for the static jammed configuration. The quasi-static shear rate regime observed could be analogous to the shear-rate independent regime observed in the behavior of shear stress in slowly sheared granular materials [26, 87]. This solid friction-like behavior has been previously studied [26, 87] and occurs when frictional forces and enduring contacts dominate the dynamics. This regime has been also observed in recent computer simulations of the effective temperature of sheared granular materials [70, 88]. Our calculations of T_{eff} for systems close to jamming exclude the systems outside of the quasi-static range, in accordance with prior studies.

4.4 Outlook: Significance Of T_{eff} for a Statistical Mechanics of Grains

In contrast to measurements of slow mode temperatures, exemplified by T_{eff}, we also measure the temperature of the fast modes as given by the root mean square (RMS) fluctuations of the velocity of the particles. It should be noted that these velocities are not instantaneous, as the time necessary to obtain an instantaneous

velocity is much smaller than the time between measurements. Nevertheless, we can obtain an estimate of the kinetic granular temperature, T_k, from $T_k = \frac{2}{3}E_k$, where $E_k = \frac{1}{2}m\overline{v^2}$ with $\overline{v^2}$ the average kinetic energy of the grains. We obtain $T_k = 9.17\times10^{10}k_BT$, or $3.77\times10^{-10}J$ and $T_k = 1.54\times10^{11}k_BT$, or $6.34\times10^{-10}J$, for 3.17 mm and 3.97 mm delrin tracers in packing 1, respectively. Here, $T = 298.15K$, the room temperature, and $k_B = 1.3806504 \times 10^{-23}JK^{-1}$. This kinetic granular temperature is smaller than T_{eff} and differs for each type of tracer indicating that it is not governed by the same statistics. Similar results have been obtained in experiments of vibrated granular gases [89]. The significance of this result is that fast modes of relaxation are governed by a different temperature. This result is analogous to what is found in models of glasses and computer simulations of molecular glasses (see for instance Refs. [66, 4, 90, 51, 91]). In the glassy phase of these models, the bath temperature is found to control the fast modes of relaxation and a different, larger, effective temperature is found to control the slow modes of relaxation. Similarly, we find a granular bath temperature for the fast modes and a larger effective temperature for slow modes of relaxation.

It is possible to identify T_{eff} as the property of the system governing the exploration of jammed configurations. As this particular non-equilibrium system remains athermal, the 'bath' temperature in which the grains exist is immaterial, as shown above. Particle diffusion is of the order of several particle diameters over the time scale of the experiment (see Fig. 4.4 and 4.17a) implying that exploration of the available jammed configurations occurs via rearrangements of the particles outside their "cages", suggesting that the trajectory of the system can be mapped onto successive jammed configurations explored by the system.

Incorporating certain experimental conditions of reversibility, and ergodicity, a statistical mechanics formulation may well describe a jammed granular system [46, 92]. Under the primary assumption that different jammed configurations are taken to have equal statistical weight, observables can be calculated by "flat" averages over the jammed configurational space [46, 62, 19, 93, 64, 94, 95]. This assumption, advocated by Edwards and collaborators, has been thoroughly debated in the literature (see for instance [51, 33]). Existing work suggests the effective temperature obtained by applying a fluctuation-dissipation theory to non-equilibrium systems is analogous to performing a "flat" average over the jammed configurational space, at least for frictionless systems [64]. Additionally, the effective temperature can be identified with the compactivity introduced in [46], resulting from entropic calculations of the granular packing [62, 19, 64]. Experimentally testing these ideas is difficult as the entropy of the jammed configurations is not easily measured, and it is not possible to obtain the compactivity from entropic considerations in the present study.

The exploration of reversible jammed states in granular matter bears similarity to that of inherent structures in glasses. Inherent structures form a network of attractive basins within an energy landscape, and the system explores these basins as governed by their stability over the slow-relaxation time of the glass. It should be noted, however, that there exists a crucial difference between glasses and grains. In liquids energy remains conserved, while energy is dissipated in granular systems through frictional contact and path dependent forces between grains. Thus, a driven granular system will quickly come to a mechanically stable, or jammed, state after the removal of the driving forces. By its nature, energy is not conserved

in a granular system. As energy conservation is the crucial property used to define an energy ensemble in statistical mechanics, the use of energy to characterize granular systems is questionable. Thus, while T_{eff} seems to imply the exploration of reversible jammed states within an energy ensemble, with

$$P(E) \sim \mathrm{e}^{-\frac{E}{T_{\text{eff}}}} \tag{4.18}$$

describing the nature of the exploration, the validity of the energy ensemble to describe granular matter in the absence of energy conservation remains an open question. Here, we set the analogous Boltzmann constant for grains equal to unity for simplicity.

Noting the drastic difference between the bath temperature and the effective temperature in a granular system, we are inspired towards a more careful analysis of the energy ensemble in slowly driven granular systems. The work of Edwards has promoted the concept of a volume ensemble, where the free volume per grain in a static granular system replaces the energy as the conserved quantity of the non-equilibrium system, at a particular volume fraction [46, 92]. The basis for using the volume ensemble stems from the ability to conserve volume in a given packing and additivity of volume per grain. Further, it is possible to explore the configuration of states at a fixed volume, via experiment or simulation. The statistical mechanics is then derived using methods similar to Boltzmann statistics for equilibrium systems. From these methods, one can obtain the compactivity, X, as a derivative of the entropy with respect to the volume, enabling the calculation of an equation of state in the volume ensemble as follows.

$$X^{-1} = \frac{\partial S}{\partial V} \tag{4.19}$$

The compactivity, X, is thereby assumed to be an equilibrium measure of a system within the framework of the volume ensemble, much like the bath temperature of the energy ensemble. This assumption can be realized by performing an ABC experiment and testing a zero-th law of thermodynamics for volumes [33]. According to the zero-th law of thermodynamics, if system A and C are in thermal equilibrium with system B respectively, then A and C are in thermal equilibrium with equal temperature. In granular system, such an experiment would require two granular systems with distinct volumes, V_1 and V_2, with the same X. Bringing these two systems together should result in a granular system of volume $V = V_1 + V_2$, at the same X, if the assumption is valid. This experiment is feasible due to the fact that it is always possible to prepare a system at a given volume fraction and will be the subject of future study and experiment, facilitated by recent theoretical findings [96].

Similar to the conservation of volume, boundary stress may also be a conserved quantity in jammed granular systems, and Edwards statistical mechanics for volume distributions could be applied analogously to the distribution of boundary stresses, Π, or forces, referred to as the force ensemble [97, 98]. The angoricity, A, is calculated as the derivative of the entropy with respect to the boundary stress, and an additional equation of state is thereby achieved as follows:

$$A^{-1} = \frac{\partial S}{\partial \Pi} \tag{4.20}$$

This result can be combined with that of the volume ensemble in an effort to accurately define the statistical mechanics of static jammed granular matter. Such an approach remains a topic of ongoing research.

However, slowly driven granular systems introduce yet another ensemble, the energy ensemble, from which the above defined T_{eff} is derived. While the above results reveal that T_{eff} does not tend to zero as the magnitude of the driving force decreases, indicating extrapolation to a non-zero static quantity, it remains unclear how the effective temperature may relate to the compactivity and angoricity as defined by Edwards statistics. Are we defining a new static quantity by determining the static limit of T_{eff}, or are we expanding the statistical mechanics of jammed granular matter to include dynamic systems by relating T_{eff}, X and A? T_{eff} is obtained in the quasi-static limit $\dot{\gamma}_e \to 0^+$, while the volume and force ensembles correspond to $\dot{\gamma}_e = 0$, exactly. Is it possible that a relation between T_{eff}, X and A can be expected?

There exists the further requirement of energy conservation for the validity of a Boltzmann approach that would guarantee:

$$T_{\text{eff}}^{-1} = \frac{\partial S}{\partial E} \tag{4.21}$$

As discussed above, energy is constantly dissipated in a driven granular system, through Coulomb friction and path-dependent tangential forces between grains. However, the input of energy by the external driving force brings the system to a steady state where the average energy is constant over the time-scale of the experiment. This steady state energy could be likened to the conserved variable in a statistical formalism depicted in Eq. 4.21, thereby introducing a thermodynamic

meaning for T_{eff}.

In a compressed emulsion system the absence of Coulomb friction and inter-particle tangential forces greatly simplifies the formalism [53]. Jamming occurs due to osmotic pressure, and the system remains athermal as a result of the large particle size. A well defined potential energy exists due to the absence of tangential forces, corresponding to the deformation of the particles at the inter-particle contact points. Therefore, a restriction to use the energy ensemble in an effort to describe a jammed system is lifted, as frictional tangential forces no longer hinder energy conservation.

Computer simulations of frictionless emulsion droplets [33] incorporate a simulated annealing method employing an auxiliary temperature to sample the available jammed configurations. The simulated annealing method assumes a Boltzmann distribution, or a flat average assumption, over the jammed states of the emulsion. The T_{eff} obtained by Eq. 4.21 with simulated annealing methods [64] is very close in value to the T_{eff} obtained via the FDT calculations as in the present work. Such a result could indicate that ergodicity holds in this frictionless system, a further justification of the methods presented herein. Therefore, a firmer basis for the validity of using the T_{eff} obtained in the quasi-static limit to describe the statistical mechanics of the same system at the static limit is achieved.

Further, T_{eff} remains approximately constant with varying tracer particle size, implying a zero-th law of thermodynamics for slowly sheared jammed granular systems. These statements further provoke the necessity for an ABC experiment, to test the zero-th law for the effective temperature, as well as similar experiments for the compacitivity and angoricity. Such experiments may enlighten us to under-

stand under what conditions $P(E) \sim \mathrm{e}^{-\frac{E}{T_{\mathrm{eff}}}}$, $P(V) \sim \mathrm{e}^{-\frac{V}{X}}$ and $P(\Pi) \sim \mathrm{e}^{-\frac{\Pi}{A}}$ may be valid in describing the statistics of the jammed and nearly jammed granular systems.

At this point, we believe that the most prominent direction is the exploration of the volume and pressure ensembles. Our understanding is that these ensembles may be sufficient to characterize the jammed state of granular matter, while the energy ensemble may be necessary for slowly moving granular systems. These are open questions at the present time. Recent papers in the theory and simulation front suggest that the compactivity characterizes the system into a phase diagram at the isostatic point, while the angoricity will be necessary to describe the pressure ensemble of compressible granular matter [96].

4.5 Summary

In summary, this study focuses on the dynamics of slowly sheared granular matter in a 3D Couette cell. A mixture of spherical, transparent and bi-disperse grains are confined between two cylinders, having walls roughened by glued identical grains, with the inner cylinder rotated via motor. We compact the grains by means of an external pressure in the negative z-direction. Fluid matching the density and refractive index of the grains partially fills the cell, allowing tracking of tracer particle trajectories as a function of time. Tracers of varying density and size are used. Multiple cameras track the tracer particle positions relative to the cylinders.

We find that the angular velocity of the tracer particles, $\omega_\theta(r)$, follows an exponential relation with r, defined by the type of packing and geometry of the

Couette cell. The velocity of the last layer of grains is non-zero, such that the shear band is located at the outer cylinder and ensures no formation of shear bands in the bulk. Near the outer cylinder $\omega_\theta(r)$ decays slowly with increasing r, such that $\omega_\theta(r)$ can be approximated linearly with a constant local shear rate. The constant local shear rate ensures that the mobility and diffusivity of tracers, dependent on local shear rate, remain approximately independent of r. We define this region the "constant mobility and diffusivity region", or the CMD region.

An "effective temperature", T_{eff}, is realized by a fluctuation-dissipation relation generalized to granular materials. Statistical measurements are confined exclusively to the CMD region. The mobility in the vertical direction, M_z, is found to be proportional to the shear rate, $\dot{\gamma}_e$, for small enough values of $\dot{\gamma}_e$. As D_z is also found proportional to shear rate, collapsing all the $D_z(r)$ for various shear rates shows a plateau in the CMD region. An approximately constant effective temperature is obtained from measurements of the mobility and diffusivity, under a constant external applied force, and with sufficiently small shear rates. This effective temperature is calculated by an analogous equation used in equilibrium statistical mechanics. We find this effective temperature to be independent of the tracer particle properties, and dependent only on the packing density of the system. While this result describes an intensive property of the system, it remains an important future study to test the effective temperature against the laws of thermodynamics. More specifically, a test of the zeroth-law of thermodynamics with respect to these non-equilibrium jammed systems could expand the scope of T_{eff} beyond that of an intensive quantity of a particular system. A well defined effective temperature in the radial direction may exist, though its existence would

require a constant external force applied in the radial direction.

The probability distribution of the displacements in the radial direction, $P(\Delta r)$, reveals exponential fluctuations. The analysis of the fluctuations reveals a power law, sub-diffusive, process, $\langle \Delta r^2 \rangle \sim \Delta t^{\alpha}$, with α less than unity. A similar analysis for fluctuations in the angular direction reveal a super-diffusive process, $\langle \Delta \theta^2 \rangle \sim \Delta t^{\beta}$, with β greater than unity. Lastly, the probability distribution of the displacements in the vertical direction are found have a Gaussian distribution such that $\langle \Delta z^2 \rangle \sim \Delta t$. It is this linearity that defines vertical displacement as a diffusive process, and allows for the use of the Fluctuation-Dissipation relation to calculate the diffusivity in the vertical direction. We further discover a linear relationship between angular displacement and the time between measurements $\Delta \theta_e \sim \Delta t$, such that all mean square fluctuations can be defined in terms of $\Delta \theta_e$ for the small shear rates of our experiments.

In the CMD region, the linear approximation of $\omega_\theta(r)$ proportional to approximately constant external shear rate, $\dot{\gamma}_e$, allows for the collapsing of all tracer particle velocity curves via dividing $\omega_\theta(r)$ by the shear rate. This collapse reveals a periodic shape with a small amplitude and periodic length roughly equal to the grain size. The effect is shown to be weaker in packings with smaller size grains. We further apply this remarkable scaling feature $v_z(r)$ and $v_r(r)$, achieving similar results.

It is important to note that the effective temperature, defined in this study for small shear rates, does not remain constant as the shear rate increases. While previous studies have discovered an an increasing effective temperature via simulations, we have measured diffusivity and mobility separately in an effort to calculate T_{eff}

through a fluctuation-dissipation relation. We find the diffusivity in the z-direction remains approximately constant throughout the range of shear rates used in this experiment, while the mobility in the z-direction approaches a plateau. exclusively increasing T_{eff}. Such an effect in the radial direction would be of great interest for future studies in sheared granular dynamics.

The nearly constant value of T_{eff} with respect to varying tracer particle size indicates that a zero-th law of thermodynamics for slowly sheared jammed granular systems could be valid and prompts one to perform an ABC experiment, fully testing the zero-th law for the effective temperature.

As we work towards a more complete description of the statistical mechanics of jammed granular matter, we strive to incorporate the varied statistical ensembles into one fundamental picture. These ensembles include the energy ensemble, as described herein, along with the volume and force ensembles, as proposed by Edwards. Such an incorporation may link static quantities of compacitivity and angoricity, describing volume and force ensembles, respectively, to the dynamic effective temperature presented in this study, derived from the energy ensemble. The exact nature of the relation between such quantities remains an open topic. Ultimately, these quantities will help to develop a thorough statistical description for jammed granular matter and reveal an equation of state. A deeper topic of concern is the formation of a clear definition of energy in jammed granular matter. Energy is not conserved in frictional systems and it remains open to debate as to how one would incorporate energy into the statistical mechanics.

One possible approach to describe the energy of jammed systems is to consider the similarities between the inherent structure formalism of glasses and the ex-

ploration of jammed states in granular matter, at least for the case of frictionless granular systems. Inherent structures probe a network of potential energy basins within an energy landscape. Such an approach toward the jammed states of granular matter may assist in understanding exactly what is meant by energy within the framework of a non-equilibrium system.

Bibliography

[1] E. R. Nowak, J. B. Knight, M. L. Povinelli, H. M. Jaeger and S. R. Nagel. *Powder Technol.* **94**, 79 (1997).

[2] S. F. Edwards, The role of entropy in the specification of a powder, in *Granular matter: an interdisciplinary approach* (ed A. Mehta) 121-140 (Springer-Verlag, New York, 1994).

[3] S. F. Edwards and R. B. S. Oakeshott, Theory of powders, *Physica A* **157**, 1080-1090 (1989).

[4] A. Liu and S. R. Nagel, (eds.), *Jamming and Rheology: Constrained Dynamics on Microscopic and Macroscopic Scales*, Taylor & Francis, London, 2001.

[5] P. G. Debenedetti and F. H. Stillinger, *Nature* **410**, 259 (2001).

[6] F. H. Stillinger and T. A. Weber, *Phys. Rev. A* **25**, 978 (1982); *ibid*, *Science* **225**, 983 (1984).

[7] M. Goldstein, *J. Chem. Phys.* **51** 3728 (1969).

[8] S. Sastry, P. G. Debenedetti, and F. H. Stillinger, *Nature* **393**, 554 (1998).

[9] W. Kob, F. Sciortino, and P. Tartaglia, *Europhys. Lett.* **49**, 590 (2000).

[10] B. Coluzzi, G. Parisi, and P. Verrocchio, *Phys. Rev. Lett.* **84**, 306 (2000).

[11] A. Fierro, M. Nicodemi, and A. Coniglio, *Europhys. Lett.* **59**, 642 (2002).

[12] L. C. E. Struik, *Physical Aging in Amorphous Polymers and other Materials*, (Elsevier, Houston, 1978)

[13] M. Mézard, G. Parisi and M. A. Virasoro, *Spin Glass Theory and Beyond* (World Scientific, Singapore, 1987).

[14] T. R. Kirkpatrick and D. Thirumalai, *Phys. Rev. B* **36**, 5388 (1987); T. R. Kirkpatrick and P. Wolynes, *Phys. Rev. A* **35**, 3072 (1987).

[15] L. F. Cugliandolo, J. Kurchan, and L. Peliti, *Phys. Rev. E* **55**, 3898 (1997).

[16] J. Kurchan, Rheology and how to stop aging, in A. Liu and S. R. Nagel, (eds.), *Jamming and Rheology: Constrained Dynamics on Microscopic and Macroscopic Scales*, Taylor & Francis, London, 2001, cond-mat/9812347.

[17] J. Kurchan, Emergence of macroscopic temperatures in systems that are not thermodynamical microscopically: towards a thermodynamical description of slow granular rheology. *J. Phys. Condensed Matter* **29**, 6611 (2000).

[18] M. Nicodemi, Dynamical response functions in models of vibrated granular media. *Phys. Rev. Lett.* **82**, 3734-3737 (1999).

[19] A. Barrat, J. Kurchan, V. Loreto, M. and Sellitto Edwards measures for powders and glasses. *Phys. Rev. Lett.* **85**, 5034-5037 (2000); Edwards' measures: a

thermodynamic construction for dense granular media and glasses. *Phys. Rev. E* **63**, 51301 (2001), and references therein.

[20] H. A. Makse and J. Kurchan. Testing the Thermodynamics Approach to Granular Matter with a Numerical Model of a Decisive Experiment. *Nature* **415**, 614-617 (2002).

[21] S. F. Edwards, The aging of glass forming liquids, in *Disorder in Condensed Matter Physics* (eds J. Blackman, & J. Taguena) 147-154 (Oxford University Press, Oxford, 1991).

[22] A. Mehta, and S. F. Edwards, Statistical mechanics of powder mixtures. *Physica* **A 157**, 1091-1097 (1989).

[23] J. Brujić, S. F. Edwards, and D. Grinev, Jammed systems in slow flow need a new statistical mechanis, *Phil. Trans. R. Soc. Lond.* A, **361**, 741-751 (2003).

[24] J.-P. Bouchaud, M. E. Cates, and P. Claudin, *J. Phys. I* (France) **5**, 639 (1995); M. E. Cates, P. Wittmer, J.-P. Bouchaud, and P. Claudin, *Phys. Rev. Lett.* **81**, 1841 (1998).x

[25] J. B. Knight, E. E. Ehrichs, V. Yu. Kuperman, J. K. Flint, H. M. Jaeger, and S. R. Nagel, *Phys. Rev. E***54**, 5726 (1996).

[26] S. B. Savage, The mechanics of rapid granular flows. *Adv. Appl. Mech.* **24**, 289-365 (1994).

[27] J. T. Jenkins, and S. B. Savage, A theory for the rapid flow of identical, smooth, nearly elastic, spherical particles. *J. Fluid Mech.* **130**, 187-202 (1983).

[28] H. J. Herrmann, J. P. Hovi, and S. Luding, eds., *Physics of Dry Granular Matter* (Kluwer, Dordrecht, 1998).

[29] R. P. Behringer and J. T. Jenkins, eds., *Powders & Grains 97* (Balkexma, Rotterdam, 1997).

[30] J. Brujić, D. L. Johnson, O. Sindt, and H. A. Makse (SDR report, to be published).

[31] E. R. Nowak, J. B. Knight, E. BenNaim, H. M. Jaeger and S. R. Nagel. *Phys. Rev. E* **57**, 1971 (1998).

[32] P. Philippe, and D. Bideau, *Europhys. Lett.* **60**, 677 (2002).

[33] A. Chakravarty, S. F. Edwards, D. V. Grinev, M. Mann, T. E. Phillipson, A. J. Walton, Proceedings of the Workshop on Quasi-static Deformations of Particulate Materials, to be published.

[34] A. J. Liu and S. R. Nagel, "Jamming is not Just Cool Any More", *Nature* **396**, 21 (1998).

[35] V. Trappe, V. Prasad, L. Cipelletti, P. N. Segre, and D. A. Weitz. Jamming phase diagram for attractive particles. *Nature 411*, 772 (2001).

[36] G. D'Anna and G. Gremaud. The jamming route to the glass state in weakly perturbed granular media. *Nature* **413**, 407 (2001).

[37] L. D. Landau and E. M. Lifshitz, *Statistical Physics* (Pergamon, NY, 1970).

[38] R. C. Ball and R. Blumenfeld, Phys. Rev. Lett. **88**, 115505 (2002).

[39] R. Blumenfeld and S. F. Edwards, Phys. Rev. Lett. **90**, 114303 (2002).

[40] J. D. Bernal, and J. Mason, "Coordination of Randomly Packed Spheres", *Nature* **188**, 910 (1960); J. D. Bernal, "The Structure of Liquids", *Proc. Roy. Soc. London,* Ser. A **280**, 299 (1964).

[41] G. D. Scott, "Packing of Equal Spheres", *Nature* **188**, 908 (1960).

[42] Hales, T. C. The Kepler conjecture. http://arxiv.org/abs/math.MG/9811078

[43] Behringer, R. P. & Jenkins, J. T. eds., *Powders & Grains 97* (Balkema, Rotterdam, 1997).

[44] Onoda, G. Y. & Liniger, E. G. Random loose packings of uniform spheres and the dilatancy effect. *Phys. Rev. Lett.* **64**, 2727-2730 (1990).

[45] J. G. Berryman, "Random Close Packing of Hard Spheres and Disks", *Phys. Rev. A* **27**, 1053 (1983).

[46] Edwards, S. F. & Oakeshott, R. B. S. Theory of powders. *Physica A* **157**, 1080-1090 (1989).

[47] Schröter, M., Goldman, D. I. & Swinney, H. L. Stationary state volume fluctuations in a granular medium. *Phys. Rev. E* **71**, 030301(R) (2005).

[48] Aste, T., Saadatfar, M. & Senden, T. J. Local and global relations between the number of contacts and density in monodisperse sphere packs. *J. Stat. Mech.*, P07010 (2006).

[49] da Cruz, F., Lechenault, F., Dauchot, O. & Bertin, E. Free volume distributions inside a bidimensional granular medium, in Powders and Grains 2005,

García-Rojo, R., Herrmann, H. J. & McNamara, S. Eds. (A. A. Balkema, Rotterdam, 2005).

[50] Bertin, E., Dauchot, O. & Droz, M. Definition and relevance of nonequilibrium intensive thermodynamic parameters. *Phys. Rev. Lett.* **96**, 120601 (2006).

[51] Fierro, A., Nicodemi, M., Tarzia, M., de Candia, A. & Coniglio, A. Jamming transition in granular media: A mean-field approximation and numerical simulations. *Phys. Rev. E* **71**, 061305 (2005).

[52] Ciamarra, M. P., Coniglio, A. & Nicodemi, M. Thermodynamics and statistical mechanics of dense granular media. *Phys. Rev. Lett.* **97**, 158001 (2006).

[53] Brujić J., Edwards, S. F., Hopkinson, I. & Makse, H. A. Measuring distribution of interdroplet forces in a compressed emulsion system. *Physica* A **327**, 201-212 (2003).

[54] Makse, H. A., Johnson, D. L. & Schwartz, L. M. Packing of compressible granular materials. *Phys. Rev. Lett.* **84**, 4160-4163 (2000).

[55] C. S. O'Hern, S. A. Langer, A. J. Liu, and S. R. Nagel, "Force Distributions near Jamming and Glass Transitions", *Phys Rev. Lett.* **86**, 111 (2001).

[56] Torquato, S. Truskett, T. M. & Debenedetti, P. G. Is random close packing of spheres well defined? *Phys. Rev. Lett.* **84**, 2064-2067 (2000).

[57] S. Alexander, Phys. Rep. **296**, 65 (1998).

[58] Edwards, S. F. & Grinev, D. V. Statistical mechanics of stress transmission in disordered granular arrays. *Phys. Rev. Lett.* **82**, 5397-5400 (1999).

[59] L. E. Silbert, D. Ertas, G. S. Grest, T. C. Halsey, and D. Levine, Phys. Rev. E **65**, 031304 (2002).

[60] Torquato, S. & Stillinger, F. H. Multiplicity of generation, selection, and classification procedures for jammed hard-particle packings. *J. Phys. Chem B* **105**, 11849-11853 (2001).

[61] Zhang, H. P. & Makse, H. A. Jamming transition in emulsions and granular materials. *Phys. Rev. E* **72**, 011301 (2005).

[62] Krzakala, F. & Kurchan, J. Landscape analysis of constraint satisfaction problems. *Phys. Rev. E* **76**, 021122 (2007).

[63] S. F. Edwards and D. V. Grinev, "Statistical Mechanics of Stress Transmission in Disordered Granular Arrays", *Phys. Rev. Lett.* **82**, 5397 (1999).

[64] Makse, H. A. & Kurchan, J. Testing the thermodynamic approach to granular matter with a numerical model of a decisive experiment. *Nature* **415**, 614-617 (2002).

[65] L. D. Landau and E. M. Lifshitz, *Statistical Physics*, (Pergamon, New York, 1970).

[66] L. F. Cugliandolo, J. Kurchan and L. Peliti, *Phys. Rev. E* **55**, 3898 (1997).

[67] S. A. Langer and A. J. Liu, *Europhysics Lett.* **49**, 68 (2000).

[68] F. Sciortino and P. Tartaglia, *Phys. Rev. Lett.* **86**, 107 (2001).

[69] J. L. Barrat and L. Berthier, *Phys. Rev. E* **63**, 012503 (2001).

[70] I. K. Ono, C. S. O'Hern, D. J. Durian, S. A. Langer, A. J. Liu and S. R. Nagel, *Phys. Rev. Lett.* **89**, 095703 (2002).

[71] H. M. Jaeger, S. R. Nagel and R. P. Behringer, *Rev. Mod. Phys.* **68**, 1259 (1996).

[72] D. W. Howell, R. P. Behringer and C. T. Veje, *Phys. Rev. Lett* **82,** 5241 (1999).

[73] C. T. Veje, D. W. Howell and R. P. Behringer, *Phys. Rev. E* **59,** 739 (1999).

[74] D. M. Mueth, G. F. Debregeas, G. S. Karczmar, P. J. Eng, S. R. Nagel, and H. M. Jaeger, *Nature* **406**, 385 (2000).

[75] D. M. Mueth *Phys. Rev. E* **67**, 011304 (2003).

[76] B. Utter and R. P. Behringer, *Phys. Rev. E* **69**, 031308 (2004).

[77] R. Nedderman, *Statics and Kinematics of Granular Materials* (Cambridge Univ. Press, Cambridge, 1992).

[78] T. G. Drake, *J. Geophys. Res.* **95**, 8681 (1990).

[79] C. Song, P. Wang, and H. A. Makse, *Proc. Nat. Acad. Sci.* **102**, 2299 (2005).

[80] E. R. Nowak, J. B. Knight, E. Ben-Naim, H. M. Jaeger, and S. R. Nagel, "Density Fluctuations in Vibrated Granular Materials", *Phys. Rev. E* **57**, 1971 (1998).

[81] P. Wang, C. Song and H. A. Makse, *Nature Physics* **2**, 526 (2006).

[82] E. R. Weeks, J. C. Crocker, A. C. Levitt, A. Schofield and D. A. Weitz, *Science* **287**, 627 (2000).

[83] J. A. Drahun and J. Bridgwater, *Powder Technol.* **36**, 39 (1983).

[84] G. Taylor, *Proc. Roy. Soc. A* **219**, 186 (1953).

[85] G. D'Anna, P. Mayor, A. Barrat, V. Loreto and F. Nori, *Nature* **424**, 909 (2003).

[86] D. C. Rapaport, *The Art of Molecular Dynamics Simulation* (Cambridge University Press, Cambridge, 1995).

[87] G. I. Tardos, S. McNamara and I. Talu, *Powder Tech* **131** 23 (2003).

[88] N. Xu and C. S. O'Hern, *Phys. Rev. Lett.* **94**, 055701 (2005).

[89] K. Feitosa and N. Menon, *Phys. Rev. Lett.* **88**, 198301 (2002).

[90] A. Mehta and T. C. Halsey, (eds) *Challenges in Granular Physics* (World Scientific, Singapore, 2002).

[91] H. Hinrichsen and D. E. Wolf, (eds) *The Physics of Granular Media* (Wiley-VCH Verlag, 2004).

[92] S. F. Edwards and R. B. S. Oakeshott, *Physica A* **157**, 1080 (1989).

[93] A. Fierro, M. Nicodemi and A. Coniglio, *Europhys. Lett.* **59**, 642 (2002); A. Fierro, M. Nicodemi, and A. Coniglio, *Phys. Rev. E* **66**, 061301 (2002).

[94] A. Mehta and J. M. Luck, *J. Phys. A.: Math. Gen.* **36**, L365 (2003).

[95] J. Berg and A. Mehta, *Phys. Rev. E* **65**, 031305 (2002).

[96] C. Song, P. Wang and H. A. Makse, *A Phase Diagram for Jammed Matter*, accepted by *Nature*.

[97] S. F. Edwards, *Physics A* **353**, 114 (2005).

[98] S. Henkes, C. S. O'Hern, and B. Chakraborty, *Phys. Rev. Lett.* **99**, 038002 (2007).